7

Modeling, optimization and control of resin flow during manufacturing of textile composites with liquid molding

A GOKCE and S G ADVANI,
University of Delaware, USA

7.1 Liquid composite molding processes

Liquid composite molding (LCM) processes are commonly used to manufacture polymer–textile composites because of their low equipment and tooling costs, low pressure requirements, short cycle times and ability to yield net-shape parts [1]. Some variations of LCM processes are resin transfer molding (RTM), vacuum-assisted resin transfer molding (VARTM), resin infusion process (RIP) and Seemann composites resin infusion molding process (SCRIMP).

LCM processes include three basic steps (Fig. 7.1) [2]:

1. The textiles, which constitute the reinforcing component of the composite part, are cut from large rolls to the dimensions of the composite part to be manufactured. The textile sheets are placed into the mold. The mold

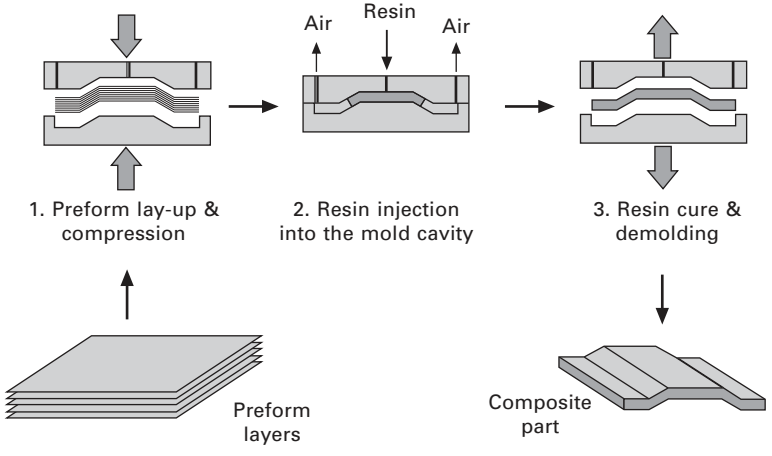

7.1 Three basic steps of resin transfer molding, a liquid composite molding process.

is closed and sealed. If the mold is single-sided as in SCRIMP and VARTM, it is covered with a plastic bag instead of a rigid tool. In RTM, which involves matching dies, the mold is closed and the mold cavity is sealed by fastening the mold with nuts and bolts, or by applying pressure with a press.

2. The resin is injected into the mold cavity through the gates. In vacuum-assisted processes such as SCRIMP and VARTM, the air is removed from the mold cavity prior to the resin injection. Atmospheric pressure drives the resin through the preform and the maximum pressure at the injection gates is one atmosphere. In RTM, high pressures can be applied at the gates. Resin advances through the fibrous preform owing to the injection pressure, pushing air out of the mold through the vents.
3. After the injection step is complete, the resin in the mold cavity cures through a series of chemical reactions to form a solid part.

The textile sheets that form the reinforcements placed in the mold before resin injection are made of fibers. The textile properties are determined by the fiber material and the textile architecture. In most of the textiles, glass fibers are used [3, 4]. Carbon and aramid (Kevlar) are among the other fiber types used. The fiberscan be either used in single strands as in *chopped* and *continuous strand random mat*, or can be used to form tows containing 200 to 4000 fibers, which are then used to make textile sheets (also known as preforms). Three types of textiles are illustrated in Fig. 7.2 a random mat, a preform that is woven using carbon fiber tows and a preform with loosely stitched glass fiber tows. Several types of preforms can be produced by stitching, weaving and braiding fiber tows.

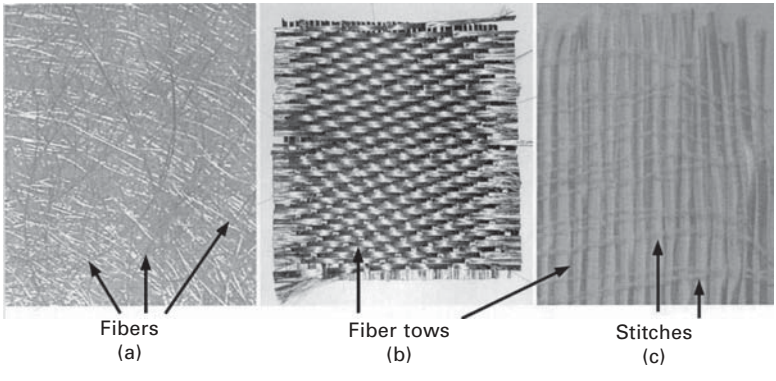

7.2 (a) A random mat. (b) A preform that is woven using carbon fiber tows. (c) A preform that is manufactured by loosely stitching fiber tows.

Manufacturing an acceptable composite part depends on successful completion of the three steps shown in Fig. 7.1. The mold filling step is

studied exclusively in this chapter [5–8]. Flow through porous media is modeled in the following section. In section 7.3, liquid injection molding simulation (LIMS), software that is used to simulate resin flow in the mold cavity, is introduced and its utilization in design, optimization and control studies is summarized. A method to optimize injection gate location is presented in section 7.4. Section 7.5 introduces the disturbances associated with the mold filling process and explains the major disturbance, racetracking, in detail. Section 7.6 explains the use of feedback control to offset the adverse effects of racetracking on the mold filling process. In Section 7.7, a passive control method to minimize the defect content in the composite parts is presented. The chapter is summarized and potential future research directions are discussed in section 7.8.

7.2 Flow through porous media

In LCM processes, the resin flows through a complex network of channels and paths that are formed by the architecture of the textile sheets in the mold cavity. The diameters of these channels are several orders of magnitude smaller than the gap-width of the mold. Thus, in addition to the stresses due to the presence of textile fibers, the capillary and surface tension effects may become significant. The resin flow through the fiber textiles can be characterized as a complex, dual-scale flow as illustrated in Fig. 7.3. The advance of resin through the air channels between tows is a macro-scale flow. The penetration of resin through the fibers in the tows is a micro-scale flow.

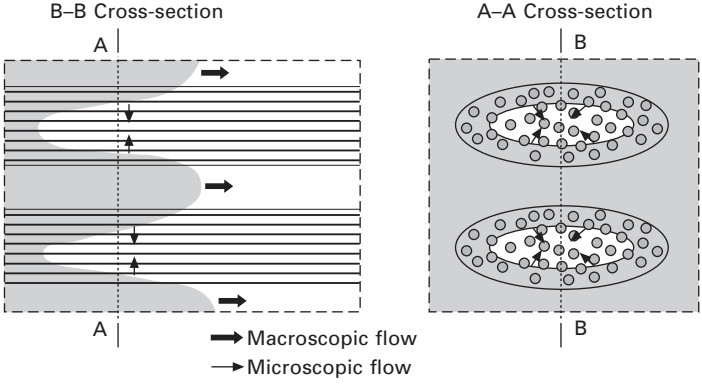

7.3 Dual-scale flow through the porous medium.

While it is theoretically possible to analyze this complex process in detail, the magnitude of immense computational power required to solve the problem forbids any attempt. Moreover, such a detailed study is not necessary as one is only interested in the macroscopic flow rate–pressure relationship during

the impregnation of resin. Thus, one would have to average the microscopic stresses to find the macroscopic relationship. The textile preforms are made up of repeated patterns. Instead of analyzing the entire mold geometry, the repetitive pattern can be identified as a unit cell and the flow can be studied in detail. The results of this microscopic study can be used determine the resistance to flow through the unit cell in an average sense. Permeability of a textile preform is defined as the ease of resin flow through the preform. Note that the permeability is an inverse measure of the flow resistance. Extensive research has been conducted to predict and measure the permeability of textiles with various architecture. These studies can be grouped in three major categories as analytical [9–15], numerical [16–22] and experimental [22–28].

The permeability is used along with Darcy's law to model the complicated flow through the porous media in an average sense:

$$\langle \boldsymbol{u} \rangle = -\frac{\boldsymbol{K}}{\eta} \cdot \nabla \langle P \rangle_{\mathrm{f}} \tag{7.1}$$

where $\langle \boldsymbol{u} \rangle$ is the resin velocity vector averaged over the volume, $\boldsymbol{K}$ is the positive definite permeability tensor of the textile preform, η is the viscosity and $\nabla \langle P \rangle_{\mathrm{f}}$ is the pressure gradient averaged over the fluid volume. In eqn 7.1, resin is modeled with η and the preform is modeled with $\boldsymbol{K}$. Note that resin flow through the porous medium is assumed be an isothermal, Newtonian flow, thus resin viscosity is taken to be constant. The resin is assumed to be incompressible, hence the continuity equation can be written as

$$\nabla \cdot \langle \boldsymbol{u} \rangle = 0 \tag{7.2}$$

Inserting eqn 7.1 into eqn 7.2, the mold-filling process can be written as an elliptic partial differential equation as:

$$\nabla \cdot (\boldsymbol{K} \cdot \nabla \langle P \rangle_{\mathrm{f}}) = \nabla \boldsymbol{K} \cdot \nabla \langle P \rangle_{\mathrm{f}} + \boldsymbol{K} \colon \nabla (\nabla \langle P \rangle_{\mathrm{f}}) = 0 \tag{7.3}$$

which governs the pressure field in the mold region that is covered with resin. Equation 7.3 is subject to the following boundary conditions (BC):

$$\text{Neumann BC at the mold walls: } \boldsymbol{n} \cdot (\boldsymbol{k} \cdot \nabla_{\mathrm{f}}) = 0 \tag{7.4}$$

$$\text{Dirichlet BC at the flow front: } P = 0$$

$$\text{and at the injection gates: } P = P_{\mathrm{i}},$$

$$\text{or: } Q = Q_{\mathrm{i}},$$

where $\boldsymbol{n}$ is the normal to the mold wall and Q is the flow rate. The flow rate boundary condition at a gate can be converted to pressure boundary condition through Darcy's law. Note that the boundary condition at a gate is applied along the boundary of a hypothetical area around the gate in two-dimensional (2D) flow, and over the surface of a hypothetical volume around the gate in three-dimensional (3D) flow.

Figure 7.4 shows domains and boundaries of interest in the mold-filling process. The entire mold cavity forms the mold domain. The region filled with the resin is the resin domain and eqn 7.3 applies in this domain only. As the resin is injected into the mold domain from the gates, the resin domain grows. Since the resin domain changes with time, the pressure distribution in the domain changes as well. Also, varying the boundary conditions at the injection gates modifies the pressure distribution in the resin domain. Therefore, although not explicit in eqn 7.3, the pressure field in the resin domain is a function of time. The resin flow through the porous medium is low Reynolds number flow, which explains the non-existence of inertia terms in eqn 7.3. Moreover, the flow can be considered to be in quasi-steady state at any given time step. Dirichlet boundary conditions apply at the free (moving) section of the outer boundary of the resin domain, which is called the flow front. Neumann boundary conditions apply at the common boundary of the mold domain and the resin domain.

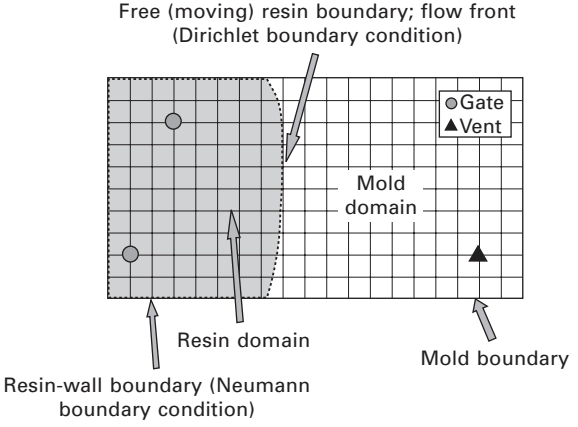

7.4 Resin and mold domains and boundaries.

The pressure gradient in eqn 7.1 is created by the pressure applied at the gates, P_i. The injection rate Q_i determines the wetted region expansion rate. The relationship between P_i and Q_i is a function of the permeability (or resistance) field in the wetted region. One either specifies the pressure P_i or the flow rate Q_i at a gate. As the problem is quasi-steady state, these values may change from one time step to the next time step.

The main function of a vent is to provide an escape passage to the air in the mold cavity. Mathematically, it enforces the Dirichlet boundary condition at the flow front. If a contiguous dry region in the mold cavity lacks a vent, the Dirichlet boundary condition in eqn 7.4 does not apply anymore along the boundary between the dry region and the resin-covered region. The pressure in the dry region increases owing to compression of air and prevents the

resin from saturating the dry region. It is highly likely that air in such a region will not be able to escape the mold cavity and will cause a dry spot in the final composite product, which has to be rejected.

The process modeled by eqns 7.3 and 7.4 is a distributed parameter system, whose solution depends on the mold geometry, permeability field in the mold cavity and injection locations and conditions. Since analytical solution is difficult for 2D and 3D flows, researchers employed numerical methods to solve it. Various numerical methods have been employed to simulate the mold filling step [29–35]. LIMS [36], software developed at the University of Delaware to simulate resin impregnation through the porous media, is introduced in the following section. Note that LIMS can also simulate resin curing during the filling phase, which is not discussed here.

7.3 Liquid injection molding simulation

LIMS uses a finite element/control volume approach to simulate the resin flow in the mold cavity. The finite element mesh of the mold geometry, the resin and textile preform properties (η and $\boldsymbol{K}$ values), gate locations and injection conditions are input to LIMS as shown in Fig. 7.5. The area around a node is assigned to the node as its control volume. In Fig. 7.6(a), the nodes at the flow front are marked with solid circles and the control volumes

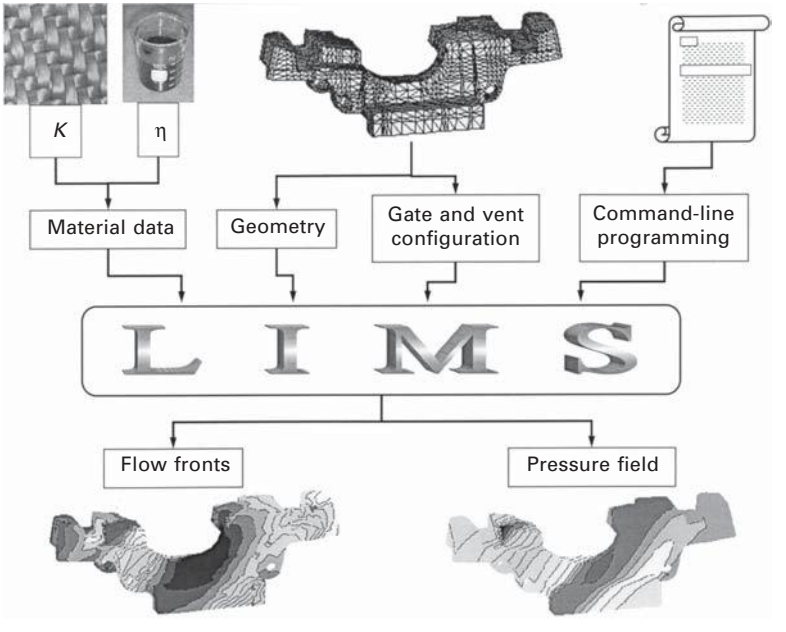

7.5 Inputs and outputs of LIMS.

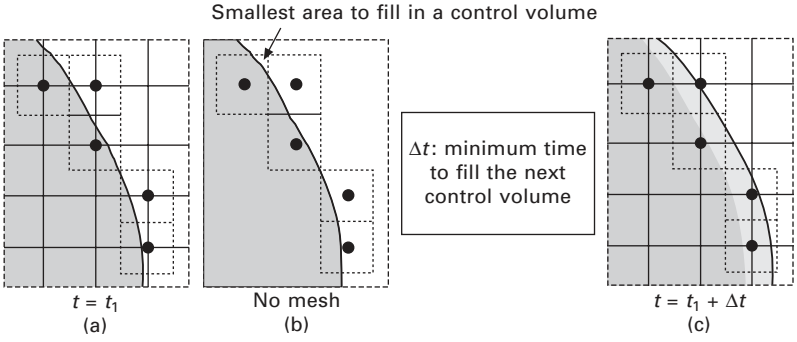

7.6 (a) Flow front location at $t = t_1$. Flow front nodes are marked with circles and the associated control volumes are circumscribed with dashed squares. (b) Mesh is removed to facilitate visualization. (c) Flow front location at $t = t_1 + \Delta t$. Note that the top left node became part of the resin domain.

around the nodes are circumscribed with dashed squares. The mold filling is simulated recursively as follows:

- *Step I*. $t = t_{new}$. LIMS solves eqns 7.3 and 7.4 using finite element methods to obtain pressure distribution $P(\boldsymbol{x})$ in the mold at $t = t_{new}$.
- *Step II*. The velocity field at the flow front $\boldsymbol{u}$ is determined using eqn 7.1.
- *Step III*. Under the current velocity field, the shortest time to fill a new control volume, Δt_{min} is found. In Fig. 7.6(b), the mesh is removed to facilitate visualization and clearly show the smallest area that needs to be filled to saturate the next control volume. Assuming a homogeneous permeability field, it is clear that the control volume on the top-left will take shortest time to fill. Thus, Δt is taken such that this control volume is filled at the next time step.
- *Step IV*. The current velocity field $\boldsymbol{u}$ is applied on the resin flow for Δt_{min}, the new fill state is estimated and the time is adjusted $t_{new} = t_{new} + \Delta t_{min}$. Figure 7.6(c) shows the flow front at the next time step. The discrepancy between the previous and current flow front locations is highlighted with a different shade in the figure. Note that the top-left control volume is completely filled. Also, three new nodes become part of the resin domain at this time step.
- *Step V*. Stop if all control volumes are saturated, otherwise go to step I.

7.3.1 Features of LIMS

Interaction with LIMS

The numerical solver in LIMS is coupled with a scripting language LBASIC. The communication between the user and the solver is provided via a console

using LBASIC. The process parameters and commands to the numerical solver are entered from the console. Selected simulation output can be displayed on the console if desired. Also a graphical user interface (GUI) module is available to interact with LIMS, which provides *point-and-click* capability for most common steps. Using LIMS through the GUI module is easier, while the console and LBASIC provide the widest capabilities.

Interrogation of simulation at each time step

In LIMS, each Solve command executes a single loop of the five steps presented above. Therefore, one can intervene in the simulation at any time step and modify process and material parameters such as the preform properties, injection location and conditions, or vent locations. Moreover, one can retrieve data from the simulation at any time step. During the actual operation, the operator can intervene in the process and obtain necessary data.

Procedures

Procedures – batches of LBASIC commands – further facilitate the use of LIMS. One can create complex algorithms in LBASIC to try various filling scenarios, retrieve specific data and undertake control actions during mold filling, as illustrated below.

In Fig. 7.7, a step mold is partially filled and the injection has to be switched to a secondary gate. Three nodes, Gate A, Gate B and Gate C in the

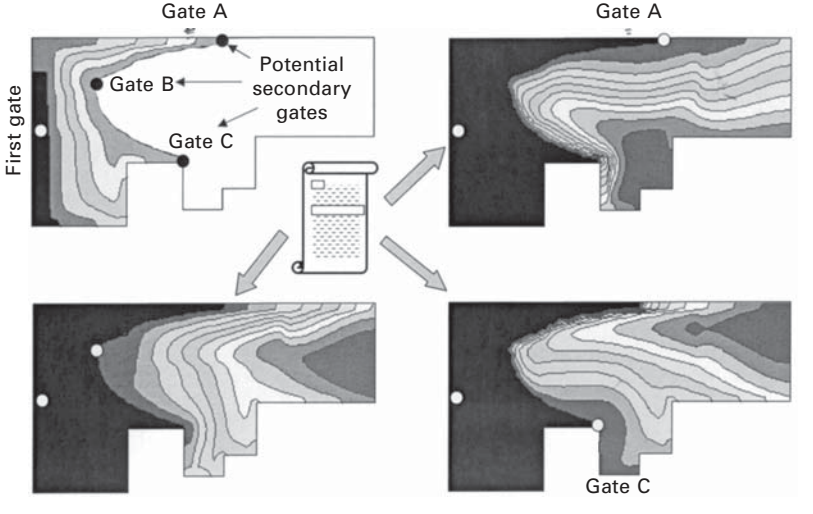

7.7 Filling contours at progressive times to demonstrate changes in filling patterns when injection gate is switched to secondary Gates A, B or C using the scripting procedures listed in Fig. 7.8.

figure, are chosen as the possible locations for the second injection location. Two procedures, *TestGates* and *SwitchGate*, are written to try each of these locations automatically. Initially, the first procedure fills the mold until resin arrives at Gate A and saves the mold filling state in the file *State.dmp*. Note that the resin arrives at Gates A, B and C simultaneously. Next, procedure *TestGates* calls the second procedure three times to try each of Gates A, B and C. Procedure *SwitchGate* loads the mold filling state from *State.dmp*, sets the second injection location and completes the mold filling simulation. The procedures are listed in Fig. 7.8 and the flow patterns at various time steps are illustrated in Fig. 7.7.

Tracers

A tracer simulates a sensor in the mold cavity. It follows the state of a given node and records the information either to a window on the screen or to a tab-limited ASCII file where each line contains the time and traced value. The tracers are valuable tools when one wants to use sensors in resin flow feedback control studies.

Virtual experimentation environment

LIMS can be called from other programs such as LabView and MATLAB® through dynamic linking, which provides seamless integration between the two environments and computational efficiency. There are two modes of data exchange between the LIMS subroutine and the master program:

1. *The text (command) data exchange*: in this mode, the master program behaves like a user sitting at the console, sending lines of commands to the LIMS subroutine and receiving lines of LIMS output. Buffers are used to store information during data exchange between the master program and the LIMS subroutine. Figure 7.9 illustrates schematically an instance of message traffic between MATLAB and LIMS. In the figure, the last command MATLAB put into the buffer is *print socurrenttime(),* which requests LIMS to print the current simulation time, and the last output LIMS put into the buffer in response to an earlier request is *342 345.231 10000*, which can be explained as *<node number>*, *<current simulation time, i.e. the duration before resin arrives at Node 342>*, *<pressure at Node 342>*. The computational overhead that comes with the message traffic limits the amount of data that can be exchanged between the LIMS subroutine and the master program.
2. *The binary data exchange*: in binary mode, shared memory blocks (memory-mapped file) are used to exchange data between the LIMS subroutine and the master program (Fig. 7.10). A shared memory block

```
REM Syntax: TestGates FirstGate, GateA, GateB, GateC, GateType, GateStrength
proc TestGates
  defint i, j, FirstGate, GateA, GateB, GateC, GateType, Flag1,
  defdbl Time, GateStrength
  let FirstGate=argument(1)
  let GateA=argument(2)
  let GateB=argument(3)
  let GateC=argument(4)
  let GateType=argument(5)
  let GateStrength=argument(6)
  let Flag1=1
  setintype "in"
  read "onrsmall.in"
  setgate FirstGate, GateType, GateStrength
REM Fill until the specified limit
  do while (Flag1)
    solve
    for i=1 to sonumberfilled()
      let j=sonextfilled()
        if (j=GateA) then
          let Flag1=0
          setgate FirstGate, 0, 0
          setouttype "dump"
          write "State"
          let Time=socurrenttime()
        endif
    next i
  loop
  REM Switch injection from the first gate to gates A, B and C
  SwitchGate GateA, GateType, GateStrength, Time, "State_GateA"
  SwitchGate GateB, GateType, GateStrength, Time, "State_GateB"
  SwitchGate GateC, GateType, GateStrength, Time, "State_GateC"
endproc
```

———————

```
REM Syntax: SwitchGate SecondGate, GateType, GateStrength, Time, OutFile
proc SwitchGate
  defint SecondGate, GateType, GateStrength
  defdbl Time
  defstring OutFile
  let SecondGate=argument(1)
  let GateType=argument(2)
  let GateStrength=argument(3)
  let Time=argument(4)
  let OutFile=argument(5)
  setintype "dump"
  read "State.dmp"
  settime Time
  setgate SecondGate, GateType, GateStrength
  do while (sonumberempty()>0)
      solve
  loop
  setouttype "tplt"
  write OutFile
endproc
```

7.8 Two procedures created to try three different filling scenarios.

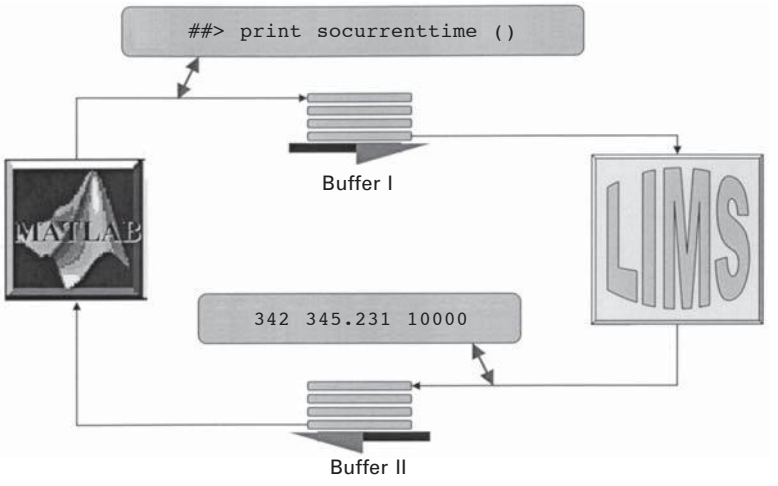

7.9 Text mode data exchange between MATLAB® and LIMS.

is essentially a data structure that contains all process information. Each shared block has a name and a certain organization, which allows the LIMS subroutine or the master program to access any specific data from the block: the fill factor of a certain node, for example. At any given time, either the master program or the LIMS subroutine can access the data block. Note that this exchange mode is binary and does not involve any actual data transfer between the master program and the LIMS

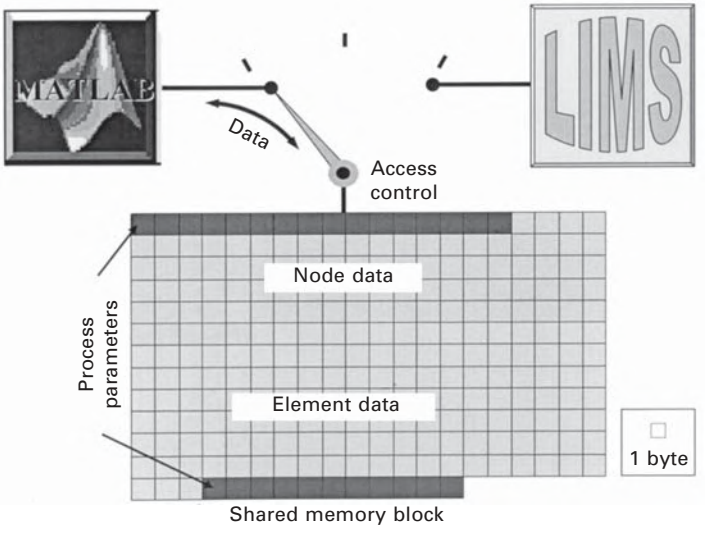

7.10 Binary mode data exchange between MATLAB ® and LIMS.

subroutine; in essence, two software programs share a certain portion of the RAM memory. Hence, it is very fast compared with text mode and is suitable for large volume data exchange such as providing data for a contour plot visualization.

The text mode is suitable for small amounts of data exchange and the binary mode is advantageous for large volumes of data exchange. If the same data are to be accessed repeatedly for a period of time, permanent memory can be used for data exchange. The majority of the study presented in this chapter was conducted in a virtual optimization and control environment created by the integration of LIMS and MATLAB® [37], a high-level programming language and an integrated technical computing environment that combines numerical computation, advanced graphics and visualization.

7.3.2 Process model in design, optimization and control

Several engineering practices, such as design, optimization and control, require a mathematical model of the physical system under study. A mathematical model imitates the process physics, and for a given set of process inputs, the model is expected to reproduce the same results as the actual system. For example, in the mold filling process, the inputs are the mold geometry, the gate locations, the injection conditions, the vent locations and the preform and resin properties, and the important outputs are the flow pattern, the fill time, dry spot formations and the pressure requirements.

In some cases an analytical mathematical model is available for the physical system under study:

$$F = f(x) \tag{7.5}$$

where x represents the process parameters and, f is an explicit function of x that maps process inputs x to the process output(s) F ($\in R$). Several design, optimization and control tools exist to address these types of situations. In other cases such as the mold filling process, an explicit function that relates the process inputs to the process outputs does not exist. Instead, LIMS is used as the mathematical model (also called the process model) of the mold filling process, which maps the process inputs to the process outputs. It provides a virtual testing environment, where one can try different designs, investigate different ideas and concepts, study input–output relations, etc. Common analytical tools in design, optimization and control fields do not apply in these cases, since an explicit form of f is not available. In the following two sections, the utilization of LIMS in the optimization and control studies is summarized.

Optimization studies

Several design choices exist for the mold in LCM processes. The optimization algorithms can help designers achieve the design that fits the performance criteria best. These algorithms require the mathematical model of the physical system to be optimized. When the mathematical model f is explicitly available, the optimal values of the process parameters x can be estimated using the standard procedures.

In the mold filling process, LIMS provides the input–output relationship. The cost functions are defined in terms of LIMS output. Several optimization algorithms that do not require an analytical process model are available for use with LIMS [38, 39]. These algorithms are usually iterative. At each iteration, the process is simulated with the design parameter values from the previous iteration. The cost function is evaluated using LIMS outputs. Next, the optimization algorithm calculates the new design parameter values, such as gate locations, for the next iteration. The purpose of all optimization algorithms is to converge towards the optimal solution by each iteration [40, 41].

Feedback control

During the manufacturing stage, feedback control may be necessary to offset the adverse effects of the disturbances and fill the mold successfully. It is straightforward to simulate the control hardware. Ability to interrogate the simulation at each time step allows one to simulate actuator actions such as opening/closing a gate and modifying the injection conditions. Sensors are simulated by using the LIMS output and the tracer data at each time step. The LBASIC procedures are extremely helpful for these purposes.

In the feedback control, once the sensor data have been retrieved from the LCM mold and processed, the optimal control action must be generated by the controller and sent to the actuators (the gates) to drive the resin flow in the desired direction. The controller usually will employ a process model to predict the responses to various actuator actions. For such methodology, LIMS can serve as the mold filling process model.

7.4 Gate location optimization

7.4.1 Problem statement

In this section, a gate location optimization problem is stated [39]. The cost function (also called the performance index) is expressed in terms of LIMS output. An assumption on the cost function f is verified using LIMS simulations.

The single gate optimization problem in LCM can be stated as follows:

> Given a non-empty, closed set $D \subset R = \{\text{integer}\}$ and a continuous function $f : D \rightarrow R$, find at least one point $x^* \in D$ satisfying $f(x^*) \leq f(x)$ for all $x \in D$.

In LCM, x correspond to a node in the finite element mesh where a gate can be placed and set D consists of all possible x values. f is the cost function that needs to be minimized. Note that an analytical expression is not available for f. Instead LIMS output is used to estimate $f(x)$ value. Two assumptions are made about f.

> **Assumption I:** $f(x)$, $x \in D$, is continuous.

Since f is not available, it is impossible to apply standard tests to prove this assumption. Instead, a case study is presented for verification using simulations.

The bottom picture in Fig. 7.11 is a simplified mesh of a bus chassis. There are two high fiber volume fraction regions in the geometry as illustrated in the figure. Flow resistance is much higher in regions with a high fiber volume fraction. It is desired to find the injection location for a single gate that will fill the mold in minimum time. The injection would be done under a constant pressure boundary condition. In order to achieve this physically, the resin reservoir is pressurized and held under constant pressure until the resin reaches the last vent. All nodes were tried as injection locations (exhaustive search) and corresponding fill times are shown with two surface plots in Fig. 7.11. In the plots, the z axis shows the fill time. The lower a node is on the z axis, the less time it takes to fill the mold. The middle picture in Fig. 7.11 shows the overall exhaustive search results. As expected, the nodes in the high-volume fraction regions are not suitable as the gate location: it takes much longer to fill the mold if the injection location is in these regions. Note that in the middle picture, the results of the high-volume fraction region dominate the plot; therefore the fill time variation in the remaining region cannot be further discriminated. In the top picture in Fig. 7.11, the results of the high-volume fraction region are removed from the plot, making the behavior of the remaining nodes visible. As expected, the injection locations in the middle of the geometry will fill the mold in shorter times. Note that plots in both middle and top pictures are continuous, hence they verify Assumption I.

> **Assumption II:** $\mathrm{d}f/\mathrm{d}x$ is small and of the same order throughout the mesh surface, where $\mathrm{d}x$ represents spatial differential of node x in the mesh.

7.4.2 Branch and bound search

The branch and bound search (BBS) is used as the optimization algorithm [42, 43]. BBS converges on the optimal solution by dividing the solution set into smaller sets and eliminating the sets that are unlikely to include the

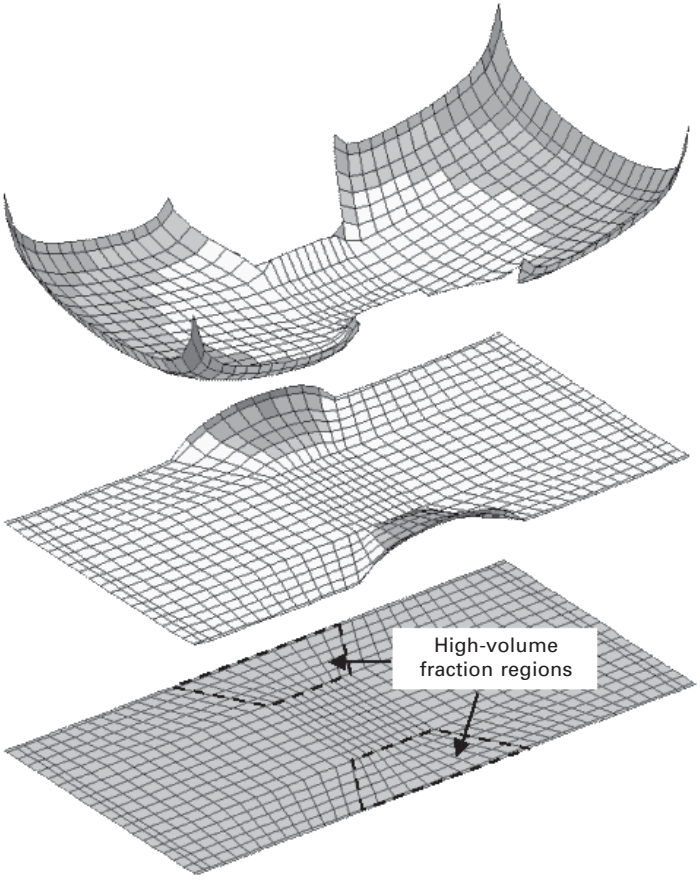

7.11 Bottom: simplified mesh of bus chassis with two high-volume fraction areas. *Middle*: Surface plot of exhaustive search results. The gate is desired at a location that will minimize fill time. High-volume fraction regions return high fill times and dominate the plot. *Top*: The results of high-volume fraction region are removed from the plot, which clearly shows that the gate should be placed at the center.

optimal solution. This process is repeated until it is no longer possible to partition a set or a stop criterion is met. In order to apply BBS to an optimization problem, it should satisfy two requirements.

> **Requirement I**: Given a solution set, it should be possible to estimate a lower bound for the function f.

A lower bound for a solution set S_i, $i = 1, 2 \ldots n$, denoted as $\beta(S_i)$, satisfies the condition $f(x) \geq \beta(S_i)$, $x \in S_i$. The only way to find a lower bound for a set in the current case is to use LIMS with each node in the set, which

amounts to impractical exhaustive search. Hence, in this study, the lower bound is replaced with a qualitative parameter as follows.

Owing to the physics of the problem, f can take in multiple values and return a single value: $f = f([x_1, x_2 \ldots x_n])$, $x \in D$, i.e. multiple gates can be used simultaneously to fill the mold, which will yield a single flow pattern that will return a single f value. Given a set S_i, the pseudo-average of f over the set is defined as $\bar{f}_{S_i} = f(S_i)$, i.e. all nodes in the solution set S_i are simultaneously designated as gates and the subsequent value of the cost function f is assigned to $\bar{f}_{S_i}$. A third assumption is derived from Assumption II as follows:

> **Assumption III**: For the sets at the same partitioning level, the differences between the pseudo-average $\bar{f}_{S_i}$ and the unknown lower bound $\beta(S_i)$ is of the same order: $\varepsilon_i \sim \text{avg}(\varepsilon_i)$, where $\varepsilon_i = |\bar{f}_{S_i} - \beta(S_i)|$.

According to Assumption III, $\bar{f}_{S_i} = \beta(S_i) \pm \varepsilon_i$. Since ε_i varies slightly for sets under evaluation, $\bar{f}_{S_i}$ can replace unknown $\beta(S_i)$ for the purpose of ranking the performances of various solution sets.

> **Requirement II**: There should be a way to partition a given solution set.

The solution set is partitioned according to geometrical guidelines (Fig. 7.12). Although there are standard partitioning methods in BBS, none has yet been proven to be applicable to the mold filling problem. A rule of thumb

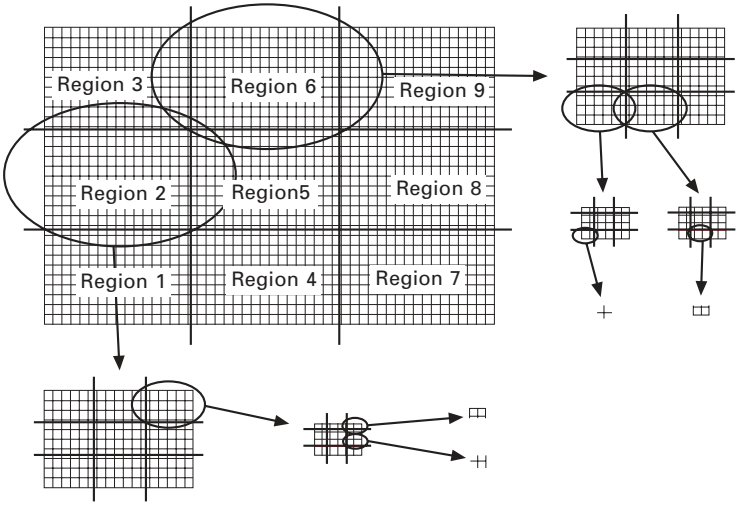

7.12 Recursive domain reduction in branch and bound search while converging on the optimal solutions.

is to partition the set in a way to validate Assumption III. A fine partitioning should be used for sets that include high gradients of f, whereas sets with low gradients may perform well with a coarse partitioning. A major cause of high gradients is significant variations to the permeability distribution within the area covered by the set. In this study, homogeneous, equal partitioning is used regardless of the permeability field in the mold.

Procedure

The algorithm of the BBS is explained step by step below. The nodes in the entire mesh are taken as the first solution set.

- *Step 1*: Partition the set(s) into subsets to form a new group of smaller sets for evaluation.
- *Step 2*: For each set in the group estimate $\bar{f}_{S_i}$.
- *Step 3*: Choose the set with $\bar{f}_{\min} = \min(\bar{f}_{S_i})$. Also choose the sets whose $\bar{f}$ values are close to $\bar{f}_{\min}$ in order to compensate for the impreciseness in Assumption III.
- *Step 4*: Remove the remaining sets from the search space.
- *Step 5*: If the chosen sets include suffcient number of nodes for partitioning, go to Step 1. Otherwise, simulate mold filling for each node in the chosen set(s), take the best solution and Stop. In this study, partitioning is continued until there are four or fewer nodes in a chosen set.

A schematic explanation of the procedure is given in Fig. 7.12: A 3×3 partitioning scheme is used throughout the solution. In the first iteration, sets 2 and 6 give superior performance as compared with other sets and hence, are selected for the next level of subdivision. In order to reach the optimal solutions, three iterations were suffcient as illustrated in the figure.

In the following section, BBS is used to find the gate location in a box geometry that will fill the mold in minimum time.

7.4.3 Case study: minimum fill time

During an injection system design, filling the mold as quickly as possible is an important goal as it will reduce the cycle time and increase the profitability of the process. Also for quick-curing resins, it lowers the possibility of resin gelling and hardening before the mold is completely filled. The mold of interest and its mesh are illustrated in Fig. 7.13(a). It is a two chamber, $65 \times 30 \times 25$ cm^3 hollow box, and the dividing wall has a circular hole in it. The mesh of the mold has 3378 nodes and 3316 elements.

An injection system with a single gate is designed. The resin is injected through the gate under the constant pressure of 0.2 MPa. The resin viscosity is assumed to be 0.1 Pa s. The preform is assumed to be isotropic with a

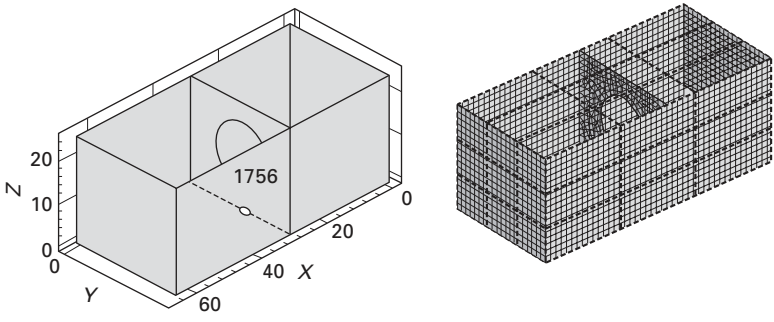

7.13 Left: box mold. *Right:* the mesh of the box mold and partitioning scheme.

permeability of 10^{-6} m^2. The gate is desired at a location on the mold geometry that will minimize the fill time. Hence, the cost function for this problem is as follows:

$$f = f(x)\text{: the fill time} \qquad 7.6$$

where x is the location of the single gate. The vents are placed in the last regions to fill or the mold can be assumed to be under perfect vacuum, so the possibility of having dry spots is non-existent. For a given set S_i, pseudo-average $\bar{f}_{S_i} = f(S_i)$ is estimated by equating the injection pressures of each node in the set to the preselected constant pressure value, $\forall x \in S_i$, $P(x) = P_{\text{injection}}$ and then simulating mold filling using LIMS.

Initially, the problem is solved using the exhaustive search (ES). After 3378 simulations, ES showed that the optimal gate location is at Node 1756 (x = 30 cm, y = 16.5 cm, z = 0 cm) with a fill time of 1000 seconds. Node 1756, which is located on a hidden line, is marked with an ellipse in the left-hand figure in Fig. 7.13. During BBS, a $3 \times 3 \times 3$ partitioning is applied throughout the optimization procedure. After a total of 3 iterations and 57 simulations, BBS arrived at the same result. Overall, BBS was 98% more efficient computationally than ES, which illustrates the advantages of optimization algorithms. More details and examples can be found in Gokce [5] and Gokce and Advani [44].

7.5 Disturbances in the mold filling process

During the mold filling stage of LCM processes, the textile sheets must be completely saturated with resin. The gates and the vents must be placed appropriately to ensure complete saturation. Usually, the gate locations are chosen first to achieve certain objectives such as minimum fill time, and minimum pressure requirements. Next, the vents are placed at locations

where resin arrives last.[1] Such design decisions are made based on the process model and subsequent simulations. If the actual values of the process parameters are significantly different from the predicted values, then the subsequent designs may fail to satisfy the intended objectives.

The constitutive relationship between the resin velocity field and the pressure field in the mold cavity is a function of the resin viscosity and the permeability field as stated by eqn 7.1. Variations in these two parameters may cause the mold filling stage to go astray, resulting in a defective part. In the mold filling process, the fill time and the flow pattern are important output variables. The fill time is the total duration of the mold filling process and is a function of several parameters such the resin viscosity, permeability field and the injection conditions. The flow pattern can be defined as the filling sequence of the mold cavity by the resin. The flow pattern is a function of the normalized form of the permeability field in the mold cavity. The fill time and the flow pattern are independent of each other.

The variations in the resin viscosity and the permeability field cause the fill time and the flow pattern to vary. Variations in the fill time are tolerable. A very small fill time implies fast filling of the mold, which may cause micro-bubbles in the fiber tows, an issue not addressed here. If the mold filling stage takes too much time, resin may start gelling, which will complicate and possibly fail the mold filling operation. On the other hand, variations in the flow pattern may cause significant defects in the composite part. Since gates and vents are placed into the mold based on a predicted flow pattern, a moderate alteration in the flow pattern due to disturbances may cause the gate and vent design to fail. Hence, variations in the flow pattern are more critical than the variations in the fill time. Some disturbances that may influence these two outputs are summarized below.

- *Resin viscosity*: Variations in the resin viscosity η, may cause the resin to flow slower or faster and affect the fill time. Under certain conditions, the isothermal-Newtonian flow assumption may fail. If the resin begins to gel before the entire mold is filled owing to faulty chemical composition, its viscosity will increase by several orders. Consequently, the resin flow will slow down in certain parts of the mold cavity and alter the flow pattern.
- *Defects in the preform*: Manufacturing defects or impurities in the textile preform may cause local variations in the permeability field. As a result, resin may flow faster or slower at certain parts of the mold, changing the flow pattern. Note that major preform defects can be detected easily before

[1]Note that the term *last* is not used in the chronological sense. It means the last region to fill in a contiguous dry area, after which the dry area disappears, regardless of the time scale.

the preforms are placed into the mold and minor defects do not cause significant disturbances. Hence, this is a minor issue.

- *Textile preform compaction during mold closing*: In LCM processes, the textile sheets in the mold cavity are under pressure. (This pressure is not related to the injection pressure applied at the gates.) In vacuum-assisted processes with single-sided molds, atmospheric pressure is applied on the textile sheets through the plastic covering. In matched die molds, the pressure on the preform can be much higher, depending on the number of preform layers and the preform architecture. Depending on the pressure level, the fiber architecture may change in various ways, affecting the shape of the flow channels, which determine the permeability of the porous medium, as illustrated in Fig. 7.14(a). In general, compaction affects the preform permeability globally, hence it may affect the fill time but not the flow pattern.
- *Interaction of textile layers during mold closing*: Since architecture of most textile preforms consists of repeated patterns, there are regions with

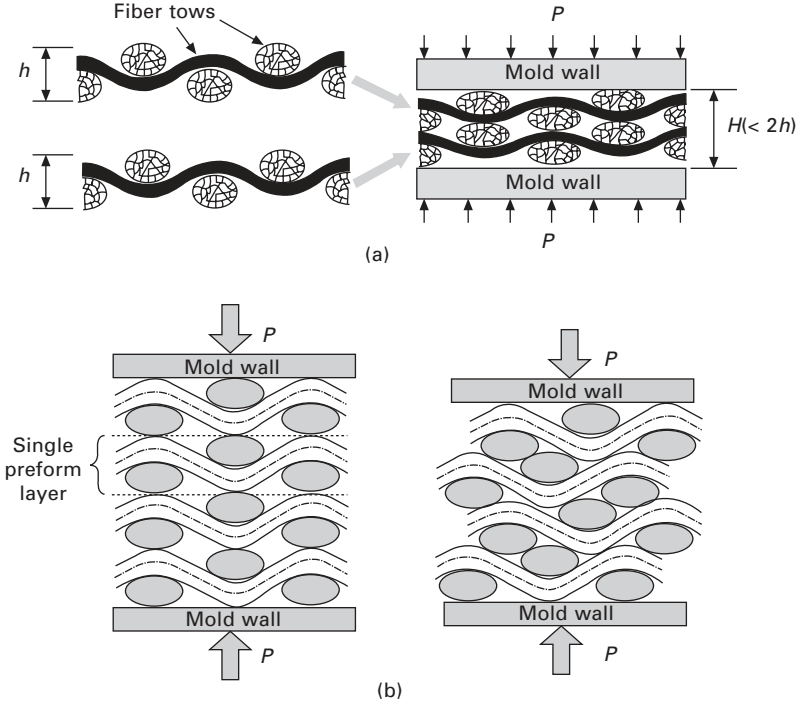

7.14 Interaction of preform layers in a closed mold: (a) *compaction*: the preform layers become thinner under pressure; (b) *nesting*: preform layers mesh with each other under pressure. There is no nesting on the left figure, whereas there is a significant level of nesting on the right figure.

high and low fiber fractions. Under pressure, the textile preform layers protrude into each other as illustrated in Fig. 7.14(b), a phenomenon called the *nesting effect*. The level of nesting effect is a function of the relative position of textile sheets with respect to each other and the applied pressure on the textile preform. The nesting effect influences the structure of flow channels in the mold cavity, hence the permeability field of the porous medium. Its effect on the permeability field is global, hence it does not affect the flow pattern. In this case the nesting effect is related to the compaction of textile sheets.

- *Accidental flow paths in the mold cavity*: Especially in matched die molds, the mold cavity is rigid. Achieving an exact fit between the textile preform and the mold cavity is a difficult challenge. When there are gaps between the inner mold surface and the textile preforms, channels that offer low resistance to resin flow may be created unintentionally in the mold cavity. Resin flows faster in these channels, altering the flow pattern significantly, a phenomenon known as *racetracking*. Figure 7.15 shows an example of altered flow front due to a gap along an edge. These channels, called *racetracking channels*, are more likely to form at certain locations in the mold as shown in Fig. 7.16. Several researchers have attempted to model these channels and their effects on the flow pattern [47–53]. Traditionally, the textile preform is assumed to fit the mold cavity exactly. However, because of process variations during preform cutting/placement and preform compaction mechanisms during mold closing, it is diffcult to achieve a perfect contact between the bulk preform and the inner mold surface. Consequently, racetracking emerges as the most common disturbance in the mold filling stage of the certain LCM processes.

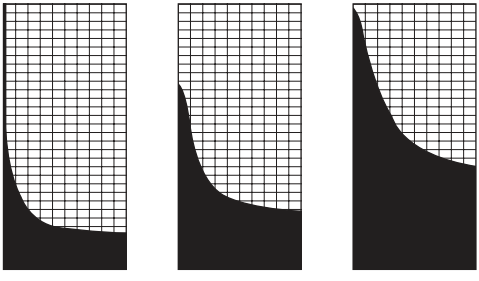

7.15 Experimental snapshots of racetracking along the left edge of a rectangular mold cavity [45, 46]. The resin enters the mold cavity from a line injection gate along the upper edge. Horizontal flow fronts would be developed if there was no racetracking.

The flow pattern, the key measure of successful mold filling, is a function of the racetracking conditions, which depend on the state of the contact between the textile preform and the inner mold surface. Since the contact

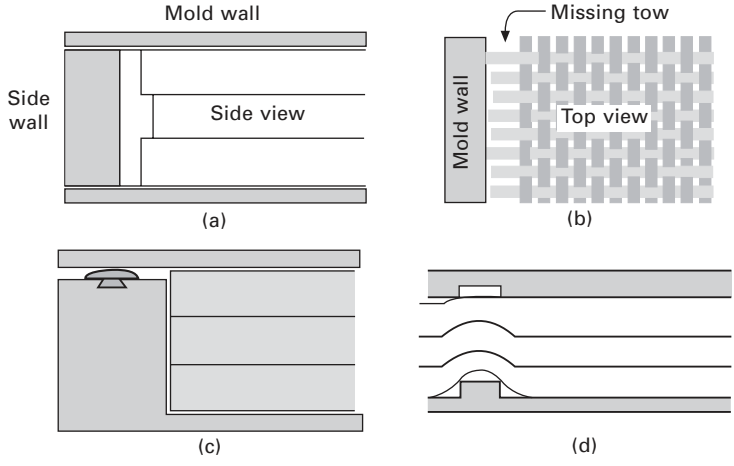

7.16 Various situations that cause racetracking: (a) poor dimensional control during perform cutting; (b) low volume fraction at the edges, possibly due to missing fiber tows; (c) insufficient mold closing; (d) poor mold design.

state is unrepeatable from one experiment to the other, racetracking is a major cause of process unrepeatability in the mold filling process. Because of its frequent occurrence and significant adverse effects, racetracking is the only disturbance studied in this chapter. However, the tools and methodologies developed for racetracking can be applied to other disturbances.

7.5.1 Modeling a racetracking channel

A racetracking channel is created because the resistance to flow along a certain path is affected by the type of fiber architecture, precision of a cut and placement of the textile preform. Resin flow through a racetracking channel usually meets a lower resistance than the textile preform, hence permeability along a racetracking channel is higher. The resin flow in the channel can be modeled as slow, fully developed, steady-state viscous duct flow and one can develop an equivalent permeability expression for it in terms of channel dimensions as [49, 52, 54]:

$$K_{rt} = \frac{a^2}{12}\left[1 - \frac{192a}{\pi^5 b}\sum_{i=1,3,5..}^{\infty}\frac{\tanh\left(i\pi b/2a\right)}{i^5}\right] \qquad 7.7$$

where K_{rt} is the equivalent permeability of the racetracking channel, b is the distance between the preform and the mold wall and a is the height of the mold cavity (Fig. 7.17). Note that the wider the gap between the preform and the mold wall, the stronger will be the racetracking.

The equivalent permeability of the racetracking channel in eqn 7.7 is not

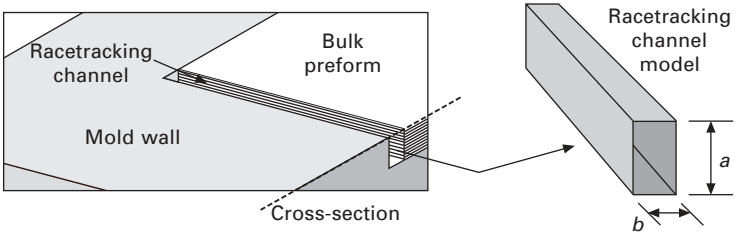

7.17 Modeling of resin flow in the racetracking channel as duct flow.

suffcient to quantify racetracking alone. The ratio of the equivalent permeability K_{rt} to the textile preform permeability $K_{preform}$ is chosen as a measure of the racetracking strength;

$$\rho = \frac{K_{rt}}{K_{preform}} \tag{7.8}$$

where ρ is the racetracking strength. Note that $K_{preform}$ can vary by several orders of magnitude for various preforms. Table 7.1 shows racetracking strength for five different preforms with an identical racetracking channel of 0.5 mm wide and 6.35 mm high. In the simulation environment, these five preforms are placed in a rectangular mold successively such that a 0.5×6.35 mm^2 racetracking channel is along the top edge. The injection gate is placed on the left edge and mold filling is simulated under constant flow rate injection for all five cases: $\rho = \{1, 4.1, 52.5, 124.5, 562.5\}$. Note that $\rho = 1$ means there is no racetracking in the mold. The flow front positions at the same time step for all five cases are superimposed in Fig. 7.18. The higher the racetracking strength ρ, the more resin flow deviates from the nominal case ($\rho = 1$). Figure 7.18 shows that even if the racetracking dimensions are identical in all the cases, racetracking takes place at varying levels as it is a function of the permeability of the textile preform as well.

A racetracking channel is not likely to have a perfect duct shape as in Fig. 7.17. The dimensions of the channel, a and b, in eqn 7.7 may vary along the channel; $a = a(s)$ and $b = b(s)$, where s is the coordinate along the length of

Table 7.1 Racetacking strengths for various performas with identical racetracking channels

Type of preform [55]	Preform permeability (m^2)	Racetracking strength, ρ
Random glass fiber	4.88×10^{-9}	4.1
3D woven glass fibers	3.77×10^{-10}	52.5
Unidirectional (warp) woven glass fibers	1.59×10^{-10}	124.5
Non-woven stitched glass fiber	3.53×10^{-11}	562.5

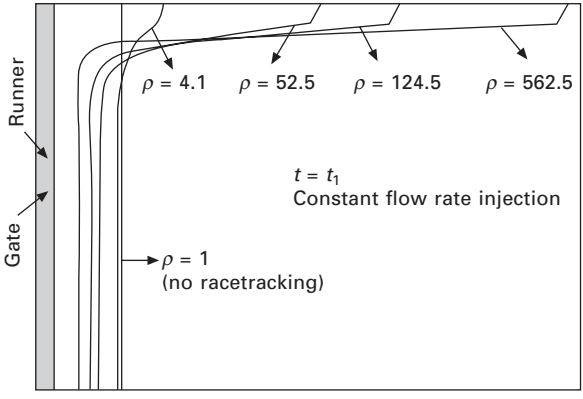

7.18 Flow front locations at the same time step for five different racetracking strengths.

the channel. Hence, $K_{rt} = K_{rt}(s)$ and $\rho = \rho(s)$. Since racetracking is unrepeatable and may appear in many different forms and strengths, it is not straightforward to model $\rho(s)$ in the simulation environment. Thus, researchers have assumed that racetracking is uniform along a racetracking channel. Gokce and Advani justified this assumption [44].

7.5.2 Experimental measurement of racetracking

A rectangular mold with an impermeable L-shaped insert, called the L-mold, has been designed [54]. The flow patterns in the mold were studied in three stages: (i) the simulation stage, (ii) the experiment stage and (iii) the racetracking analysis stage.

Simulation stage

Five potential racetracking channels were identified in the mold as illustrated in Fig. 7.19. During a moldfilling experiment, the racetracking strength along a channel can be of any value. Since it is not possible to include all ρ values in the study, a finite set of ρ values, called a *racetracking set*, is selected to represent the entire ρ range of a channel. During an experiment, the actual racetracking strength in a channel will be approximated by the closest value from its racetracking set. Thus, the continuous ρ range for the racetracking channel is discretized into a finite number of ρ values. The more elements there are in the racetracking set, the better the actual racetracking strength can be approximated.

The racetracking conditions in channels I, II, III and IV were modeled by the racetracking set $\mathscr{R} = \{3, 7, 14, 32, 70\}$, and channel V was modeled by the racetracking set $\mathscr{R} = \{2, 6\}$. By taking one value from the racetracking

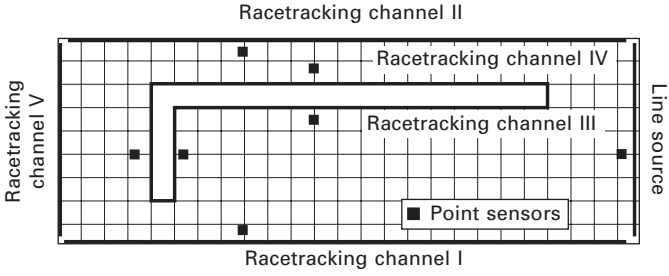

7.19 Potential racetracking channels and sensor locations in the L-mold.

set of each channel, 1250 ($5 \times 5 \times 5 \times 5 \times 2$) racetracking scenarios were created. The collection of all scenarios is called a *scenario space S*.

The mold filling was simulated for all 1250 racetracking scenarios.[2] Seven point sensor locations were identified in the mold for racetracking measurements (Fig. 7.19). A table that includes resin arrival times at the sensors for all scenarios was created from the simulation results. The table, called the *detection table*, would be used to compare simulation results with the experimental arrival times to identify the racetracking scenario that is closest to the mold filling state in the mold.

Experiment stage

A rectangular mold and an L-shaped insert were manufactured and assembled to create an L-mold. Point sensors and a CCD camera were used as the sensors (Fig. 7.20). Fifty mold filling experiments were conducted using the same mold and materials under the same processing conditions. During each experiment, resin arrival times at the point sensors were recorded to identify the closest scenario from the scenario space *S*. Note that actual racetracking strength in a racetracking channel will probably not be equal to any of the values in the racetracking set associated with the channel. Consequently, an actual flow pattern will not exactly match any of the 1250 racetracking scenarios. However, this is a source of error common to all discretization operations. If the discrete case is suffciently close to the actual case, then the results returned by the discrete case will be within the range.

[2]To make the text more readable, the term *scenario* will be used to represent a *mold (filling operation) with specific racetracking conditions*. Therefore, the phrases a *scenario is filled/drained/saved* must be understood accordingly.

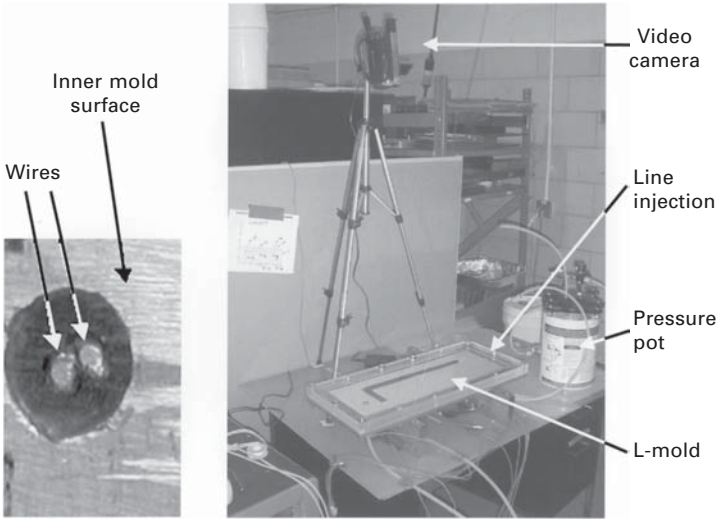

7.20 (a) A point sensor; (b) Experimental set-up [56].

Racetracking analysis

The flow pattern of each experiment was approximated by a racetracking scenario using the detection table. Thus, 50 ρ measurements were obtained for each of the five racetracking channels in the mold. The frequency of the elements in set $\mathscr{R}_i$ of racetracking channel i is displayed and plotted in Fig. 7.21. The data show that racetracking occurred frequently at varying levels in all channels, which illustrates the significance of racetracking.

7.5.3 Successful mold filling despite racetracking

Traditionally, in RTM processes the gate locations are selected first and then vents are placed at the last-filled regions. The case without any disturbances is called the *nominal case* and the corresponding vent configuration is called the *nominal vent configuration*. Racetracking even at moderate levels can alter the flow pattern significantly and cause the resin to arrive at the vents earlier, blocking the air drainage. The nominal vent configuration, which was designed for the nominal flow pattern, cannot drain the air successfully for an altered flow pattern. There are two approaches to address the disagreement between the altered flow pattern and the nominal vent configuration:

1. *Active control*: One way is to counteract the influence of racetracking on the flow pattern using feedback control. The resin flow is steered by modifying the injection conditions at the gates towards the existing (nominal) vent configuration so that all air is drained from the mold cavity.

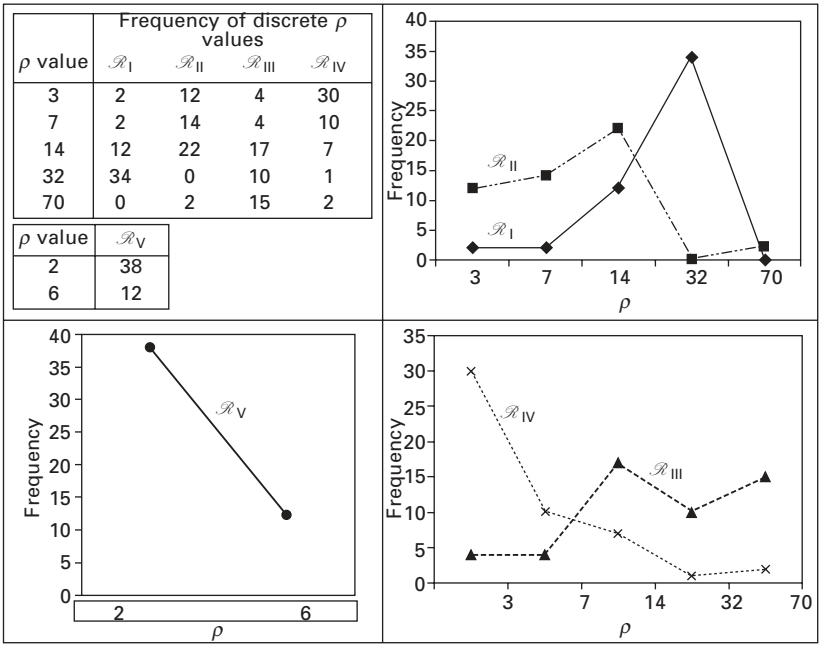

ρ value	Frequency of discrete ρ values $\mathscr{R}_{I}$	$\mathscr{R}_{II}$	$\mathscr{R}_{III}$	$\mathscr{R}_{IV}$
3	2	12	4	30
7	2	14	4	10
14	12	22	17	7
32	34	0	10	1
70	0	2	15	2

ρ value	$\mathscr{R}_{V}$
2	38
6	12

7.21 Experimental outcomes for racetracking channels in the L-mold.

2. *Passive control*: The vents act as constraints on the mold filling process by dictating the last points resin must arrive for a successful mold filling. Instead of driving the resin towards a nominal vent configuration as in feedback control, one might take the inverse approach and augment the nominal vent configuration by adding more vents, hence relaxing the constraint on the mold filling process. A suffcient number of vents can be placed optimally in the mold such that there will always be a vent in the vicinity of a region where resin arrives last.

7.6 Active control

The central idea in feedback control is to manipulate the resin flow in the mold cavity by modifying the injection conditions at the gates. A feedback control system has three major components:

1. *Data acquisition hardware*: This includes the sensory system and signal processing circuitry. The sensory system provides data from the closed mold, which enables one to track resin flow in the mold cavity. The sensors used to monitor mold filling can be direct current (DC), dielectric, optic, ultrasound or microwave-based, and can be classified in various ways depending on the method used, such as point-sensing versus

continuous-sensing sensors, or intrusive versus non-intrusive sensors. The variables that are measured by the sensors can be conductivity, impedance, electric current and reflection properties of light/laser beams, ultrasound waves or microwaves. Signal processing cards usually come with the sensory system, otherwise these are available off-the-shelf.

2. *Controller*: This is a computer program that can evaluate the incoming process data and generate input signals for the gates that will manipulate the resin flow in the desired direction.
3. *Actuators*: These are the controllable process inputs that drive the physical system. In the mold filling process, the only actuators are the injection gates in the mold. One can manipulate the resin flow by varying the injection conditions at the gates.

The control methods that were used for the mold filling process can be divided into two as *set point-based control* and *scenario-based control*. In set point-based control, the injection system with two or more gates and *a* certain number of vents is designed at first. A target flow pattern – usually the nominal flow pattern – is designated. During the mold filling operation, the control is conducted periodically: during a *sampling time* Δt, the flow front position is determined through the sensors and is compared with the target flow front position at the current time step. The error is estimated and, based on the *traction error*, the controller generates the optimal input signals for the injection gates to minimize the error between the actual and target flow front position. Neural networks, adaptive control and model-based control are some of the set point-based control methods [57–61].

There is an offine stage and an online stage in the scenario-based control. In the offline step, the injection system is designed for the nominal case. A scenario space that aims to model the disturbances is created. The sensory system is designed and detection tables are created to identify scenarios in the closed mold. Auxiliary injection gates are placed into the mold. Using various algorithms, control actions that fill each scenario successfully are determined, concluding the offline stage. The online stage can divided into two: the *recognition step* and the *control step*. During the recognition step, the sensory system tracks the resin flow and associates it with a scenario from the scenario space. Once the closest scenario has been found, the associated control actions are undertaken in an open-loop manner. Decision trees, genetic algorithms (GA) and ES are used for scenario-based control [7, 62, 63].

7.6.1 Simulation-based liquid injection control (SLIC)

A scenario-based learning control system has been developed at the University of Delaware [63]. The system, named Intelligent RTM, consists of an offline

stage called simulation-based liquid injection control (SLIC) and an online stage called AutoRTM, which is a LabView program. Intelligent RTM has eight modules:

- *Level 0*: Given the mesh of the part, nominal material parameters and the disturbance ranges, a scenario space is created.
- *Level 1*: The injection system for the disturbance-free case is designed. Optimal gate and vent locations are determined simultaneously using GA.
- *Level 2* (Only for LCM processes that utilize distribution media): The distribution media for the part is designed for the disturbance-free case.
- *Level 3:* The locations of the auxiliary gates that will undertake control actions and the locations of the point sensors that will activate the gates are determined optimally using GA. The auxiliary system is tested in the scenario space.
- *Level 4:* A sufficient number of vents are placed optimally in the mold using GA and detection tables are created to choose the scenario from the scenario space that is closest to the actual mold filling state.
- *Level 5:* The data from the offline stage are converted into a form (Lab View format) that is usable by the online components of the system. This step completes the offline stage of the control system. The mold filling operation can be initiated and controlled using the data from the offline stage.
- *Level 6:* When a racetracking scenario that does not belong to the scenario space takes place during mold filling, it is added to the detection table and control actions that will fill the scenario successfully using the existing hardware are sought offline. This *learning* ability gives flexibility to SLIC.
- *Level 7* (under development): Performance statistics reports that include the composite quality, cycle time and cost are prepared automatically.

7.6.2 Case study: rectangular mold with triangular insert

SLIC is demonstrated on a rectangular part with a triangular insert as shown in Fig. 7.22. The top and bottom edges, and three edges of the triangle are identified as potential racetracking channels. In all channels, the racetracking strength is modeled with the racetracking set $\mathscr{R} = \{20, 100\}$, which yields a scenario space with $2^5 = 32$ scenarios. The resin is injected from two injection lines on the left and right edges of the geometry. Auxiliary gates are placed optimally into the mold and the control actions that fill each scenario successfully are determined in level 3. In level 4, the scenario detection sensors are placed into the mold and a detection table is created. The snapshots from an experiment are illustrated in Fig. 7.23 along with the flow pattern of the associated scenario, scenario 29 with $\rho = 100$ in channels 1, 2 and 5 and $\rho = 20$ in channels 3 and 4. After the detection stage, the control actions

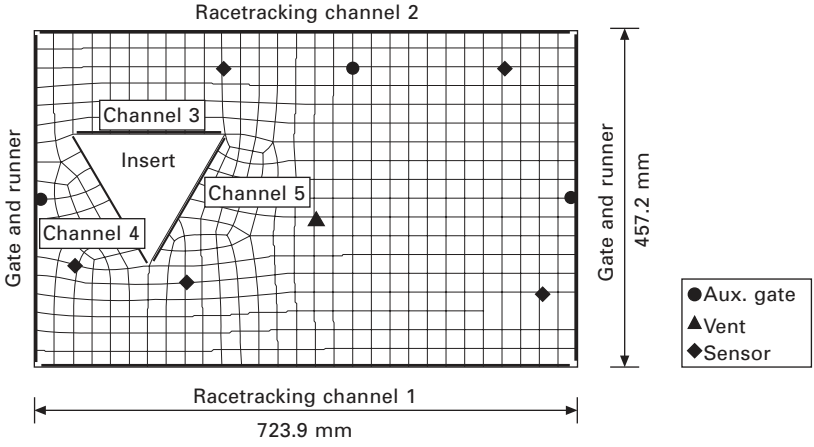

7.22 The mesh of the part used for the SLIC demonstration. The detection sensors and the auxiliary gate locations are also shown in the figure.

associated with scenario 29 – close all injection gates and open the auxiliary gate at the top – were taken to complete the mold filling successfully, which would otherwise fail.

7.6.3 Gate effectiveness

The mold filling process is irreversible: the wetted region always expands, it does not shrink. It is impractical, if not impossible, to reverse the process by sucking the resin back out of the mold. Mathematically, feedback control allows one to control the pressure at a certain number of points in the mold cavity, thus modifying the pressure gradients that drive the resin flow. However, owing to the process physics, the effects of such control on the pressure gradients are highly diffusive and lack any directional preference. Hence, as the resin flow front moves away from the gates, the ability of the gate to manipulate the resin flow, called the *gate effectiveness*, is diminished.[3] There is only a limited time window within which a gate can significantly modify

[3] From the *control theory* perspective, the loss of gate influence in steering the flow front indicates loss of *controllability*, which is defined as the ability to drive a dynamic system from an initial state to a target state in finite time [64]. The dynamic systems that are governed by partial differential equations such as mold filling process are called *distributed parameter systems* (or infinite dimensional systems) [65–67]. Theoretical operator, Hilbert uniqueness and moment are some of the methods used to investigate controllability of distributed parameter systems [68–70].

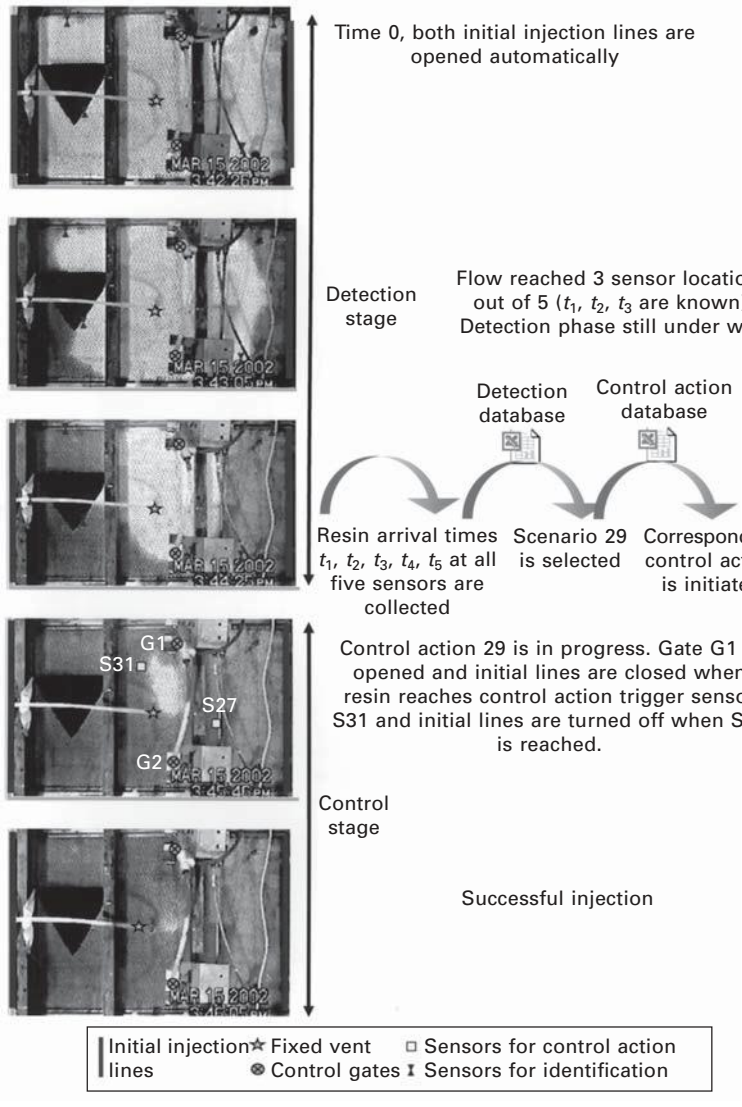

7.23 Snapshots from a mold-filling experiment. The flow pattern was identified as scenario 29 from the scenario space and the associated control actions were taken to achieve complete filling.

the resin flow pattern. This phenomenon is illustrated in the simulation environment with a case study below.

Mold III, a long rectangular mold with a line resin source on the far left and an injection gate on the bottom edge, is designed as illustrated in Fig. 7.24(a). Resin proceeds in straight lines from left to right. A coordinate system is attached to the mold such that its origin coincides with the point

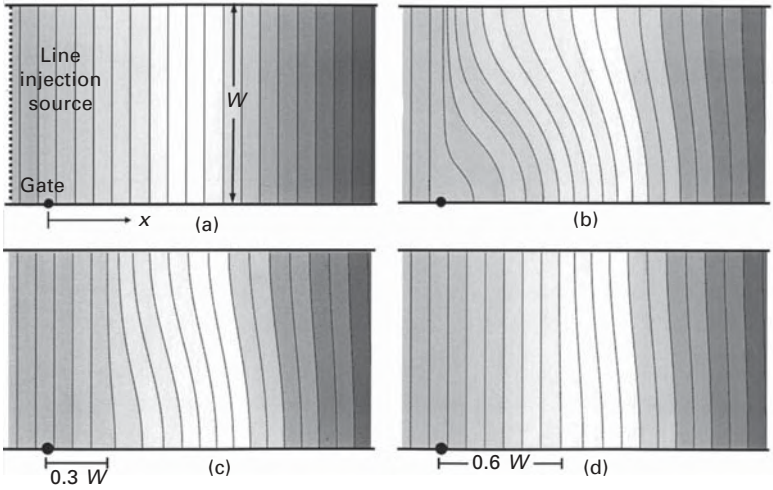

7.24 (a) Mold III, a rectangular mold with a line injection at the left and an injection gate at the bottom. (b) The gate at $x = 0$ is switched on as soon as the flow reaches it. (c) The gate at $x = 0$ is switched on after the flow reaches $x = 0.3W$, where W is the width of the mold. (d) The gate at $x = 0$ is switched on after the flow reaches $x = 0.6W$. In all cases, the flow proceeds from left to right from a constant flow rate line injection source on the left. When the gate is switched on, the line source is switched off.

gate location and its x axis is aligned with the flow direction. Principal directions of the permeability tensor are aligned with x and y directions and the preform is isotropic: $K_{xx} = K_{11} = K_{yy} = K_{22}$. The gate is initially closed. In the first case, the gate is switched on as soon as the flow front arrives there (Fig. 7.24b). In the second case, flow is allowed to proceed until $x = 0.3W$, where W is the width of the mold (Fig. 7.24c), before the point gate is switched on. In the final case, the gate is turned on when the flow is at $x = 0.6W$ (Fig. 7.24d). In all cases, the line source at the left edge is turned off when the gate is turned on. The simulations show that the effect of the gate on the flow front strongly depends on the position of the gate location with respect to the flow front position.

Since the flow front is continuously steered through a set of injection gates in set point-based control, the gate effectiveness is more crucial in this case. The gate effectiveness has been addressed as a secondary topic in a few studies [58, 60]. Gokce and Advani studied gate effectiveness in one-dimensional flow and used the results to derive guidelines for the gate effectiveness in higher-dimensional flows [71]. They investigated the effectiveness of the gate in Mold III through a statistical study by varying the vertical location of the gate and the flow front location separately.

7.7 Passive control

In passive control, instead of steering the resin towards the nominal vent locations, additional vents are placed into the mold at locations where resin is likely to arrive last. Depending on the racetracking situation, last-filled regions may take place at various locations of the mold cavity, which may require an impractical number of vents. Therefore, it is necessary to determine which regions of the mold cavity are more likely to receive resin last and place vents at these locations only. Hence, the racetracking conditions and their probability must firstly be predicted.

Although racetracking conditions are not repeatable, they depend on various parameters such as preform cutting/placement tolerances and variations in manufacturing conditions. Figure 7.21 in section 7.5.2 displays the racetracking measurements from 50 experiments. Assuming the manufacturing conditions are stable and sufficient number of experiments are conducted, the distribution of ρ values in the figure can be used as a racetracking forecast for future experiments. Note that racetracking sets and scenario spaces were created in sections 7.5.2 and 7.6.2. Below, a more general and comprehensive approach to globally model racetracking conditions in the mold cavity is presented [44] and each step is illustrated on the simplified version of a window pane mold, which will be used in a case study in section 7.7.4.

- Possible racetracking channels in the mold cavity are identified. Figure 7.25 shows the potential racetracking channels in the window pane mold.

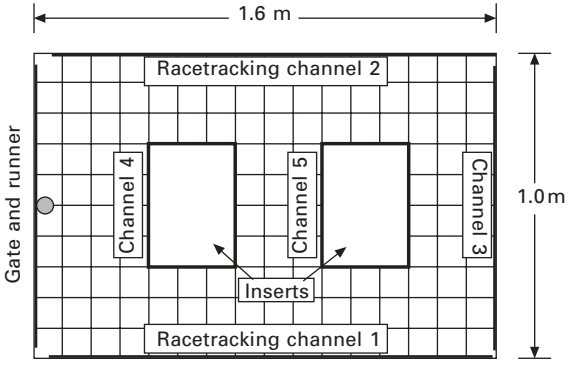

7.25 Potential racetracking channels in the window pane mold geometry.

- While the racetracking strength in a channel (ρ) is ultimately unpredictable during an experiment, it is possible to develop a probabilistic measure such as, 'On a selected side of the mold, it is 20% likely that there will be negligible racetracking, 50% likely that there will be low racetracking,

20% likely that there will be medium racetracking and 10% likely that there will be strong racetracking'. Density functions from the probability theory are utilized as probabilistic measures of the racetracking conditions in the channels. The probability that the racetracking strength in a channel will occur within a certain range, $\rho_1 \geq \rho \geq \rho_2$, can be estimated from a density function. The density function that characterizes racetracking behavior in a racetracking channel is called as the *racetracking forecast*. The ideal way to obtain the density function is to use process statistics from the manufacturing floor. The tolerances of preform cutting and the equipment used to place the fabrics in the mold, plus the experience of the operators, will also influence the density function. Density functions can be derived only under steady manufacturing conditions, and the degree of agreement between the density function and the actual racetracking conditions in the mold will influence the efficiency of the optimized results on the manufacturing floor. Variations of Weibull density function (Fig. 7.26a) are used to model racetracking conditions in the window pane mold.

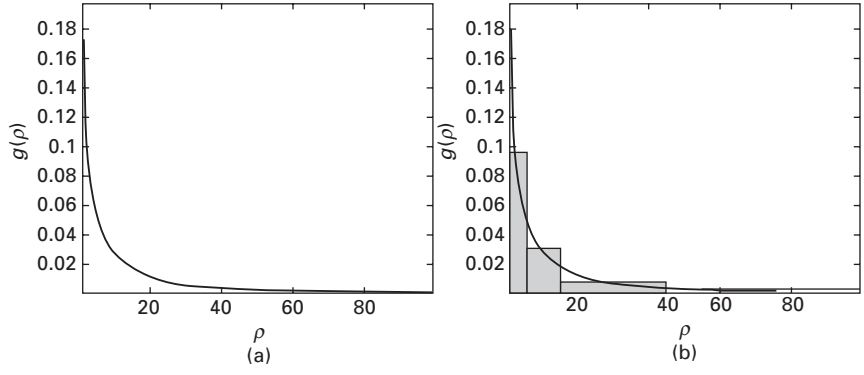

7.26 (a) Weibull probability density function. (b) Continuous probability density function is discretized into a racetracking set with five racetracking values.

- The density functions are usually continuous. Since a continuous function is not usable in optimization studies, it is discretized into a racetracking set, $\mathscr{R}_i = \{\rho_1, \ldots, \rho_m\}$, where i is the index of the racetracking channel and m is the number of elements in the racetracking set. Each element in the racetracking set represents a ρ interval from the ρ range. A probability value is calculated for each element in $\mathscr{R}$ from the density function. The likelihood that an actual racetracking value will be in a certain ρ interval is given by the probability value of the $\mathscr{R}$ element which represents that interval. The sum of the probability values is equal to 1. All five density

functions used for the window pane mold are discretized into four ρ values as shown in Table 7.2 and corresponding probability values are estimated from the Weibull density function (Fig. 7.26b).

Table 7.2 Racetracking sets of the channels in the window pane mold and associated probability values

	Racetracking set	Associated probability values
Channel 1	$\mathscr{C}_1$ = {1, 10, 30, 100}	P_1 = {0.44, 0.31, 0.20, 0.05}
Channel 2	$\mathscr{C}_2$ = {1, 10, 30, 100}	P_2 = {0.44, 0.31, 0.20, 0.05}
Channel 3	$\mathscr{C}_3$ = {1, 10, 25, 80}	P_3 = {0.39, 0.35, 0.19, 0.07}
Channel 4	$\mathscr{C}_4$ = {1, 10, 25, 80}	P_4 = {0.39, 0.35, 0.19, 0.07}
Channel 5	$\mathscr{C}_5$ = {1, 10, 25, 80}	P_5 = {0.39, 0.35, 0.19, 0.07}

- After all channels are modeled with appropriate racetracking sets, a scenario space S is created by taking all possible racetracking arrangements: $\mathscr{C}_1 \times \mathscr{C}_2 \times \ldots \times \mathscr{C}_n$, where $\times$ is the Cartesian product[4] operator and n is the number of racetracking channels in the mold. Each scenario represents a process window that may take place during the actual mold filling process and has a certain probability of occurrence. Assuming the racetracking forecast of each channel is independent of the other racetracking channels, the probability of each scenario is estimated by multiplying the probability values of the racetracking set elements that make up the scenario. The probability of a scenario determines its weight in the scenario space, which has a total probability of 1. With the addition of the probability dimension, the scenario space represents mold filling conditions, including preform cutting and placement operations. Practically, it predicts what might happen during mold filling on the manufacturing floor. Note that scenario space is an approximation to the racetracking forecast. As for the window pane mold, the scenario space is created by taking the Cartesian product of the racetracking sets, $\mathscr{C}_1 \times \mathscr{C}_2 \times \mathscr{C}_3 \times \mathscr{C}_4 \times \mathscr{C}_5$, which yields 1024 scenarios. The runner location on the left edge was known beforehand, which simplified the racetracking modeling. Otherwise, the scenario space is independent of the gate locations and injection conditions.

7.7.1 Optimization problem

The locations of the vents do not have an effect on the mold filling process until resin arrival. *Assuming they are closed shortly after resin arrivals*, vent

[4] The Cartesian product in set theory resembles *outer multiplication operation* in *tensor notation*, except that the operands are not actually multiplied in the Cartesian product but are grouped together.

locations act as a constraint on the mold filling process, rather than a process variable.

> **Constraint I.** At any given time during mold filling $t = t_i$, each contiguous air bubble in the mold cavity must have at least one vent within its volume; $p(\mathscr{V}) : \mathscr{D}_i \cap \mathscr{V} \neq 0$, where p is the constraint, $\mathscr{D}_i$ is the set of nodes in the contiguous air bubble i and $\mathscr{V}$ is the vent configuration. A vent configuration is defined as the set of all nodes that possess a vent.

When an air bubble is no longer connected with any vent ($\mathscr{D}_i \cap \mathscr{V} = 0$) then Constraint I is violated and a dry spot forms[5]. Therefore, given the racetracking forecast, the vents should be placed optimally in the mold to minimize the likelihood of dry spot formation. Consequently, the optimization problem can be stated as follows:

> **Problem statement:** Given a racetracking forecast (approximated by scenario space S), a non-empty, closed set $\mathscr{A} \subset R$ {: integer} and a function[6] $f : \mathscr{A}^n \rightarrow R$, find at least one vent configuration $\mathscr{V}^* \in \mathscr{A}^n$ satisfying $f(\mathscr{V}^*) \geq f(\mathscr{V})$ for all $\mathscr{V} \subset \mathscr{A}^n$, where n is the number of vents and $\mathscr{A}^n = \mathscr{A} \times \ldots \times \mathscr{A}$ (n times Cartesian product).

In LCM, $\mathscr{A}$ is the set of nodes in the finite element mesh of the mold where a vent can be placed. Function f is the *performance index* (cost function) that needs to be maximized. The performance index is chosen as the *mold filling success rate*, which is defined as the cumulative probability of the scenarios that are successfully drained by a given vent configuration $\mathscr{V}$:

$$\text{Performance index of } \mathscr{V}: f(\mathscr{V}) = P(\mathscr{B} = \{ \text{ scenarios drained by } \mathscr{V}\}) \qquad 7.9$$

where event $\mathscr{B}$ is a subset of scenario space $\mathscr{S}$. For example, in a given problem with a certain racetracking forecast, if scenarios ξ_2, ξ_7 and ξ_{19} are drained successfully by vent configuration $\mathscr{V}_1$, then $\mathscr{B} = \{\xi_2, \xi_7, \xi_{19}\}$ and $f(\mathscr{V}_1) = P(\xi_2 + (P(\xi_2) + P(\xi_7) + P(\xi_{19})$ according to eqn 7.9. Note that function p in Constraint I is integrated into f in the optimization problem statement above. Since an analytical expression for f is not available, mold filling simulation output from LIMS is used to estimate the value of $f(\mathscr{V})$.

[5] In this chapter, as soon as a dry spot forms, it is recorded and the dynamics of the air bubble motion in the closed mold are ignored.

[6] f maps elements of domain $\mathscr{A}^n$ to real numbers R.

7.7.2 Last-filled region and vent fitness maps

There is a close relationship between the last-filled regions and the optimal vent locations in the mold. Once the scenario space has been created and the injection system designed, the mold filling is simulated for the entire scenario space. In the window pane mold, the resin is injected through a gate and number on the left edge. Mold filling was simulated for 1024 scenarios in the scenario space. Figure 7.27 illustrates the flow patterns and the last-filled regions from six randomly selected scenarios. The racetracking values (ρ) of the channels in each scenario are shown below the flow pattern: the first value belongs to channel 1, the second value belongs to channel 2, etc. Next the last-filled regions from all scenarios are superimposed – taking scenario probabilities into account – to determine where last-filled regions concentrate over the mold geometry. The distribution of the last-filled regions over the window pane mold is illustrated in Fig. 728(a), which is called a *last-filled region map*. The resin is more likely to arrive at darker mold regions in the figure.

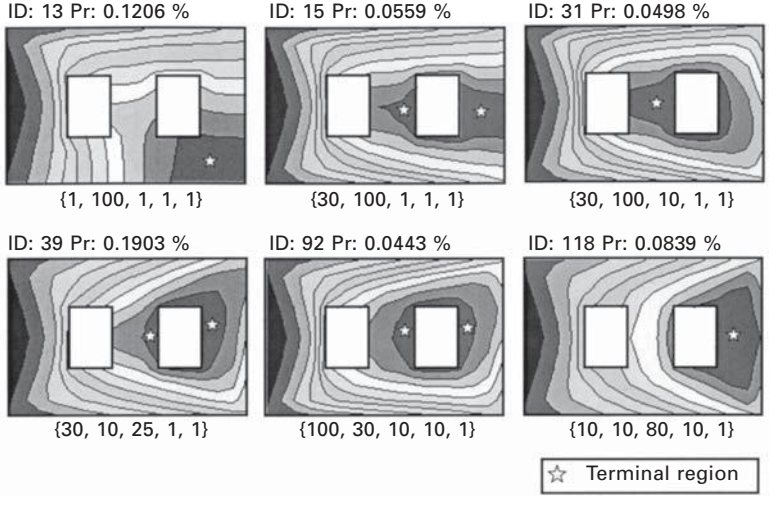

7.27 The flow patterns of six sample scenarios from the scenario space of the window pane mold. The resin runner lies along the left edge. ID is the index of the scenario in the scenario space and Pr is the (percentage) probability of the scenario. Five values under the figures show the racetracking strengths along the five channels in the mold for the given scenario.

Ideally, a *successful mold filling* implies that there are no unfilled nodes remaining when the resin arrives at the last vent. However, this is a very restrictive definition for the optimization problem under study, because it will be a challenge to find a feasibly small vent configuration with a significant

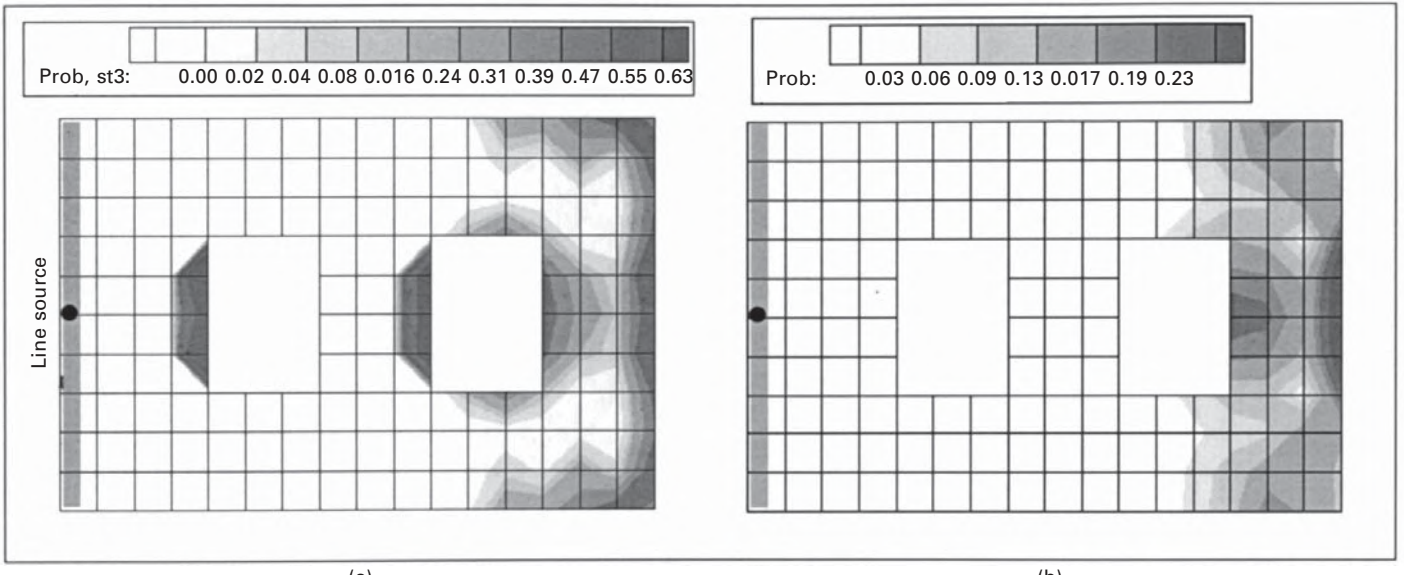

7.28 (a) Last-filled region distribution in window pane mold. (b) Corresponding vent distribution plot that shows the merit of nodes to become vent locations.

performance index. In order to relax this requirement, two tolerances are introduced, based on the process physics: (i) dry spots that include fewer nodes than a preset value at the time of formation are ignored, and (ii) in order to drain air bubbles in the vicinity of a vent, a certain amount of resin is allowed to bleed after it arrives at the vent. The first tolerance is quantified in terms of nodes in a dry spot and the second tolerance is represented as a dry spot-proof region of certain radius around a vent. Any mold filling simulation that satisfies both tolerances will be considered as *successfully drained* (or *successfully filled*).

Owing to the introduction of the tolerances, a single scenario can be successfully drained by several vent configurations. Figure 7.29 illustrates the mold filling contour plot for a certain scenario of a rectangular mold. A single gate at the center of the mold creates two last filled regions on the right and left sides of the mold. The air on the right side can be successfully drained by a single vent at any of the nodes {265, 276, 277}. The air on the left side can be drained by a single vent at any of the nodes {5, 6, 16, 17}. Hence, nodes {5, 6, 16, 17, 265, 276, 277} are possible vent configurations in this scenario of the rectangular mold. Each scenario will give a different set of nodes as the vent locations. A node may appear in many scenarios as a possible vent location. The cumulative probability of the scenarios it appears in as a possible vent location, gives the fitness of that node to be a vent. For the window pane mold, the dry spot tolerance is taken as four nodes and the radius of the dry spot-free area around a vent is taken as the distance nodes between two. The vents are found for all scenarios and the fitness of the nodes to be vents are estimated and plotted in Fig. 7.28(b). The two contour plots in Fig. 7.28 are different, yet display similar morphological properties. The reason for the difference between the plots is the introduction of the dry spot tolerances. For example, Fig. 7.28(a) shows that dry spots are frequently

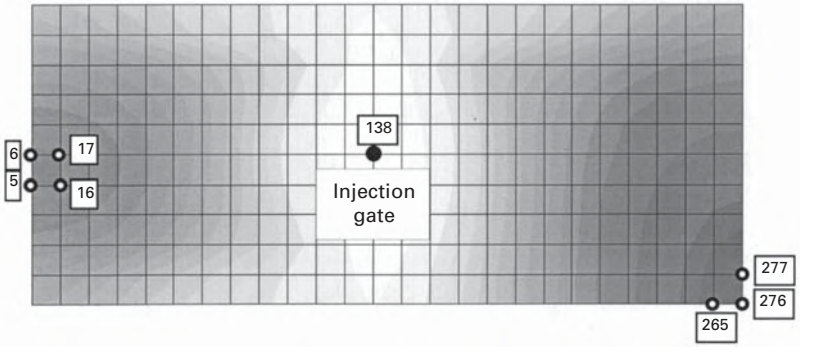

7.29 Nodes that can drain air successfully on the right and left sides of the mold. Contour plot shows the flow front locations at several time steps.

captured to the left of the two inserts in the mold. However, Fig. 7.28(b) does not suggest any vent in those two regions, because the sizes of the dry spots are smaller than the dry spot tolerance. The vent distribution plot shows the merit of nodes becoming vents, hence it can be used as an elementary vent optimization tool.

Although vent distribution plots display the merit of nodes becoming vent locations, they are not sufficient to choose optimal vent locations, as they exclude an important pieces of information: (i) each scenario is independent of other scenarios and (ii) each scenario requires all necessary vents. Even if a single required vent is missing, a scenario will not be drained successfully. For example, for the scenario in Fig. 7.29, the possible vent locations are {5, 6, 16, 17, 265, 276, 277}. However, it must be stated that there must be at least two vents in the mold to drain this scenario: one vent from set {265, 276, 277} and one vent from set {5, 6, 16, 17}. If either vent is missing, the mold filling will not be successful in the process window represented by this scenario. Vent distribution plots indicate the merit of individual nodes to be vents, but exclude the fact that certain nodes should act together in a vent configuration to be useful. Hence, a combinatorial search algorithm that works on a scenario basis is developed in the following section.

7.7.3 Combinatorial search (CS)

It has been shown by Gokce and Advani [44] that a vent configuration that is created by merging two or more vent configurations includes all the scenarios from the individual vent configurations. Thus, in combinatorial search, superior small vent configurations are found first and the optimal vent configuration is sought by merging the small vent configurations as explained below:

- *Step I*. For each scenario, the vent configurations with the smallest number of vents that save the scenario are found. Note that a scenario is saved by several vent configurations owing to the dry spot tolerances. These small vent configurations are called the *elementary vent configurations* (EVC) and are used as the building blocks of large vent configurations (i.e. vent configurations with a large number of vents) during the optimization procedure. The collection of all EVCs is called the EVC set E .
- *Step II*. The data from the previous step are rearranged to find the scenarios saved by each EVC. The cumulative probability of the scenarios saved by an EVC gives its success rate (performance index).
- *Step III*. EVCs with low success rates are eliminated from set ε. The remaining EVCs are grouped with respect to the number of vents they include. ${}^{i}\varepsilon$ is used to represent the group of elementary vent configurations with i vents.
- *Step IV*. Note that there is a constraint on the number of vents, n. There are

various ways to combine elementary vent configurations from ε that satisfy this constraint. For example, if four vents are allowed in a mold and the set ε has vent configurations with one, two or three vents ($\varepsilon = {}^1\varepsilon \cup {}^2\varepsilon \cup {}^3\varepsilon$), then all vent configurations that include four vents can be created as follows:

$$ {}^4\mathscr{W} = \{{}^1\varepsilon \times {}^1\varepsilon \times {}^1\varepsilon \times {}^1\varepsilon\} \cup |{}^1\varepsilon \times {}^1\varepsilon \times {}^2\varepsilon\} \cup \{{}^2\varepsilon \times {}^2\varepsilon\} \cup \{{}^1\varepsilon \times {}^3\varepsilon\} \qquad 7.10 $$

- *Step V*. Instead of creating ${}^4\mathscr{W}$ at once, one may use the following incremental procedure, which is based on the underlying theory of the combinatorial search:

$$ i = 1: \quad {}^1\mathscr{W} = {}^1\varepsilon $$

$$ i = 2: \quad {}^2\mathscr{W} = \{{}^1\mathscr{W} \times {}^1\varepsilon\} \cup \{{}^2\varepsilon\} $$

$$ i = 3: \quad {}^3\mathscr{W} = \{{}^2\mathscr{W} \times {}^1\varepsilon\} \cup \{{}^1\mathscr{W} \times {}^2\varepsilon\} \cup \{{}^3\varepsilon\} $$

$$ i = n = 4: \quad {}^4\mathscr{W} = \{{}^3\mathscr{W} \times {}^1\varepsilon\} \cup |{}^2\mathscr{W} \times {}^2\varepsilon\} \cup \{{}^1\mathscr{W} \times {}^3\varepsilon\} $$

At each step during the procedure, only superior vent configurations with high-performance indices (success rate) in ${}^i\mathscr{W}$ are retained for the next step, reducing the computational cost significantly. In, this way, it is possible to introduce *minimum required performance* as a second optimization stop criterion, which will yield fewer vents with suffcient performance. Note that optimal vent configurations that include one, two or three vents are also determined as a by-product of the procedure above.

7.7.4 Case study: the window pane mold

The combinatorial search is demonstrated on the window pane, a 1.6×1.0 m^2 rectangular mold containing two inserts (Fig. 7.25). The mesh of the geometry includes 175 nodes, 136 2D elements (quads) and 80 1D elements (bars). 1D elements are used to model racetracking channels. Top, bottom and right edges, and the perimeters of the inserts are identified as five racetracking channels. The racetracking conditions in each channel are forecast using variations of the Weibull density function. The racetracking sets and associated probability values are shown in Table 7.2. A scenario space with 1024 scenarios is created to model the racetracking condition in the mold. The injection scheme is specified as constant flow rate through node 70 (x = 0, y = 0.5 m) on the left edge, which is connected to a runner along the left edge. The last-filled region map is illustrated in Fig. 7.28(a).

The number of vents is selected as four. Dry spots with three or fewer nodes are tolerated and an area of 2-node radius around a vent is considered dry spot-proof. Set ε is generated with 465 EVCs, which include one or two

vents, i.e. $\varepsilon = {}^1\varepsilon \cup {}^2\varepsilon$. Using the incremental procedure at step V above, the optimal vent configurations with one, two, three and four vents are found consecutively. The optimal vent configurations are also investigated using an exhaustive search. A vent candidate pool $\mathscr{P}$ is created from the nodes that appeared in a last filled region, at least in one scenario. Vent configurations are created by taking Cartesian products of $\mathscr{P}$. When the computational cost becomes prohibitive for large vent configurations, the candidate pool is sampled evenly (geometrically) to reduce the pool size. The ES conducted using a downsized candidate pool is called *partial exhaustive search* (partial ES). While ES provides the optimum solution, a partial ES may not provide the optimum solution, but will indicate near-optimal solutions. The results of CS and ES are compared for accuracy and efficiency. The computational cost is reported in terms of the duration of the optimization process. Gateway 2000 computers with Pentium 4 1600 MHz processors and 256MB RAM were used for this study. The results for CS and (partial) ES are listed in Table 7.3. The results for the 3-vent and 4-vent cases are illustrated in Fig. 7.30. In each case, all nodes that appeared as vent locations are shown on the figure. The performance index of the CS result is shown with a pie chart on each figure. The computational cost comparison between the CS and ES (or partial ES) is illustrated with a bar plot. CS results are as accurate as ES results and better than partial ES results. Computational savings are 57%, 91%, 99% and 97% for 1-vent, 2-vent, 3-vent and 4-vent optimization, respectively.

Table 7.3 CS and ES optimization results for window pane mold. Performance index is the cumulative probability of the scenarios that are drained by $\mathscr{V}^*$

Optimization method	Optimal vent configuration[a], $\mathscr{V}^*$ (node numbers)	Performance index, $f(\mathscr{V}^*)$	Computational cost (s)
Creation of set ε	–	–	69
CS	118	27.6%	69
ES	118	27.6%	162
CS	107 117	48.2%	209
ES	107 117	48.2%	2,439
CS	57 107 117	69.0%	301
ES	57 107 117	69.0%	44,570
CS	57 106 118 168	87.9%	1,364
Partial ES	57 107 117 169	87.3%	51,165

[a] *x* and *y* coordinates of the nodes are as follows (in m): 57 (1.4, 0.0), 106 (1.3, 0.5), 107 (1.3, 0.6), 117 (1.6, 0.4), 118 (1.6, 0.5), 168 (1.4, 0.9), 169 (1.4, 1.0).

As a benchmark, an intuitive vent design, illustrated in Fig. 7.31, was tested in the scenario space. The success rate was only 28% as compared to 69% with the optimal 3-vent vent configuration.

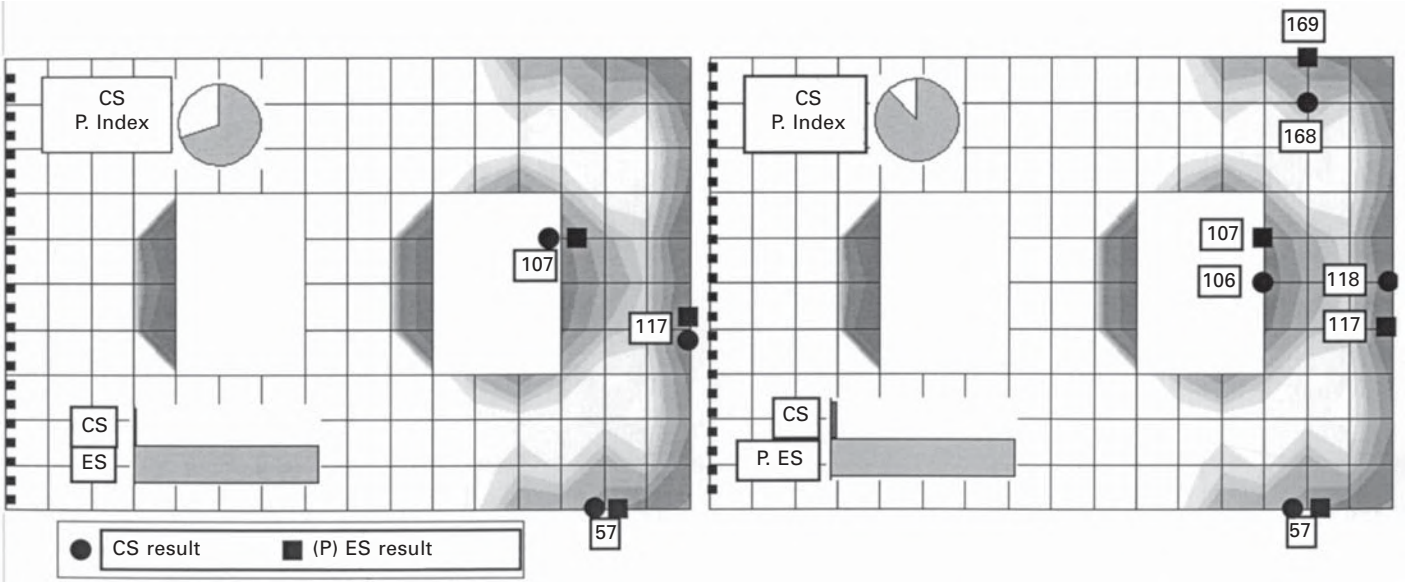

7.30 Optimal 3-vent (*left*) and 4-vent (*right*) vent configurations in the window pane mold as found by combinatorial search (CS) and exhaustive search (ES). Since each optimization method returned different results, vent locations are shown by different markers, as illustrated in the legend.

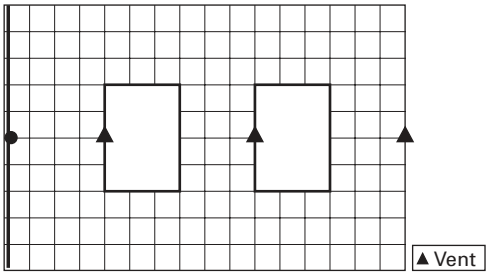

7.31 The vent configuration used as a benchmark to evaluate the performance of the optimization algorithm Combinatorial Search.

Mold symmetry and scenario space

The window pane mold has many symmetric features: the geometry, injection conditions, density function and the racetracking sets of symmetric channels. Consequently, last-filled region and vent fitness maps are also symmetric. Therefore:

- Two vent configurations that are symmetries of each other will yield the same results.
- It is erroneous to investigate a section of the geometry only, since several scenarios in the scenario space are not symmetric owing to different racetracking conditions along the symmetric channels. Yet, several scenarios are symmetric with respect to each other. Two scenarios are called *symmetric* if the resin flow pattern of one is a symmetry of the flow pattern in the other across an axis. The size of the scenario space can be reduced by eliminating one of the symmetric scenario groups. Later, the optimal vent configuration for the reduced scenario space can be mirrored across symmetry axes to create the optimal vent configuration for the entire scenario space.

7.8 Conclusion

Resin flow through textile preforms in the mold cavity was modeled in section 7.2 using Darcy's law. Liquid injection molding simulation (LIMS), which was used to simulate resin flow in the mold cavity, was introduced in section 7.3. Its features and utilization in design, optimization and control studies were presented. The branch and bound search was adapted to gate location optimization in section 7.4 and its application was demonstrated with a case study. Section 7.5 introduced the disturbances associated with the mold filling process. Racetracking was identified as the key disturbance and it was shown with a case study that it is not repeatable. Active and passive control methods that enable successful mold filling in the presence

of racetracking were proposed in sections 7.6 and 7.7, respectively. In active control, which was exemplified by simulation-based liquid injection control (SLIC), the resin flow is redirected by varying the injection conditions at the injection gates. In passive control, racetracking conditions were modeled probabilistically and a sufficient number of vents are placed at locations where resin is more likely to arrive last. The approaches and procedures to create these strategies were presented with pedagogic examples.

7.9 Outlook

The knowledge base about LCM processes is growing every day. Several tools and methodologies that address modeling, design, optimization and control issues are available or under development. Ultimately, the aim is to develop the LCM technology to the extent that simple, high-volume parts will be manufactured quickly, and large, complex and low volume parts will be manufactured successfully. A maximum level of automation is desirable, especially for the former group. Since automation makes the manufacturing steps repeatable, the average quality of the parts will increase. Automation also cuts down the labor costs and decreases the health hazards by decreasing the exposure of the workers to the resin fumes and preform soot. Reducing the reject rate is a prime goal in all cases.

Further research and development is necessary to bring LCM processes to their full potential. The work presented in this chapter spans several important issues in mold filling. Some of the future research directions are presented below.

7.9.1 Multiple gate optimization

This topic is rarely addressed by the researchers, possibly because of the extensive computational effort required. There is a permutational relationship between the number of the gates and the problem size: in a mold with N nodes, there are N possibilities for the first gate, $N(N-1)$ possibilities for the second gate, etc. An optimally designed multi-injection system can reduce the fill time significantly and hence the need to explore optimization methods that can address this issue effectively.

7.9.2 Optimal placement of flow enhancement media

In LCM processes such as VARTM (or vacuum infusion), a flow enhancement medium is placed on the entire surface of the preform to distribute the resin quickly. However, this method is not applicable when there are mold regions that are inaccessible for the flow enhancement medium or the vacuum line as shown in Fig. 7.32. Also, if the mold geometry is complex and includes

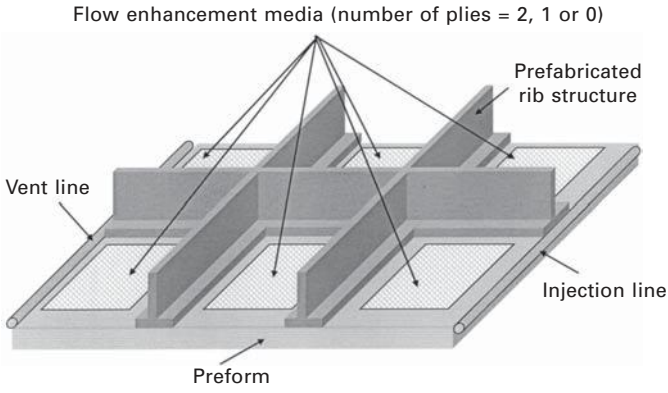

7.32 A composite part geometry that does not allow the placement of flow enhancement media over the entire geometry.

inserts or ribs, such a design may fail to fill the mold successfully. Therefore, the flow enhancement medium needs to be designed optimally in these cases in order to increase the efficiency of the mold filling operation.

7.9.3 Use of manufacturing data for racetracking forecast

In section 7.7, a generic density function was used to forecast racetracking in the racetracking channels for illustration purposes. In actual applications, the racetracking forecast must capture the manufacturing conditions, which are assumed to be stable. Statistics from the manufacturing floor and equipment, material and processing tolerances must be incorporated into the racetracking forecast. Even if it is not possible to capture the actual case exactly, a sufficiently accurate racetracking forecast will be very useful to test various designs in the simulation environment.

7.9.4 Feasible target flow pattern selection in set point-based active control

Set point-based feedback controllers generate control inputs based on the tracking error between the target flow pattern and the actual flow pattern. A flow pattern strongly depends on the permeability field in the mold cavity. Given a permeability field and a gate configuration, there is a finite range of flow patterns that can be created by modifying the injection conditions at the gates, which is called the *reachable set*. For a controller to be successful in minimizing the tracking error, the target flow pattern must belong to this set. Therefore, it is crucial to predict the reachable set in the presence of disturbances

and select a feasible target flow pattern. Multiple target flow patterns can be selected as needed depending on the racetracking forecast.

7.10 Acknowledgements

The financial support, provided by the Office of Naval Research (ONR) under Grant N000l4-97-C-0415 for the Advanced Materials Intelligent Processing Center at the University of Delaware, made the work presented in this chapter possible. The invaluable contributions of Dr Pavel Simacek, Dr Kuang-Ting Hsiao and Mathieu Devillard to this chapter are kindly appreciated.

7.11 References

1. Advani S.G. and Sozer M.E., *Process Modeling in Composites Manufacturing*. Marcel Dekker, New York, 2003.
2. Advani S.G., Resin transfer molding in *Flow and Rheology in Polymeric Composites Manufacturing*, pages 465–516. Elsevier Publishers, Amsterdam, 1994.
3. Rosato D.V. and Lee (ed.) S.M., Polymeric Matrix Composites in *International Encyclopedia of Composites*, volume 3, pages 148–181. VCH Publishers, Inc., New York, 1990.
4. Schwartz M.M., *Composite Materials Handbook*. McGraw Hill, New York, 1992.
5. Gokce A., Modeling of flow continuum and optimal design of control-oriented injection systems in liquid composite molding processes. PhD thesis, University of Delaware, 2003.
6. Bickerton S., Modeling and control of flow during impregnation of heterogeneous porous media, with application to composite mold filling processes. PhD thesis, University of Delaware, Spring 1999.
7. Stadtfeld H.C., Experimental validation of impregnation schemes with control strategies in liquid composite molding processes. Master's thesis, University of Delaware, 2000.
8. Kueh S.R.M., Fiber optic flow monitoring system and methodology for sensor placement to identify flow disturbances in liquid composite molding. PhD thesis, University of Delaware, Summer 2001.
9. Kozeny J., *Sitzungsberichte Abt IIa*. Wiener Akademie der Wissenschaft, 1927.
10. Carman P.C., *Fluid Flow Through Granular Beds*. Transactions 15, Institution of Chemical Engineers, 150–166, 1937.
11. Dave R., Kardos J.L. and Duducovic M.P., A model for resin flow during composite processing. part 2: Numerical analysis for unidirectional graphite/epoxy laminates. *Polymer Composites*, 8(2), 1987.
12. Lam R.C. and Kardos J.L., The permeability and compressibility of aligned and cross-plied carbon fiber beds during processing of composites. In *Proceedings of ANTEC, SPE*, New York, May 1989.
13. Bruschke M.V., A predictive model for permeability and non-isothermal flow of viscous and shear-thinning fluids in anisotropic fibrous media. PhD thesis, University of Delaware, 1992.
14. Chiemlewski C., Petty C.A. and Jeyaraman K., Crossflow permeation of viscous and viscoelastic liquids in cylinder arrays. In *Proceedings of the American Society for Composites Fifth Technical Conference*, East Lansing, June 1990.

15. Simacek P. and Advani S.G., Permeability model for woven fabrics. *Polymer Composites*, 17(6): 887–899, December 1996.
16. Chang W. and Kikuchi N., Analysis of non-isothermal mold filling process in resin transfer molding (RTM) and structural reaction injection molding (SRIM). *Computational Mechanics*, 16(1): 22–35, 1995.
17. Lee C.K., Sun C.C. and Mei C.C., Computation of permeability and dispersivities of solute or heat in periodic porous media. *International Journal of Heat and Mass Transfer*, 39(4): 661–676, 1996.
18. Dimitrovova Z. and Faria L., Finite element modeling of the resin transfer molding process based on homogenization techniques. *Computers and Structures*, 76(1): 379–397, 2000.
19. Koponen A., Kataja M. and Timonen J., Statistical physics, plasmas, fluids, and related interdisciplinary topics. *Physical Review E*, 56(3): 3319–3320, 1997.
20. Spaid M. and Phelan F., Modeling void formation dynamics in fibrous porous media with the lattice boltzman method. *Composites Part A*, 29 (7): 749–755, 1998.
21. Gokce A. and Advani S.G., Permeability estimation with the method of cells. *Journal of Composite Materials*, 35(8): 713–728, 2001.
22. Nedanov P., Permeability characterization of fibrous porous media. Master's thesis, University of Delaware, 2002.
23. Gebart B.R., Permeability of unidirectional reinforcements for RTM. *Journal of Composite Materials*, 26(8): 1100–1133, 1992.
24. Verheus A.S. and Peeters J.H., A. The role of reinforcement permeability in resin transfer molding. *Composites Manufacturing*, 4(1): 33–38, 1993.
25. Parnas R.S. and Salem A.J. A comparison of the unidirectional and radial in-plane flow of fluids through woven composite reinforcements. *Polymer Composites*, 14(5): 383–394, 1993.
26. Ferland P., Guittard D. and Trochu F., Concurrent methods for permeability measurement in resin transfer molding. *Polymer Composites*, 17(1):149–158, 1996.
27. Wang J.T., Wu C.H. and Lee L.J., In-plane permeability measurement and analysis in liquid composite molding. *Polymer Composites*, 15(4): 278–288, 1994.
28. Weitzenbock J.R., Shenoi R. A. and Wilson P.A., Measurement of three-dimensional permeability. *Composites Part A*, 29(1–2): 159–169, 1998.
29. Bruschke M.V. and Advani S.G., A finite element/control volume approach to mold filling in anisotropic porous media. *Polymer Composites*, 11: 398–405, 1990.
30. Bruschke M.V. and Advani S.G., A numerical approach to model non-isothermal viscous flow through fibrous media with free surfaces. *International Journal for Numerical Methods in Fluids*, 19: 575–603, 1994.
31. Lee L.J., Young W.B. and Lin R.J., Mold filling and cure modeling of RTM and SRIM processes. *Composite Structures*, 27(1–2): 109–120, 1994.
32. Tredoux L. and Westhuizen J., Van der. Development of a numerical code that simulates combined heat transfer, resin flow and compaction during composite processing. *Composites Manufacturing*, 6(2): 85–92, 1995.
33. Fracchia C.A., Castro J. and Tucker III C.L., A finite element/control volume simulation of resin transfer molding. In *Proceedings of the ASC 4th Annual Technical Conference*, Santa Monica, October 1995.
34. Young W.-B., Consolidation and cure simulation for laminated composites. *Polymer Composites*, 17(1): 142–148, 1996.
35. Liu X.-L., Isothermal flow simulation of liquid composite molding. *Composites Part A: Applied Science and Manufacturing*, 31(12): 1295–1302, Dec 2000.

36. Simacek P., Sozer E.M. and Advani S.G., *User Manual for DRAPE 1.1 and LIMS 4.0 Liquid Injection Molding Simulation, Technical Report UD-CCM 98-01*. Center for Composite Materials, University of Delaware, Newark, DE, 1998.
37. The Mathworks, Inc., http://www.mathworks.com. *Learning MATLAB*.
38. Mathur R., Advani S.G. and Fink B.K., Use of genetic algorithms to optimize gate and vent locations for the resin transfer molding process. *Polymer Composites*, 20: 167–178, 1999.
39. Gokce A., Hsiao K.-T. and Advani S.G., Branch and bound search to optimize injection gate locations in liquid composite molding processes. *Composites: Part A*, 33: 1263–1272, 2002.
40. Papalambros P.Y. and Wilde D.E., *Principles of Optimal Design: Modeling and Computation*. Cambridge University Press, Cambridge, 1988.
41. Rao S.S., *Optimization: Theory and Applications*. Wiley Eastern Limited, New Delhi, 1979.
42. Parker R.G. and Rardin R.L., *Discrete Optimization*. Academic Press Inc., San Diego, 1988.
43. Horst R. and Tuy H., *Global Optimization: Deterministic Approaches*. Springer-Verlag, Berlin, 3rd edition, 1996.
44. Gokce A. and Advani S.G., Combinatorial search to optimize vent locations in the presence of disturbances in liquid composite molding processes. *Materials and Manufacturing Processes*, 18(2): 261–285, 2003.
45. Bickerton S. and Advani S.G., Characterization of corner and edge permeabilities during mold filling in resin transfer molding. In *Proceedings of the ASME AMD-MD Summer Meeting*, volume 56, pages 143–150, Los Angeles, CA, June 1995.
46. Bickerton S. and Advani S.G., Characterization of racetracking in liquid composite molding processes. *Composites Science and Technology*, 59: 2215–2229, 1999.
47. Han K., Wu C.H. and Lee L.J., Characterization and simulation of resin transfer molding – racetracking and dry spot formation. In *Proceedings of Ninth Annual ASM-ESD Advanced Composite Conference,* Michigan, 1993.
48. Leek R., Carpenter G., Donnellan T. and Phelan F., Simulation of edge flow effects in resin transfer molding. In *Proceedings of the 25th International SAMPE Technical Conference*, pages 233–245, Philadelphia, Oct 1993.
49. Ni J., Zhao Y., Lee L.J. and Nakamura S., Analysis of two regional flow in liquid composite molding. *Polymer Composites*, 18(2): 254–269, 1997.
50. Sheard J., Senft V., Mantell S.C. and Vogel J.H., Determination of corner and edge permeability in resin transfer molding. *Polymer Composites*, 19(1): 96–105, 1998.
51. Hammami A., Gauvin R. and Trochu F., Modelling the edge effect in liquid composite molding. *Composites Part A: Applied Science and Manufacturing*, 29(5–6): 603–609, 1998.
52. Bickerton S. and Advani S.G., Characterization of racetracking in liquid composite molding processes. *Composites Science and Technology*, 59: 2215–2229, 1999.
53. Chaneske J., Jayaraman K., Norman D. and Robertson R., Effects of preform architecture on racetracking in liquid molding. In *Proceedings of International SAMPE Symposium and Exhibition*, pages 954–966, Long Beach, CA, May 2000.
54. Tadmor Z. and Costas G.G., *Principles of Polymer Processing*. John Wiley and Sons, New York, 1979.
55. Data compiled and evaluated by Parnas R.S. and Flynn K.M., *NIST Data Base on Reinforcement Permeability Values, Version 1.0*. NIST Std. Ref. Database 63.
56. Devillard M., Hsiao K.-T., Gokce A. and Advani S.G., On-line characterization of

bulk permeability and race-tracking during the filling stage in resin transfer molding process. In *34th International SAMPE Technical Conference*, Baltimore, November 2002.
57. Demirci H.H. and Coulter J.P., Neural network based control of molding processes. *Journal of Materials Processing and Manufacturing Science*, 2: 335–354, 1994.
58. Demirci H.H. and Coulter J.P., Control of flow progression during molding processes. *Journal of Materials Processing and Manufacturing Science*, 3(4): 409–425, 1995.
59. Demirci H.H., Coulter J.P. and Guceri S.I., Numerical and experimental investigation of neural network-based intelligent control of molding processes. *Journal of Manufacturing Science and Engineering, Transactions of the ASME*, 119(1): 88–94, 1997.
60. Berker B., Barooah P., Yoon M.K. and Sun J.Q., Sensor based modeling and control of fluid flow in resin transfer molding. *Journal of Materials Processing and Manufacturing Science*, 7(2): 195–214, 1998.
61. Nielsen D. and Pitchumani R., Real time model-predictive control of preform permeation in liquid composite molding processes. In *Proceedings of the ASME National Heat Conference*, Pittsburgh, August 2000.
62. Sozer E.M., Bickerton S. and Advani S.G., Modeling and control of liquid composite mold filling process. In *Proceedings of Flow Processes in Composite Materials (FPCM)*, Plymouth, UK, pages 109–124, July 1999.
63. Hsiao K.-T., Devillard M. and Advani S.G., Streamlined intelligent rtm processing: From design to automation. In *Proceedings of 47th International SAMPE Symposium and Exhibition*, volume 47, pages 454–465, Long Beach, CA, May 2002.
64. Westphal L.C., *Sourcebook of Control Systems Engineering*. Chapman & Hall, London, 1992.
65. Kazimierz M., Zbigniew N. and Malgorzata P., *Modelling and Optimization of Distributed Parameter Systems*. Chapman & Hall, London, 1996.
66. Tzou H.S. and Bergman L.A., *Dynamics and Control of Distributed Systems*. Cambridge University Press, Cambridge, 1998.
67. Tzafestas S.G., *Distributed Parameter Control Systems*. Pergamon Press, Oxford, 1982.
68. Avdonin S.A. and Ivanov S.A., *The Method of Moments in Controllability Problems, for Distributed Parameter Systems*. Cambridge University Press, Cambridge, 1995.
69. Grinberg A.S., Lototskii V.A. and Shklyar B., Sh. Controllability and observability of dynamic systems. *Automation and Remote Control* (English translation of *Avtomatika i Telemekhanika*), 52(1): 1–16, June 1991.
70. Cao Y., Gunzburger M. and Turner J., Controllability of systems governed by parabolic differential equations. *Journal of Mathematical Analysis and Applications*, 215(1): 174–189, Nov. 1997.
71. Gokce A. and Advani S.G., Gate effectiveness in controlling resin advance in liquid composite molding processes. *Journal of Manufacturing Science and Engineering*, 125(3): 548–555, 2003.

8

Mechanical properties of textile composites

I A JONES, University of Nottingham, UK and
A K PICKETT, Cranfield University, UK

8.1 Introduction

Textile composites are used typically because of their high strength-to-weight and stiffness-to-weight ratios. In order to exploit these properties it is essential to have a good understanding of their behaviour under load, beginning with the capability to model their stiffness and later consider their strength via suitable failure criteria. It is normal to assume that composites (especially reinforced thermosets) are linear elastic up to the point of failure, although there is some evidence that even thermoset matrix materials can yield in shear. Moreover, there is now increasing interest not just in the modelling of damage onset but also the degradation in properties of a structure as damage progresses. However, in order to be able to reach that stage, an accurate understanding of the structure's elastic behaviour must be established. Hence this chapter starts with a description of elastic behaviour, from simple approaches based on micromechanics and classical laminate theory to more sophisticated analyses developed specifically for textile composites. This is followed by a description of failure behaviour, with particular emphasis on impact loading.

8.2 Elastic behaviour

The application of elasticity to composite materials (even idealised ones, let alone those with the complex fibre architecture of textile-reinforced composites) is an extremely complex area, and any summary of this field in a few pages needs to be accompanied by some strong notes of caution. The first of these is that the ensuing description is only a flavour of the basic theory, and the reader should have no difficulty in locating a number of texts covering this basic material (and its underlying assumptions and limitations) in more detail. For a more in-depth treatment of some aspects, the reader is referred to the very detailed text by Bogdanovitch and Pastore[1], and is encouraged to review the latest literature in the field, some of which is referenced in the present chapter.

The second note of caution is that there are many variants on the notation and definitions used within the theory, with differences ranging from the superficial (the choice of symbols used to represent the various quantities) to the more fundamental (the use of matrices and contracted notation, cf. tensorial notation; mathematical, cf. engineering definition of shear strains). It is therefore vital to ensure that the correct notation and conventions are used before making use of any formula or computer program. The notation used here is essentially that of of Hull and Clyne[2] and of Jones[3], with some minor variations. A summary of the notation, and a more extended presentation of the material in section 8.2.1 is available in Appendix A of Owen *et al*[4].

8.2.1 Fundamentals: orthotropic solids

In order to understand the behaviour of textile reinforced composites it is necessary first to study the concepts of anisotropic and orthotropic behaviour, and to introduce relevant concepts from laminate analysis. Viewed at a microscopic level, textile composites (irrespective of their fibre architecture) are assembled from bundles of parallel fibres embedded in (and assumed to be rigidly bonded to) a matrix material that is usually polymeric and has a much lower modulus than the fibres, and is usually assumed to be homogeneous and isotropic (i.e. properties constant throughout irrespective of position or orientation). This structure will clearly have stiffness and strength properties which are much greater in the direction of the fibre than in any perpendicular direction. Figure 8.1 shows an idealisation of this structure, where the symmetry of the structure is apparent, and enables us to simplify our treatment of the elastic behaviour from the general case of true anisotropy (material properties different in all directions with no symmetry).

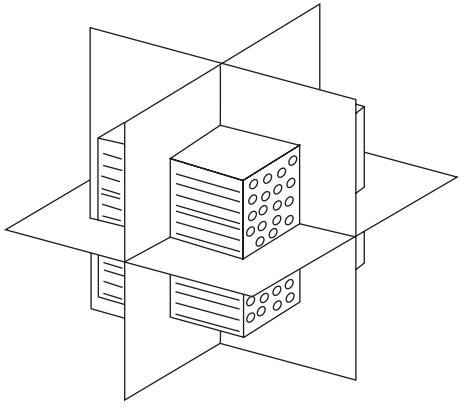

8.1 Schematic diagram of fibre-reinforced composite as an orthotropic solid showing three planes of symmetry.

The elastic behaviour (i.e. the relationship between stresses and strains in the three principal directions) of a material possessing three such planes of symmetry is characterised by the orthotropic constitutive model. This is fully defined by three elastic moduli E_1, E_2 and E_3, three independent Poisson's ratios ν_{12}, ν_{23} and ν_{31} and three shear moduli G_{12}, G_{23} and G_{31}. Three further Poisson's ratios are related to the aforementioned moduli and Poisson's ratios:

$$\nu_{21} = \nu_{12}\frac{E_2}{E_1};\ \nu_{32} = \nu_{23}\frac{E_3}{E_2};\ \nu_{13} = \nu_{31}\frac{E_1}{E_3} \qquad 8.1$$

The elastic behaviour may be expressed via Hooke's law for orthotropic materials:

$$\varepsilon_1 = \frac{1}{E_1}(\sigma_1 - \nu_{12}\sigma_2 - \nu_{13}\sigma_3)$$

$$\varepsilon_2 = \frac{1}{E_2}(\sigma_2 - \nu_{21}\sigma_1 - \nu_{23}\sigma_3)$$

$$\varepsilon_3 = \frac{1}{E_3}(\sigma_3 - \nu_{31}\sigma_1 - \nu_{32}\sigma_2)$$

$$\gamma_{12} = \frac{\tau_{12}}{G_{12}} \quad \gamma_{23} = \frac{\tau_{23}}{G_{23}} \quad \gamma_{13} = \frac{\tau_{13}}{G_{13}} \qquad 8.2$$

This is a generalisation of the isotropic three-dimensional (3D) expression of Hooke's law, one of the first mathematical relationships to which students of solid mechanics are exposed. In practice we are generally interested in a thin layer or lamina of material (or, eventually, an assembly of them); in this case it can usually be assumed that through-thickness stress (defined to be σ_3) is negligible and the through-thickness strain (ε_3) is unimportant. Equation 8.2 can therefore be simplified to express the strains within the 1–2 plane in terms of the stresses in that plane:

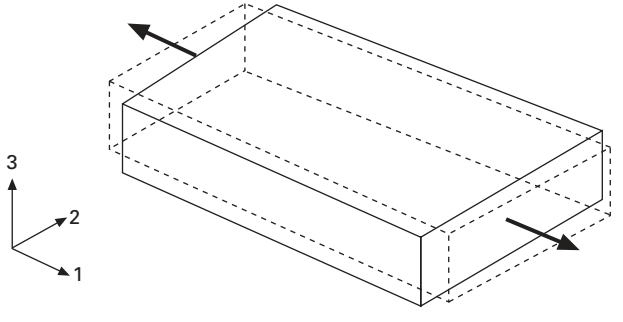

8.2 Orthotropic solid loaded along its axis displays no tension-shear coupling.

$$\varepsilon_1 = \frac{1}{E_1}(\sigma_1 - \nu_{12}\sigma_2)$$

$$\varepsilon_2 = \frac{1}{E_2}(\sigma_2 - \nu_{21}\sigma_1)$$

$$\gamma_{12} = \frac{\tau_{12}}{G_{12}} \qquad 8.3$$

These relationships may be expressed more conveniently in matrix form:

$$\begin{Bmatrix} \varepsilon_1 \\ \varepsilon_2 \\ \gamma_{12} \end{Bmatrix} = \begin{bmatrix} \frac{1}{E_1} & -\frac{\nu_{12}}{E_1} & 0 \\ -\frac{\nu_{21}}{E_2} & \frac{1}{E_2} & 0 \\ 0 & 0 & \frac{1}{\tau_{12}} \end{bmatrix} \begin{Bmatrix} \sigma_1 \\ \sigma_2 \\ \sigma_{12} \end{Bmatrix} = \begin{bmatrix} S_{11} & S_{12} & 0 \\ S_{12} & S_{22} & 0 \\ 0 & 0 & S_{66} \end{bmatrix} \begin{Bmatrix} \sigma_1 \\ \sigma_2 \\ \tau_{12} \end{Bmatrix}$$

or $\{\varepsilon\} = [S]\{\boldsymbol{\sigma}\}$ 8.4

where S_{11}, etc., are elements of the on-axis compliance matrix $[\boldsymbol{S}]$ of a lamina. For elastic behaviour the compliance matrix must be symmetric, so that $\nu_{12}/E_1 = \nu_{21}/E_2$ which follows on from eqn 8.1. Therefore only four independent constants (E_1, E_2, G_{12} and either of the Poisson's ratios) are needed to define the in-plane elastic behaviour of a lamina. Note the presence of the zeros in the matrices in eqn 8.4; these mean that the material does not distort in shear when stretched in the on-axis direction (Fig. 8.2).

This behaviour is a direct consequence of the symmetry noted in Fig. 8.1. Sometimes it is preferable instead to express stresses in terms of strains:

$$\begin{Bmatrix} \sigma_1 \\ \sigma_2 \\ \tau_{12} \end{Bmatrix} = \begin{bmatrix} \frac{E_1}{1-\nu_{12}\nu_{21}} & \frac{\nu_{12}E_2}{1-\nu_{12}\nu_{21}} & 0 \\ \frac{\nu_{21}E_1}{1-\nu_{12}\nu_{21}} & \frac{E_1}{1-\nu_{12}\nu_{21}} & 0 \\ 0 & 0 & G_{12} \end{bmatrix} \begin{Bmatrix} \varepsilon_1 \\ \varepsilon_2 \\ \gamma_{12} \end{Bmatrix} = \begin{bmatrix} Q_{11} & Q_{12} & 0 \\ Q_{12} & Q_{22} & 0 \\ 0 & 0 & Q_{66} \end{bmatrix} \begin{Bmatrix} \varepsilon_1 \\ \varepsilon_2 \\ \gamma_{12} \end{Bmatrix}$$

or $\{\boldsymbol{\sigma}\} = [\boldsymbol{Q}]\{\boldsymbol{\varepsilon}\}$ 8.5

where Q_{11}, etc., are elements of the on-axis 'reduced' (plane stress) stiffness matrix $[\boldsymbol{Q}]$ of the lamina, and $[\boldsymbol{Q}] \equiv [\boldsymbol{S}]^{-1}$. Note that these reduced stiffness terms are *not* equal to the corresponding terms in the 3D stiffness matrix for the material. In section 8.2.3 we shall return to the manipulation of these elastic stiffnesses and compliances, but it is useful at the present stage to consider how values for the above moduli and Poisson's ratios can be obtained.

8.2.2 Obtaining the unidirectional properties: testing and micromechanics

The above analysis assumed the availability of the unidirectional bulk properties of the composite material, and later sections will assume knowledge of the local properties of the impregnated fibre bundles (tows) which (along with the regions of pure resin) constitute textile reinforced composite materials. However, obtaining these properties is problematic. It must be realised that composite materials differ in one vital respect from conventional engineering materials such as metals: they do not generally exist as an entity until the manufacture of the component from which they are made. In other words, they are not (with some exceptions) produced by melting or machining stock material but are created from resin and fibre (or a mixture of the fibre and an uncured resin or thermoplastic matrix) at the time of moulding, and their properties depend heavily upon the manufacturing processing conditions. There are two main approaches: experimental measurement using standard testing procedures, and theoretical prediction from the properties of the constituent materials (fibre and matrix). By far the best way of obtaining material properties for design purposes is to perform tests on statistically large samples of materials. Such testing is time consuming and the resulting properties often constitute closely guarded proprietary data. It is important that such tests are conducted to recognised standards.

Measurement of unidirectional and laminate properties: testing methods

Experimental testing may be applied both to the purely unidirectional material and to the finished laminate. A detailed discussion of testing procedures is inappropriate here; instead, reference is made to the various standards in use which define various methods of obtaining the required properties. In particular, BS2782-10 covers various aspects of testing of reinforced plastics (notably method 1003[5], which covers tensile testing, and 1005[6], which covers flexural testing). Standardised test methods for unidirectional materials are also available (for example, ISO 527-5:1997[7], which covers the testing of unidirectional reinforced plastics). Experimental determination of shear properties is problematic; one widely used method is the Iosipescu test embodied in ASTM standard D5379[8], which involves the testing of small, vee-notched specimens loaded within a special frame that subjects them to pure shear within the gauge region. Shear strength properties are easily obtained from the maximum load measured; elastic properties may be determined via the use of a ±45° strain gauge bonded onto the gauge region of the specimen.

Prediction of unidirectional properties: micromechanics

Instead of physically constructing a unidirectional material or a laminate and performing tests, an alternative approach is to predict the unidirectional behaviour of the composite from the properties of its constituent materials, namely its fibre and matrix. This approach is clearly better than nothing, but has some important limitations:

- The spatial distribution of the fibres within the matrix is unknown.
- Wet-out and interfacial bonding are normally assumed to be perfect but are unlikely to be so in practice (there may, for instance, be dry regions within each tow of fibres).
- While the on-axis elastic behaviour of composites is fibre-dominated and relatively easy to predict, the transverse and shear behaviours result from complex stress distributions within the composite and are much less easy to predict theoretically.

The prediction of composite properties from those of the fibre and matrix is one example of the discipline known as micromechanics, and a number of theoretical and semi-empirical models exist. The simplest is known as the 'rule of mixtures', and probably the most commonly used is a refinement of that method known as the Halpin–Tsai equations, although more sophisticated approaches exist such as the composite cylinder assemblage approach, which can take account of anisotropic properties in the fibres themselves.

Rule of mixtures

The rule-of-mixtures approach[3] is applicable particularly to the determination of the longitudinal modulus of a unidirectional composite and of its major Poisson's ratio; its application to transverse and shear moduli gives less accurate results. In the case of the longitudinal modulus, the assumption is made that the strain along a two-dimensional (3D) block of material (Fig. 8.3) is uniform (the iso-strain assumption explored in more detail in section 8.2.3) and that no transverse stresses are present. For a given value of strain,

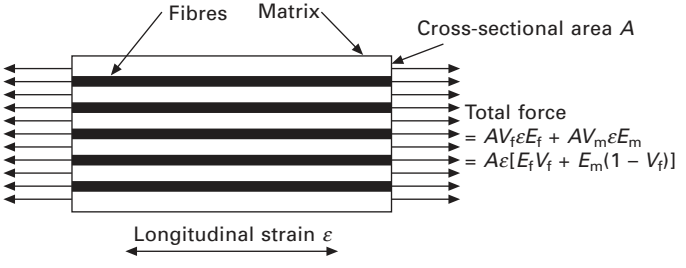

8.3 Rule of mixtures approach to determine longitudinal modulus.

the loads carried by the fibre and matrix components will be proportional both to their moduli and to the cross-sectional area of the fibre and matrix, with the respective areas being proportional to the fibre and matrix volume fractions; in other words, the fibres and matrix are assumed to be elastic bodies (springs) acting in parallel. This leads to the following expression for longitudinal modulus E_1:

$$E_1 = E_f V_f + E_m V_m = E_f V_f + E_m (1 - V_f) \quad 8.6$$

where it is assumed that there is no void content in the composite, and where E_f and E_m are respectively the elastic moduli of the fibre and matrix, and V_f and $V_m \equiv 1 - V_f$ are respectively the volume fractions of the fibre and matrix. A slightly less trivial derivation leads to a very similar expression for the major Poisson's ratio ν_{12} (which in a UD material can be assumed to be identical to ν_{13}):

$$\nu_{12} = \nu_f V_f + \nu_m (1 - V_f) \quad 8.7$$

Both these expressions are found to give answers of good accuracy. By contrast, the application of the rule of mixtures to the transverse elastic properties requires the assumption that the fibres and matrix are elastic bodies in series (requiring the iso-stress assumption, again explained in section 8.2.3); this is very much a simplification since the true arrangement is three-dimensional and is a combination of series and parallel behaviour. The resulting expression for E_2 ($\equiv E_3$) is rather inaccurate but is presented below for completeness:

$$\frac{1}{E_2} = \frac{1}{E_f} V_f + \frac{1}{E_m}(1 - V_f) \quad 8.8$$

Similar arguments apply to the shear moduli (for which both the series and parallel assumptions give poor results), but these will not be pursued further here.

The Halpin–Tsai equations

The Halpin–Tsai equations[9, 10] are effectively a refinement and generalisation of the rule of mixtures. Indeed, for the longitudinal modulus E_1 and major Poisson's ratio ν_{12} the rule of mixtures is used directly via eqns 8.6 and 8.7. The basis of the approach for the transverse and shear moduli is to assume intermediate situations between the extremes of the series and parallel models to which the rule of mixtures is restricted. For these moduli, the form of the equation is as follows:

$$\frac{M}{M_m} = \frac{1 + \xi\eta V_f}{1 - \eta V_f} \quad 8.9a$$

where: $$\eta = \frac{(M_f/M_m) - 1}{(M_f/M_m) + \xi} \quad 8.9b$$

in which:

$M = E_2$, G_{12} and G_{23} for composite
M_f = fibre property E_f or G_f
M_m = matrix property E_m or G_m
V_f = fibre volume fraction
(proportion of composite by volume)

ξ is a constant relating to the way the load is shared between fibre and matrix within the model; its value must lie between the extremes of $\xi = 0$ (in which case eqn 8.9(a) simplifies to the series model similar to eqn 8.8) and $\xi = \infty$ (when eqn 8.9(a) simplifies to the parallel model similar to eqn 8.6). For low fibre volume fractions (up to 65%) ξ may be assumed to be 2 and 1 respectively for the calculation of E_2 (and E_3) and G_{12} (and G_{13}). For higher volume fractions (as may be encountered within densely packed fibre tows), correction factors may be applied. For the calculation of G_{23} a simple value of ξ is insufficient so a formula is required in any case. The three formulae for ξ are therefore[9]:

$$\xi \cong 2 + 40\,V_f^{10} \text{ for calculation of } E_2 \text{ and } E_3$$

$$\xi \cong 1 + 40\,V_f^{10} \text{ for calculation of } G_{12} \text{ and } G_{13}$$

$$\xi \cong \frac{1}{4 - 3\nu_m} \text{ for calculation of } G_{23} \quad 8.10$$

Halpin[10] states that the Poisson's ratio ν_{23} in the transverse plane may be calculated approximately from the relevant direct and shear moduli using the following relationship:

$$\nu_{23} \cong 1 - \frac{E_2}{G_{23}} \quad 8.11$$

Hashin's composite cylinder assemblage model

Although the above formulae are widely quoted and used, no published results have been found that evaluate their accuracy for use with fibres (such as carbon or aramid) whose properties are themselves anisotropic. One model which does take account of fibre anisotropy is Hashin's composite cylinder assemblage (CCA) model[11, 12]. This gives closed form expressions for E_1, G_{12}, the bulk modulus and ν_{12}, and upper and lower bounds on the transverse moduli. The expressions are rather lengthy, and the interested reader is advised to refer to Hashin[11] or the appendix of Naik and Shembekar[13].

8.2.3 Off-axis behaviour and laminates

The analysis in section 8.2.1, and the properties discussed in section 8.2.2, relate purely to material where the fibres all lie with their axes in the same direction, defined to be the 1-direction of the material's local coordinate system. Practical textile reinforced composites can of course have very complex fibre architectures, so this discussion will concentrate next upon one of the simplest of such structures, a planar plate constructed using layers of non-crimp textile reinforcement. The analysis which follows may be found in almost any text on composite materials, such as those by Hull and Clyne[2] and Jones[3]. A global Cartesian coordinate system provides a frame of reference for definition of stresses and strains in each layer, and for the overall loads on and deformations of the plate: the x and y axes are coplanar with the plate and the z axis is perpendicular to the plate and measured from its mid-surface. Consider a thin lamina within such a structure, with its fibre axes orientated at angle θ to the global x direction. The stresses present in that lamina may be expressed in terms of the in-plane strains which that lamina undergoes:

$$\begin{Bmatrix} \sigma_x \\ \sigma_y \\ \tau_{xy} \end{Bmatrix} = \begin{bmatrix} \overline{Q}_{11} & \overline{Q}_{12} & \overline{Q}_{16} \\ \overline{Q}_{12} & \overline{Q}_{22} & \overline{Q}_{26} \\ \overline{Q}_{16} & \overline{Q}_{26} & \overline{Q}_{66} \end{bmatrix} \begin{Bmatrix} \varepsilon_x \\ \varepsilon_y \\ \gamma_{xy} \end{Bmatrix} \qquad 8.12$$

where $\overline{Q}_{11}$ etc. are the elements in the off-axis reduced stiffness matrix $[\overline{\boldsymbol{Q}}]$ of the lamina. Note that in general there are no zero terms in the $[\overline{\boldsymbol{Q}}]$ matrix: this denotes that stretch along either the x or y axis will result in shearing of the lamina (Fig. 8.4).

$[\overline{\boldsymbol{Q}}]$ is related to $[\boldsymbol{Q}]$ by the following fourth rank tensor transformations:

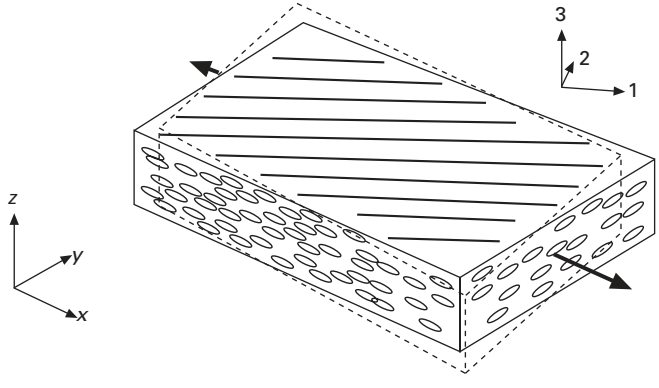

8.4 Example of tension-shearing coupling in an off-axis composite.

$$\begin{aligned}
\overline{Q}_{11} &= Q_{11}m^4 + Q_{22}n^4 + 2(Q_{12} + 2Q_{66})m^2n^2 \\
\overline{Q}_{22} &= Q_{11}n^4 + Q_{22}m^4 + 2(Q_{12} + 2Q_{66})m^2n^2 \\
\overline{Q}_{12} &= (Q_{11} + Q_{22} - 4Q_{66})m^2n^2 + Q_{12}(m^4 + n^4) \\
\overline{Q}_{66} &= (Q_{11} + Q_{22} - 2Q_{12})m^2n^2 + Q_{66}(m^4 + n^4 - 2m^2n^2) \\
\overline{Q}_{16} &= (Q_{11} - Q_{12} - 2Q_{66})m^3n - (Q_{22} - Q_{12} - 2Q_{66})mn^3 \\
\overline{Q}_{26} &= (Q_{11} - Q_{12} - 2Q_{66})mn^3 - (Q_{22} - Q_{12} - 2Q_{66})m^3n
\end{aligned} \tag{8.13}$$

in which $m = \cos\,\theta$ and $n = \sin\,\theta$.

In practice a composite laminate will be made up, for instance, of layers of non-crimp textile reinforcement with each *i*th layer of fibres within this architecture having its own ply angle θ_i and hence its own off-axis stiffness matrix $[\overline{\boldsymbol{Q}}]_i$. It is then standard bookwork to use *classical laminated plate theory* or *classical laminate theory* (CLT) to assemble the three stiffness matrices $[\boldsymbol{A}]$, $[\boldsymbol{B}]$ and $[\boldsymbol{D}]$ which relate the forces $\{\boldsymbol{F}\}$ and moments $\{\boldsymbol{M}\}$ per unit of plate length (the 'unit forces and moments') to the mid-plane strains $\{\boldsymbol{\varepsilon}^0\}$ and curvatures/twists $\{\boldsymbol{\kappa}\}$ with which the laminate deforms:

$$\begin{Bmatrix} N_x \\ N_y \\ N_{xy} \end{Bmatrix} = \begin{bmatrix} A_{11} & A_{12} & A_{16} \\ A_{12} & A_{22} & A_{26} \\ A_{16} & A_{22} & A_{66} \end{bmatrix} \begin{Bmatrix} \varepsilon_x^0 \\ \varepsilon_y^0 \\ \gamma_{xy}^0 \end{Bmatrix} + \begin{bmatrix} B_{11} & B_{12} & B_{16} \\ B_{12} & B_{22} & B_{26} \\ B_{16} & B_{26} & B_{66} \end{bmatrix} \begin{Bmatrix} \kappa_x \\ \kappa_y \\ \kappa_{xy} \end{Bmatrix} \tag{8.14}$$

and:

$$\begin{Bmatrix} M_x \\ M_y \\ M_{xy} \end{Bmatrix} = \begin{bmatrix} B_{11} & B_{12} & B_{16} \\ B_{12} & B_{22} & B_{26} \\ B_{16} & B_{26} & B_{66} \end{bmatrix} \begin{Bmatrix} \varepsilon_x^0 \\ \varepsilon_y^0 \\ \gamma_{xy}^0 \end{Bmatrix} + \begin{bmatrix} D_{11} & D_{12} & D_{16} \\ D_{12} & D_{22} & D_{26} \\ D_{16} & D_{26} & D_{66} \end{bmatrix} \begin{Bmatrix} \kappa_x \\ \kappa_y \\ \kappa_{xy} \end{Bmatrix} \tag{8.15}$$

where:

$$\begin{aligned}
A_{ij} &= \sum_{k=1}^{n} (\overline{Q}_{ij})_k \cdot (z_k - z_{k-1}) \\
B_{ij} &= \frac{1}{2} \sum_{k=1}^{n} (\overline{Q}_{ij})_k \cdot (z_k^2 - z_{k-1}^2) \\
D_{ij} &= \frac{1}{3} \sum_{k=1}^{n} (\overline{Q}_{ij})_k \cdot (z_k^3 - z_{k-1}^3)
\end{aligned} \tag{8.16}$$

in which z_k and z_{k-1} are the through-thickness coordinates of top and bottom surfaces respectively of the *k*th layer. While CLT is a commonly used approximation to the behaviour of composite laminates, it is just that: an

approximation, based upon a number of simplifying assumptions generally known as the Kirchhoff–Love assumptions, which include the assumption that initially straight section lines passing perpendicularly through the laminate (sometimes known as normals) remain perpendicular and straight during deformation (Fig. 8.5).

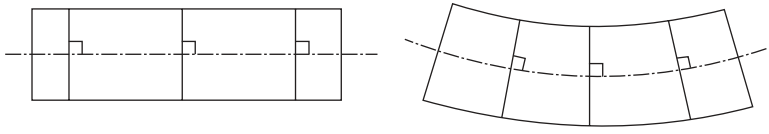

8.5 Section through shear-rigid plate illustrating the assumption of non-deformable normals.

This implies a constraint against transverse shearing effects, and is a 2D extension of the well-known assumption in engineering beam theory that initially plane perpendicular sections remain plane and perpendicular. In fact the transverse shear stiffness of practical laminates, especially those made using carbon fibre reinforcements, can be very low relative to their in-plane stiffness especially if they are of significant thickness. In order to model the behaviour of such a laminate accurately, it is necessary to relax the assumption of non-deformable normals by using a shear-deformable analogue of CLT. Such theories can assume, with progressively increasing levels of complexity, that the normals remain straight but not normal (e.g. Fig. 8.6), or that they deform from straightness following a polynomial function, or that they follow a more complex mode of deformation still, e.g. a piecewise function possibly involving exponentials. The interested reader is referred to the book of Reddy[14] and to papers by Soldatos and coworkers[15, 16], which generalise a range of approaches and develop advanced versions of such theories whose results closely approximate the exact results obtainable from 3D elasticity. Theoretical discussion of such approaches is beyond the scope of the present chapter, but the concepts of 'thin' (shear-rigid) and 'thick' (shear-flexible) plate and shell assumptions will be further discussed in the context of finite elements.

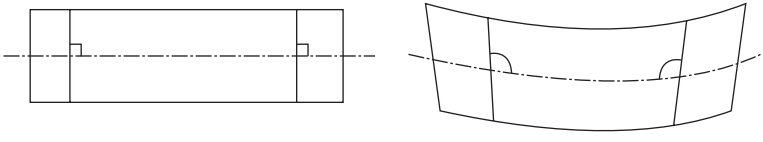

8.6 Section through plate illustrating the assumption of uniform transverse shear deformation.

8.2.4 Analysis of practical textile-reinforced composites

Analysis of homogeneous composite materials, whether they be orthotropic, anisotropic or quasi-isotropic, can be handled via the kind of mathematical

techniques described earlier. Textile composites, especially those made from woven textiles, are, however, inhomogeneous and typically have properties that vary continuously throughout the structure. In the latter case there are no easy and accurate answers, although some useful approximations can be obtained. Useful overviews of some of the possible approaches are provided by Hofstee and van Keulen[17] and Tan *et al.*[18]; a selection of the most important ones are outlined here.

Analysis of non-crimp textile composites

For non-crimped (stitch-bonded) textile composites, laminate theory can be used directly since the fibres remain substantially straight without serious localised waviness, and each group of fibres retains a distinct position within the laminate structure which may quite properly be discretised into plies. However, the following factors may need to be taken into account:

- Such textiles are often used where significant forming or draping is required, and this can greatly affect the content of fibres lying in particular directions. The effects of this behaviour on elastic properties have been modelled recently by Crookston *et al.*[19], but this is by no means standard practice.
- Since there is only fairly loose constraint on the positions of the tows especially within non-crimped fabrics, statistical variations in fibre direction, content, etc., may be significant and may in turn have a significant effect upon the mechanical properties. This issue is under investigation at the University of Nottingham, and an overview of the subject is presented by Long *et al.*[20]
- In some textile reinforcements (e.g. those that are predominantly unidirectional, having 95% of fibres in the 0° direction and the remaining 5% in the 90° direction) the tows clearly retain their distinctive shape and the true structure is not truly made up of uniform layers of differing thickness. Similarly, the true shape of the tows means that in some cases 'nesting' between successive layers can occur. As far as can be ascertained, these issues have not yet been fully investigated although the effects of tow shape and related issues are again under investigation at Nottingham[21].

Analysis of woven, braided and knitted textiles

By contrast, woven, braided and knitted textiles have more complex structures and their composites require a more detailed treatment. Leaving aside knitted textiles, a range of models of increasing complexity can be used to obtain the elastic properties of composites with crimped tows. There is a clear trade-off between the manual and computational effort involved and the accuracy obtained, although even the most complex approaches still result in errors of

several per cent compared with experimental values. The simplest and least accurate approach is to ignore the true fibre architecture of the textile reinforcement and simply to treat each set of tows as being a different layer with a given orientation within a uniform laminate. Such an approach ignores the reduction in strength and stiffness due to fibre waviness or crimp. In modelling approaches that attempt to model the fibre architecture, a so-called representative (or repeating) volume element (RVE), sometimes called a unit cell, is considered, and suitable boundary conditions at its edges are assumed so that the behaviour of this element can be extrapolated to that of a continuous sheet of the composite. One extension of the laminate approach, which takes account of the fibre crimp, is that due to Hofstee and van Keulen[17], and will be considered later. An alternative extension to this approach, sometimes termed the mosaic approach, treats the textile composite as a laminate with a laminate sequence which varies continuously over the RVE, and Naik and Shembekar's model[13] follows this approach again taking account of fibre crimp. Such approaches are essentially 2D simplifications of a highly complex 3D structure and stress system.

An alternative approach discretises the volume of the RVE into small sub-cells or voxels; there are several variants on this approach including those described by Bogdanovitch and Pastore[1] and the approach of Bigaud and Hamelin[22] described later. More rigorous still is the use of 3D models of the RVE which separately model the true or idealised geometry of the fibre tows and the regions of matrix between them using solid finite elements. Such an approach has been used by Chapman and Whitcomb[23] and many others, and this body of work is explored below. While such an approach may be regarded as a true simulation of the physical situation, the meshes required are large and complex, and the data preparation and run times are both considerable. With the automation of the mesh generation process and the increasing power of computers, such an approach is becoming more attractive; however, it is more appropriate in the present discussion to review some examples of simpler approaches that enable the engineer to approximate the behaviour of a textile composite without undertaking a major analysis task.

Iso-stress and iso-strain assumptions

Of the analytical approaches that take account of the variations of properties over the textile composite, there are two main sets of assumptions used in averaging the varying effective properties over a representative length, volume or area. These are known as iso-stress and iso-strain assumptions, or alternatively as the series and parallel models respectively. In its 1D form, the iso-stress assumptions regard elemental lengths of the composite as being subjected to equal stress and effectively acting as elastic elements or springs in series. The iso-strain assumption regards elemental lengths as being subjected

to equal strain; this is normally equivalent to placing their stiffnesses in parallel. In practice, a combination of both approaches is often used, with the local elastic behaviour being averaged over the length, area or volume of an RVE or unit cell of the composite.

Approaches based upon classical laminate theory

Hofstee and van Keulen[17] use a simplified geometry of a crimped tow[24] within a plain weave composite, consisting of straight and curved (circular arc) segments, to obtain equivalent properties for the crimped tow in each direction (Fig. 8.7). Either iso-stress or iso-strain assumptions may be made,

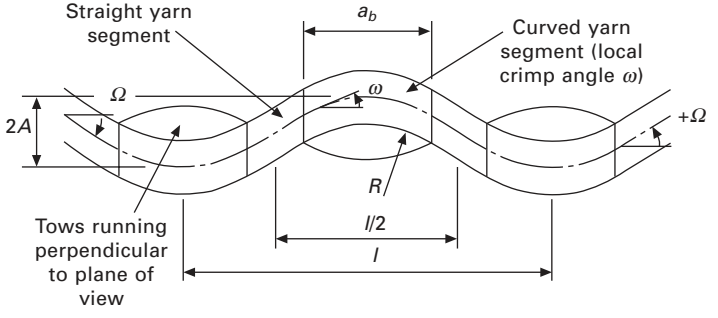

8.7 Crimped tow geometry assumed by Hofstee (adapted from references 17 and 24).

involving integration of the locally transformed compliances or stiffnesses of the tow as the fibre crimp angle changes. The resulting volume averaged stiffnesses $\langle \boldsymbol{C} \rangle$ are (for the iso-strain assumption):

$$\langle \boldsymbol{C} \rangle^{\varepsilon} = \frac{a_b}{l\Omega} \int_{-\Omega}^{\Omega} \boldsymbol{C}(\omega) \mathrm{d}\omega + \left(\frac{1}{2} - \frac{a_b}{l} \right) [\boldsymbol{C}(-\Omega) + \boldsymbol{C}(\Omega)] \qquad 8.17$$

and (for the iso-stress assumption):

$$\langle \boldsymbol{C} \rangle^{\sigma} = \left\{ \frac{a_b}{l\Omega} \int_{-\Omega}^{\Omega} \boldsymbol{S}(\omega) \mathrm{d}\omega + \left(\frac{1}{2} - \frac{a_b}{l} \right) [\boldsymbol{S}(-\Omega) + \boldsymbol{S}(\Omega)] \right\}^{-1} \qquad 8.18$$

where $\boldsymbol{C}(\omega)$ and $\boldsymbol{S}(\omega)$ are respectively the transformed stiffness and compliance matrices at the local crimp angle ω of the curved portion of the fibre, and Ω is the maximum crimp angle. The resulting crimped tow properties are used within a simplified model of each textile layer within the laminate, consisting of separate sub-layers representing the warp, weft (fill) and resin components of the layer.

This model is then used as the basis of a parametric study of the variation on modulus with shear angle (to represent deformation during draping), along with a study of the effect of fabric stretching (resulting in straightening of one set of tows at the expense of increasing the crimp in the other set). It is found that the iso-strain version of the model yields results that are almost identical to those of the model when crimp is neglected, while the iso-stress version yields moduli in the fibre directions which are significantly lower (around 10–30% lower) than those obtained using the iso-strain version. The results of the two versions of the model are compared with experimental data[25] and it is found that in the direction of the fibres, the effects of crimp become significant and the iso-stress version of the model yields results in closer agreement with experiment than the iso-strain version.

The iso-stress and iso-strain concepts are combined with CLT in the approach by Naik and Shembekar[13] for the analysis of unsheared woven composites. Two main variants of the theory are presented, both of which involve discretising a representative volume element of the composite along and perpendicular to the direction of loading relevant to each property. In contrast to the simple application of iso-stress and iso-strain assumptions to the averaging of tensile stiffnesses, the approach of Naik and Shembekar[13] involves the averaging of direct, bending and coupling stiffnesses over the representative volume element of the composite. In the parallel–series (PS) model, the components $A_{ij}(x, y)$, etc., of the local laminate stiffness matrices $[\boldsymbol{A}]$, etc. at position (x, y) are averaged across the width perpendicular to the loading (x) direction following an iso-strain assumption:

$$\overline{A}_{ij}^{p}(x), \overline{B}_{ij}^{p}(x), D_{ij}^{p}(x) = \frac{1}{a_{\mathrm{f}} + g_{\mathrm{f}}} \int_{0}^{a_{\mathrm{f}}+g_{\mathrm{f}}} A_{ij}(x, y), B_{ij}(x, y), D_{ij}(x, y)\,\mathrm{d}y \qquad 8.19$$

where a_{f} and g_{f} are respectively the width of the fill tows and of the gaps between them. These averaged stiffnesses $\overline{A}_{ij}^{p}(x)$, etc., are then inverted and the resulting compliances $\overline{a}_{ij}^{p}(x)$, etc., are averaged along the loading direction x according to an iso-stress assumption:

$$\overline{a}_{ij}^{ps}, \overline{b}_{ij}^{ps}, \overline{d}_{ij}^{ps} = \frac{1}{a_{\mathrm{w}} + g_{\mathrm{w}}} \int_{0}^{a_{\mathrm{w}}+g_{\mathrm{w}}} \overline{a}_{ij}^{p}(x), \overline{b}_{ij}^{p}(x), \overline{d}_{ij}^{p}(x)\,\mathrm{d}x \qquad 8.20$$

where a_{w} and g_{w} are respectively the width of the warp tows and of the gaps between them. These averaged compliances are finally used to calculate the equivalent moduli and Poisson's ratio. In the SP model, an iso-strain approach is used to average the laminate compliances along the loading direction. These averaged compliances are inverted and used in turn with an iso-stress assumption by averaging across the width perpendicular to the loading direction. Finally, the resulting overall laminate stiffnesses are inverted to give the

overall compliances and hence the equivalent moduli and Poisson's ratio. The authors compare the results of these two methods with 1D parallel and series models and with experimental results and conclude that the PS approach gives results in best agreement with experiment.

Approaches based upon sub-cells or voxels

Another approach combining the iso-stress and iso-strain assumptions is that of Bigaud and Hamelin[22]. While they initially explored the use of rigorous finite element (FE) models of unit cells, they turned away from this approach owing to the difficulties in automatic meshing and the long run times involved. Instead, they divide the unit cell into voxels or sub-cells for which the properties of each sub-cell are scaled according to the number of sub-cell vertices lying within a given yarn or tow. The sub-cell properties are then averaged over the unit cell using different combinations of iso-stress and iso-strain assumptions as appropriate. For example, for calculating the direct modulus in a given direction (say the y direction), the stiffnesses are averaged over each slice in the x–z plane according to an iso-strain assumption before inverting the results and averaging the resulting compliances in the y direction according to an iso-stress assumption and using the overall compliance to calculate the modulus. A broadly similar approach is used for calculating the Poisson's ratios. By contrast, the shear moduli are calculated from global shear stiffnesses which are purely the averages of the relevant sub-cell stiffness terms. The authors compare the results from their analytical model with those from a numerical approach, and demonstrate that the various results agree within a few per cent for the moduli but their results for the Poisson's ratios (especially in the plane perpendicular to the fibre direction) are in less good agreement with the alternative solutions.

Approaches based upon 3D FE modelling of the unit cell

Reference has already been made to the difficulties of this approach, although it is potentially the most accurate method for predicting elastic and failure behaviour of textile composites. In its most rigorous form, it involves constructing an FE model of an RVE of the textile using 3D continuum elements (see section 8.2.5) that replicates the idealised fibre architecture of the textile, with separate regions to represent the directional (orthotropic) tows and the isotropic matrix material. Two of the earliest examples of this approach appear to be those of Whitcomb[26] and of Guedes and Kikuchi[27]. This theme has been continued in more recent work, for example by Chapman and Whitcomb[23] and by Ng *et al.*[28]. Dasgupta *et al.*[29] similarly predicted the elastic moduli and coefficients of thermal expansion using unit cell FE models. Several later authors, e.g. Zako *et al.*[30], have used this approach within a

non-linear analysis to obtain predictions of the development of damage within the composite material, while other authors, e.g. Aitharaju and Averill[31], have used 3D FE unit cell models as a method of validating simpler and more computationally efficient approaches to obtaining material properties. There are two main difficulties associated with the use of full 3D models of the tow/matrix architecture:

1. The geometry, especially of the matrix region, involves very complex shapes with features that are very difficult to mesh. For example, there are thin sections between converging surfaces of tows as they cross, leading to the potential for very distorted elements. This makes the construction of the model non-trivial, making the use of links with solid modelling techniques[32, 33] and/or fibre architecture models[34] highly desirable. Improved availability of solid modelling systems and the increasing integration of solid modelling with FE can help with this issue.
2. The number of elements involved in such a 3D mesh can become very large especially as mesh convergence studies are undertaken. While ongoing improvements in computing mean that this problem will become less significant with time, the problem nonetheless remains that complete convergence of calculated stresses may not be practical.

It must be concluded that at present the use of 3D FE models provides a valuable research tool for predicting tow-level behaviour within a textile composite, at the expense of considerable data preparation and run time. An example analysis produced using this approach is shown in Fig. 8.8. This represents uniaxial loading of a 2×2 twill weave fabric, where the mesh was generated automatically using the University of Nottingham 'TexGen' textile modelling software[34].

8.2.5 Finite element modelling of textile composite components

For all components except the most simple, it is likely that structural analysis will be undertaken using the finite element method (FEM), in which the structure is broken down into small regions whose constitutive properties are easily evaluated, prior to assembling a mathematical model of the global behaviour of the system from the properties of all the elements. It is not appropriate here to provide a detailed overview of the FEM, although numerous comprehensive texts exist (for example the standard text by Zienkiewicz and Taylor[35]) and a brief overview of the FEM in the context of composite materials is given by Owen *et al.*[4] However, it is useful to explore the kinds of elements that are available in the analysis of textile composites.

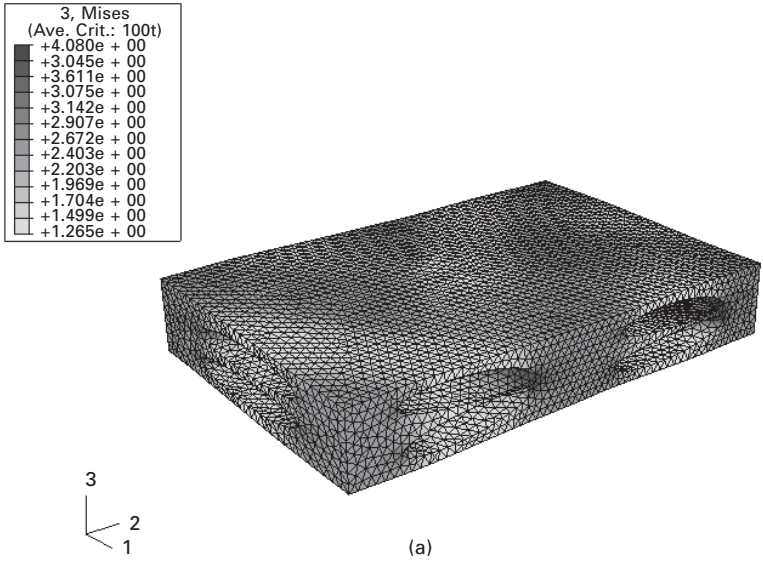

8.8 Example 3D FE analysis for a 2 × 2 twill weave glass/polyester composite. (a) Von Mises stress distribution in the matrix; (b) stress in the fibre direction for the impregnated tows.

Elements for analysing thin laminates

These are usually extensions of thin shell isotropic elements. Four independent elastic constants (normally E_1, E_2, ν_{12} and G_{12}), along with the orientation of the material's principal directions (relative to a global or local coordinate system), are required to define each layer. A layer is assumed here to consist of a ply or group of plies having a given set of orthotropic material properties orientated at a single angle. In practice, it may consist of one of the sets of tows in a non-crimp fabric ply or even (as a crude approximation, or with the properties modified as in the method of Hofstee and van Keulen[17]) one of the sets of tows in a woven fabric. Material directions will normally lie parallel to the laminate mid-surface, and care must be taken that the material directions are correctly specified so that this is indeed the case. Thin shell elements typically have five or six degrees of freedom (DOFs) at each node: three displacement DOFs, along with two or three rotational DOFs to enforce continuity of slope between elements. A range of different element topologies are available: these include three-noded elements (which have rather poor accuracy, resulting in a need for many elements in order to obtain a converged solution), four- or eight-noded triangular elements (which use higher orders of interpolation to overcome the problems of the three-noded elements) and eight-noded quadrilateral elements (see Fig. 8.9). These shell elements are applicable to thin shells where transverse shear strains have little effect, and the Kirchhoff–Love assumption of zero transverse shear strain may be enforced mathematically (i.e. analytically, within the formulation) over the whole element or numerically at certain points on the element (but permitting slight shearing elsewhere).

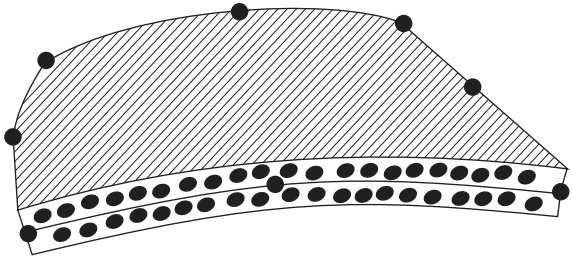

8.9 Eight-noded, doubly curved laminated quadrilateral shell element.

Elements for analysing moderately thick laminates

Thin shell elements are adequate for reasonably thin metallic plates and shells, but composites are very flexible in transverse shear relative to their overall (direct and bending) stiffness. It is therefore necessary to take account of transverse shearing for moderately thick laminates or poor results will be

obtained. So-called 'thick shell' or shear-deformable plate and shell elements are therefore used. Instead of the Kirchhoff–Love assumptions these use the Reissner–Mindlin assumption, which may be stated as: 'straight sections remain straight but do not necessarily remain normal'.

G_{23} and G_{31} must now be considered in order to take account of transverse shear stiffness. Nodal degrees of freedom still usually consist of three displacements and three rotations but the rotations now represent the combined effects of mid-surface rotation of the shell due to bending, and rotation of shell normals (relative to the mid-surface) due to shearing. It should be noted that when transverse (interlaminar) shear stresses are calculated (either from thin shell or thick shell elements), they are usually reconstructed using equilibrium considerations, not calculated directly from the strain field assumed above.

Although 'thick shell' elements are able to model transverse shearing effects, they do have a pitfall. If they were to be used for modelling of thin laminates where shearing deformations are insignificant, a spurious mode of energy storage occurs within the element leading to so-called 'shear locking', a stiffening of the element that tends to rigid behaviour as the shell thickness tends to zero. Some care is therefore needed when deciding whether to use 'thin' or 'thick' shell elements (or even 3D elements), although it is very difficult to give clear guidance on this issue and there is no substitute for experience and benchmarking.

As implied by the lists of engineering properties required for each type of element, it is normally necessary to specify equivalent elastic properties of each ply of textile-reinforced composite. An alternative form of the input data is the set of laminate stiffnesses (i.e. $[\boldsymbol{A}]$, $[\boldsymbol{B}]$, $[\boldsymbol{D}]$ and the transverse shear stiffnesses). Some of the approaches for predicting these elastic constants for textile composites were presented in section 8.2.4.

3D orthotropic elements

These are of limited usefulness for modelling conventional (2D) textile composite laminates, although they are useful where solid pieces of composite are to be modelled. They could also be used in the modelling of composites manufactured from thick (3D) textiles such as 3D woven or braided reinforcements. Moreover, they are essential in the creation of 3D models of representative volume elements or unit cells of textile composites. Typical 3D elements are shown in Fig. 8.10.

In most FE systems, all the usual 3D elements are available with orthotropic properties, e.g. 4- and 10-noded tetrahedral, and 8- and 20-noded 'bricks', along with other geometries including wedge elements, and orthotropic plane stress, plane strain and generalised plane strain 2D elements.

Some FE systems allow layered bricks and other layered 3D elements,

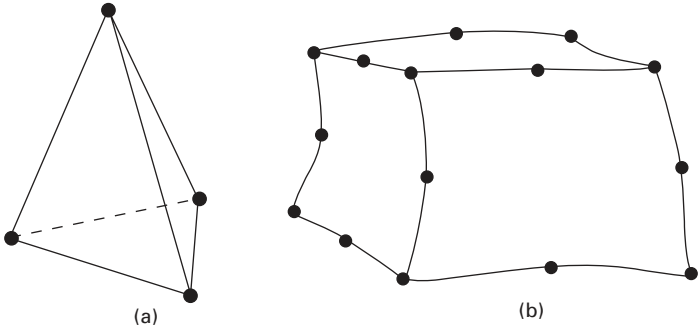

8.10 Conventional 3D solid elements with the opportunity to use orthotropic properties: (a) four-noded tetrahedron and (b) twenty-noded hexahedron ('brick').

which form a useful halfway house between explicitly modelling each layer separately with its own 3D elements and using shell elements. However, once again, care must be taken to ensure that the fibre directions are correctly specified for each layer.

8.2.6 Conclusions

This section has examined the elastic behaviour of composite materials in general, with particular emphasis on the difficulties of extending this kind of analysis to cope with the complex fibre architectures found in composites made with woven and braided textiles. It may be concluded that, as with any form of engineering analysis, there is a trade-off between the accuracy obtained using a given analysis method (ranging from simplistic treatment of different tow sets as different plies, though to rigorous 3D finite element modelling of representative volume elements) versus the complexity of the analysis and the computational and data preparation times involved. Furthermore, only elastic properties have been considered thus far, whereas the onset of failure and the progression of damage will be examined in the following section.

8.3 Failure and impact behaviour

Impact and failure analysis of textile composites is appreciably more difficult than for metals owing to the complexity and multitude of failure modes that can occur. Possible failure modes include, among others, tensile fibre failure, compressive fibre buckling, matrix crushing, transverse matrix cracking, fibre–matrix debonding and delamination between adjacent plies in the case of a laminated textile composite. The interaction of these failure modes further complicates the problem, making a predictive numerical simulation difficult, but not impossible. This section illustrates some of the numerical

methods that are often employed for such simulations. For the purpose of this discussion the methods outlined are typical of those currently available in some commercial FE analysis codes.

Most textile composites comprise one or more plies laid over each other to form a laminate. The plies may be unidirectional or bidirectional, or more intricate weaves and knits which are bound together with resin that is either pre-impregnated, or post-impregnated using an injection process. Regardless of the manufacturing route, the basic laminate comprises plies and resin interfaces, each of which may independently, or concurrently, fail during excessive loading. Other types of textile composites could have a 2.5D or 3D architecture in which yarns are intertwined through the thickness direction; this will eliminate delamination failure.

A large body of experimental and analytical work on the failure of composites and textile composites is available in the literature; see for example Hinton *et al.*[36] and Cox and Flanagan[37]. However, for practical analysis and failure prediction of large-scale composite structures only the FE technique is suitable and is, therefore, the only method to be discussed here. Two popular FE methods are available; namely, the implicit and explicit techniques, each of which has its advantages and disadvantages[38]. The two methods are briefly introduced, followed by some composite failure modelling approaches that are equally applicable to both analysis techniques.

8.3.1 Solution strategies for FE failure analyses

Usually commercial FE codes use either an implicit or an explicit solution to perform an analysis. The two solution algorithms render each method more, or less, appropriate to different classes of problems. Generally, implicit methods are most suitable for straightforward failure analysis, particularly if the loading is 'static', while explicit methods are more appropriate for dynamic, highly non-linear problems which would include composites impact (and crash) analysis.

The implicit method is most commonly used in general-purpose FE codes for linear and non-linear problems. Essentially implicit FE analysis requires the composite structure to be discretised using (modelled as) an assembly of appropriate finite elements. Each element has a stiffness matrix dependent on the material constitutive relationship and the nature of the chosen element. Each element stiffness matrix is computed and assembled to give the global structure stiffness matrix $[K]$. This matrix provides the relationship between nodal displacements $\{u\}$ and applied nodal forces $\{P\}$ of the structure:

$$\{P\} = [K]\ \{u\} \quad \text{or} \quad \{u\} = [K]^{-1}\ \{P\} \tag{8.21}$$

In contact and non-linear material problems, such as impact analyses for composites, the matrix $[K]$ is not constant and iterative solution schemes are

necessary to find the nodal displacements for a given applied loading. Often these solution schemes require repetitive assembly and inversion of the global stiffness matrix, which can be prohibitively expensive and unreliable.

In recent years the explicit method has become popular for highly non-linear dynamic problems, especially if contact between bodies is involved: crashworthiness and impact simulation are two notable examples. The same meshing techniques used in the implicit method are used to discretise the structure. The difference is the solution algorithm and the problem is now formulated as a dynamic problem using the linearised equations of motion, from which a solution in the time domain is obtained:

$$[M]\{\ddot{u}\}_n + [C]\{\dot{u}\}_n + [K]\{u\}_n = \{F_{\text{ext}}\}_n \tag{8.22}$$

where $\{u\}$, $\{\dot{u}\}$ and $\{\ddot{u}\}$ are vectors of nodal displacement, velocity and acceleration, n is the cycle number at time position T_n (after n time steps each of length ΔT); $[M]$, $[C]$ and $[K]$ are the mass, damping and stiffness matrices respectively and $\{F_{\text{ext}}\}$ is a vector of applied external nodal forces. Material damping can be neglected in short duration dynamic problems and, replacing the term $[K]\{u\}_n$ with the equivalent internal nodal force vector $\{F_{\text{int}}\}$, this gives Newton's second law of motion,

$$[M]\{\ddot{u}\}_n = \{F_{\text{ext}}\}_n - \{F_{\text{int}}\}_n \tag{8.23}$$

If a lumped mass distribution is assumed the mass matrix $[M]$ is diagonal and a solution for nodal accelerations $\{\ddot{u}\}$ is trivial:

$$\{\ddot{u}\}_n = [M]^{-1}(\{F_{\text{ext}}\} - \{F_{\text{int}}\})_n \tag{8.24}$$

The nodal velocities $\{\dot{u}\}_{n+1/2}$ and nodal displacements $\{u\}_{n+1}$ may then be obtained by integration in the time domain using the central finite difference operators:

$$\{\dot{u}\}_{n+1/2} = \{\dot{u}\}_{n-1/2} + \{\ddot{u}\}_n \Delta T_n$$
$$\{u\}_{n+1} = \{u\}_n + \{\dot{u}\}_{n+1/2} \Delta T_{n+1/2} \tag{8.25}$$

Equations 8.24 and 8.25 are 'conditionally stable' and restrict the allowable integration time step to $\Delta T_{\text{critical}}$, which is dependent on the element size and material properties.

An important advantage of the above scheme is that the system of equations are uncoupled, allowing an element-by-element solution; thus the formation and inversion of a large global stiffness matrix are not needed. Furthermore, instabilities due to sheet buckling, or material softening due to damage, are easily treated using the explicit dynamic formulation. Contact is also easily handled by first identifying its occurrence and then imposing temporary resisting 'penalty' forces, as additional external forces, in eqn 8.24. Treating these phenomena using an implicit method, where global stiffness matrices

must be assembled, inverted and used in iterative schemes to yield a solution does present formidable computational difficulties; however, linear static analysis and identification of initial failure is more easily handled.

8.3.2 Ply and delamination failure modelling

Delamination is important because it causes ply separation and loss in bending stiffness of the laminate; whereas in-plane ply failure controls in-plane stiffness and ultimate failure of the laminate. Most FE codes have ply constitutive models to treat mechanical stiffness, and they usually have a variety of popular failure models to identify rupture. Usually delamination is not considered, but some codes, including implicit[39] and explicit[40], have now implemented delamination models to characterise mechanical stiffness and failure of the resin-rich ply interface. The following sections outline the principles of ply and delamination models used in FE codes.

Ply constitutive and failure models

Most commercial FE codes allow composites to be represented using 2D shell or 3D solid elements; usually the shells are 'multilayered' so that a laminate with many plies can be treated using a single element. In each case the composite orthotropic material properties are specified in the 'fibre' frame and the relative orientation of this frame, with respect to the 'global' structural axis system, must be given. The 2D and 3D orthotropic constitutive relations are given in many composites textbooks[2, 3]; the plane stress relations for an orthotropic material are described in section 8.2.1.

Many ply failure models have been proposed that can predict failure for a given state of loading. Usually impact and crash analysis codes tend to prefer a 'damage mechanics' approach in which failure is first identified and thereafter the elastic properties are progressively reduced until full rupture occurs. The nature of the failure mode dictates whether sudden rupture and rapid damage will occur (e.g. tension), or whether slow progressive damage and energy absorption are more representative (e.g. compressive crushing).

Finite element codes often allow the user a choice of different failure criteria, or damage mechanics methods. A linear implicit analysis will provide element stresses and strains for a given applied loading. For a selected failure criterion the instance of initial material failure is then found by identifying the critical location, and linearly scaling the applied loads to achieve failure at this location (failure index $f = 1$, see below). This would correspond to 'first-ply failure', which does not necessarily represent the ultimate strength of the laminate or structure. More sophisticated FE techniques can allow this first-ply to be excluded, or certain stress components to be excluded, and further loading applied. Clearly the structure stiffness matrix must be

reformulated and iterative solution strategies are required. Alternatively, damage mechanics methods can be used in explicit (time) or implicit (load) integration schemes in which the structure is progressively loaded and the evolution of damage followed.

The following outlines some commonly used ply failure criteria; this is then followed by an example of a typical damage mechanics model. These models were originally developed for unidirectional and woven plies, but could be applied to more advanced textiles. The reader should be aware, however, that there is considerable controversy over composite failure models[41]. Nevertheless, if an appropriate test programme is conducted, in which the failure modes tested and used to define the failure law are comparable to those expected in the actual structure under consideration, then these models can be used with a good level of confidence.

Maximum stress and maximum strain

This criterion assumes failure occurs if any stress component in the fibre frame (σ_1, σ_2, τ_{12}) exceeds its corresponding allowable limit (σ_{1u}, σ_{2u}, τ_{12u}). These limits are normally determined from appropriate coupon tests. The criterion for a 2D finite element is:

$$f = \max\left(\left|\frac{\sigma_1}{X_\sigma}\right|, \left|\frac{\sigma_2}{Y_\sigma}\right|, \left|\frac{\tau_{12}}{S_\sigma}\right|\right), \quad \text{for failure } f \geq 1 \tag{8.26}$$

with,

$$X_\sigma = \sigma_{1u}^{t} \quad \text{if} \quad \sigma_1 \geq 0, \quad Y_\sigma = \sigma_{2u}^{t} \quad \text{if} \quad \sigma_2 \geq 0$$

$$X_\sigma = \sigma_{1u}^{c} \quad \text{if} \quad \sigma_1 < 0, \quad Y_\sigma = \sigma_{2u}^{c} \quad \text{if} \quad \sigma_2 < 0$$

$$S_\sigma = \tau_{12u}$$

Note that different failure limits are possible for in-plane tension (σ_{1u}^{t}) and compression (σ_{1u}^{c}). The maximum strain criterion has an identical form except that stress terms are replaced with strains and the failure quantities are now failure strains. A major concern of this model is that failure is not influenced by the interaction of the different stress–strain components.

The Tsai–Wu quadratic failure criterion

The Tsai–Wu criterion is typical of a second class of general failure criteria for anisotropic composites in which a single expression is derived to express failure. The general form of this quadratic failure criterion in stress space is given by:

$$f^2 = \sum_{i=1}^{6} F_i \sigma_i + \sum_{i,j=1}^{6} F_{ij} \sigma_i \sigma_j \qquad 8.27$$

The F_{12} term provides interaction of stress components and the differences between tensile and compressive failure stresses are introduced in the coefficient F_i, F_{ij}. For plane stress the above reduces to:

$$F_1\sigma_1 + F_2\sigma_2 + F_{11}\sigma_1^2 + F_{22}\sigma_2^2 + F_{66}\tau_{12}^2 + 2F_{12}\sigma_1\sigma_2 = f^2 \qquad 8.28$$

where

$$F_1 = \frac{1}{\sigma_{1u}^{\mathrm{t}}} - \frac{1}{\sigma_{1u}^{\mathrm{c}}}; \qquad F_{11} = \frac{1}{\sigma_{1u}^{\mathrm{t}}\sigma_{1u}^{\mathrm{c}}}$$

$$F_2 = \frac{1}{\sigma_{2u}^{\mathrm{t}}} - \frac{1}{\sigma_{2u}^{\mathrm{c}}}; \qquad F_{22} = \frac{1}{\sigma_{2u}^{\mathrm{t}}\sigma_{2u}^{\mathrm{c}}}$$

$$F_{66} = \frac{1}{\tau_{12u}^{\mathrm{p}}\tau_{12u}^{\mathrm{n}}} \qquad F_{12} = \frac{1}{2}\sqrt{F_{11}F_{22}}$$

Many similar failure criteria are available in commercial codes including, for example, the Modified Puck, Hoffmann and Tsai–Hill criteria. An excellent review of these criteria and other models, compared with test measurements, is given by Hinton *et al.*[36]

Ply failure modelling using damage mechanics

Continuum damage mechanics provides a simple method to treat ply (and delamination) failure and is often used in advanced FE codes for impact and crash analysis of composite structures. Damage is a permanent weakening of the material due to resin micro-cracking, fibre–matrix debonding, fibre failure, etc., and occurs prior to complete rupture. Its effect can be approximated by reducing (damaging) the material elastic properties via a damage parameter (d). The stress–strain relation is then given by:

$$\sigma = E_{\mathrm{d}} \cdot \varepsilon \quad \text{where} \quad E_{\mathrm{d}} = E_{\mathrm{o}}\,(1 - d) \qquad 8.29$$

The elastic and damaged moduli are E_{o} and E_{d} respectively, and d is a scalar damage parameter that varies from zero, for strains below a damage initiation strain ε_i, and increases linearly to d_u at full material damage strain ε_u. Damage d is usually linked to the state of strain or strain energy release rate. Complete material rupture at strain ε_u is easily imposed by setting the damage $d = 1$. The evolution of damage and the resulting stress–strain curve is shown in Fig. 8.11.

For orthotropic materials several material moduli are present, which may be independently, or concurrently, damaged. The essential requirement is a valid set of coupon tests that determine the mechanical properties and damage

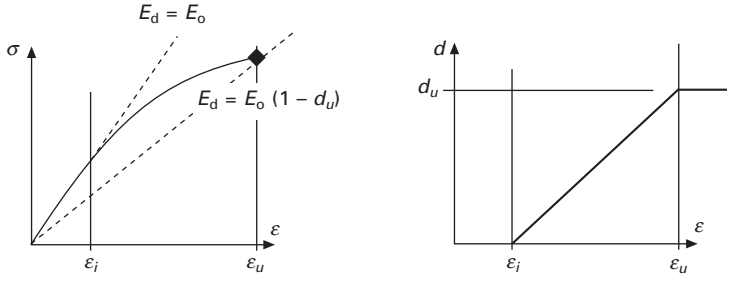

8.11 Illustration of damage mechanics: (a) variation of stress and strain; (b) Variation of damage *d*.

evolution leading to failure for each of the different possible failure modes. The following illustrate the principles and application of continuum damage mechanics to a woven fabric composite[42]; this work is an extension of a previous model originally proposed for unidirectional composites[43]. The plane stress orthotropic constitutive law with damage parameters is given by:

$$\begin{Bmatrix} \varepsilon_1 \\ \varepsilon_2 \\ \gamma_{12} \end{Bmatrix} = \begin{bmatrix} 1/E_1(1-d_1) & -\nu_{12}/E_1 & 0 \\ -\nu_{12}/E_2 & 1/E_2(1-d_2) & 0 \\ 0 & 0 & 1/G_{12}(1-d_{12}) \end{bmatrix} \begin{Bmatrix} \sigma_1 \\ \sigma_2 \\ \tau_{12} \end{Bmatrix} = [S]\{\sigma\} \qquad 8.30$$

where the compliance matrix $[S]$ comprises four undamaged elastic constants E_1, E_2, G_{12} and υ_{12} and elastic damage parameters (d_1, d_2) for the two principal fibre directions and damage parameter (d_{12}) for inelastic shear response.

Figure 8.12 shows typical force versus displacement curves for composite coupons loaded in the 0°/90° and ±45° directions (test curves are shown

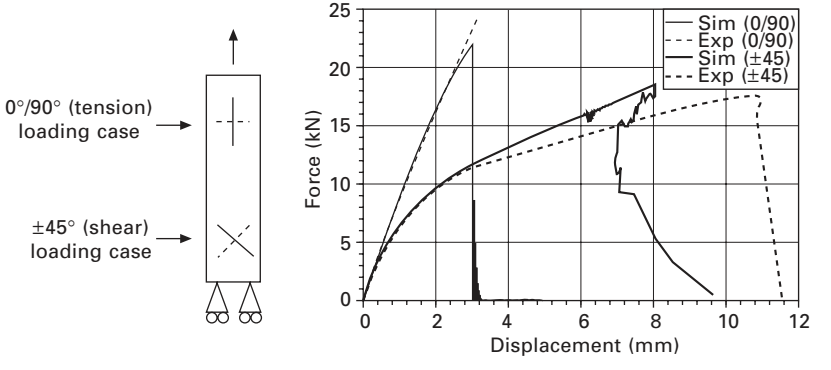

8.12 Test and simulation curves for a typical balanced glass fabric–epoxy composite under axial 0°/90° and shear ±45° loading.

dashed). The material is a woven R-glass fabric with Fibredux 924 epoxy resin. Usually at least these tests are required to determine the damage parameters d_1, d_2 and d_{12}. However, some models account for the effect of interaction of stress components on damage and additional tests are necessary; this effect will be more important for textile composites than simple UD plies. The Ladevèze model[42, 43], for example, clearly defines the test program needed and the methods to derive and specify the damage evolution parameters. Following these procedures reasonable agreement between test and simulation curves, Fig. 8.12, has been obtained using the crashworthiness FE code PAM-CRASH[40].

Delamination modelling

The detection of delamination and the ability to model its growth can have important consequences on the laminate stiffness and sequence of ply failures leading to ultimate laminate failure. Delamination also absorbs a significant proportion of impact energy and should be properly modelled in any numerical model of impact failure.

The following approach to treat delamination is gaining favour and is available in at least two commercial FE codes[39, 40]. The method involves modelling the laminate as a stack of discrete finite elements, in which each element represents one ply or a subset of plies. These elements are tied together using interface constraints that characterise the mechanical stiffness, strength and delamination energy absorption of the resin-rich interface. The interface algorithm performs two key operations; first, at the start of the calculation, matching 'pairs' of nodes and adjacent elements are identified and, second, during the calculation these matching pairs are constrained to move relative to each other dependent on a linear elastic with damage stress-displacement law. Figure 8.13 shows a schematic view of one element of the interface.

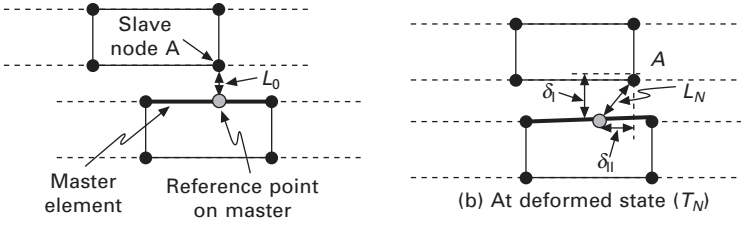

(a) The initial (undeformed) state (T_o)

(b) At deformed state (T_N)

8.13 Identification of the 'slave' node and the attached 'master' surface and the mode I (normal) and mode II (shear) separation distances.

The main features of the interface mechanical law are shown in Fig. 8.14 for normal (mode I) loading. A simple linear elastic law is assumed up to a failure stress σ_{Ic}. Thereafter, linear damaging is activated such that at final separation δ_{Imax}, the fracture energy of the fibre–resin system has been absorbed. That is, the area under the curve corresponds to the fracture energy G_{Ic} of the resin–fibre interface. Thus σ_{Imax}, δ_{Ic} and δ_{Imax} are selected so that the elastic-damage curve fulfils the required criteria. Identical arguments are used to define the normal (mode I) and shear (mode II) curves which have different parameters; typically crack growth under mode II loading will absorb about ten times the energy of mode I crack growth.

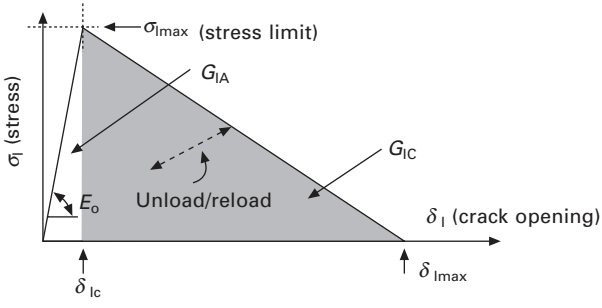

8.14 Diagram of the stress-crack opening curve for mode I loading.

The following formulae describe mode I failure; identical equations are used for mode II by interchanging E_0, σ_{Imax}, δ_I and G_{Ic} with G_0, σ_{IImax}, δ_{II} and G_{IIc}. The resin through-thickness normal modulus E_0 is used for the elastic range of the stress-displacement curve. When a maximum stress σ_{Imax} is reached, the stress displacement law follows a linear damage equation of the type:

$$\sigma_I = (1 - d_I) \cdot E_0 \cdot \varepsilon_I = (1 - d_I) \cdot E_0 \cdot \frac{\delta_I}{L_0} \qquad 8.31$$

where d_I is the damage parameter, varying between the values of 0 (undamaged) and 1 (fully damaged), E_0 is the modulus, L_0 the normal distance between the original position of the slave node and the master element and δ_I the deformed normal separation distance of the slave node and master element.

The area under the elastic range is the fracture energy required to start damage of the interface G_{IA}, and is given by:

$$G_{IA} = \frac{1}{2} \frac{\sigma_{Imax}^2}{E_0} L_0 \qquad 8.32$$

The total area under the load–displacement curve is the critical fracture energy required for failure of the interface (including the elastic and damaging zones) and is given by:

$$G_{Ic} = \frac{1}{2}\sigma_{Imax}\delta_{Imax} \qquad 8.33$$

The values of G_{Ic} and G_{IIc} can be obtained via the standard double cantilever beam (DCB) and end notched flexure (ENF) tests[44, 45] respectively, from which the necessary parameters for the model can be found.

Figure 8.15 illustrates mode I loading of a simple single element test case. Path ($\boldsymbol{a}_1$) shows the case of tensile loading. Damage initiates when σ_{Imax} is reached and path ($\boldsymbol{a}_2$) is then followed. Path ($\boldsymbol{b}_1$) represents unloading using the new partially damaged material modulus. Note that if unloading causes the gap to fully close then the original undamaged modulus is used, path ($\boldsymbol{b}_2$). Reloading follows paths ($\boldsymbol{b}_1$) and ($\boldsymbol{b}_2$) to the point where unloading initiated, after which path ($\boldsymbol{a}_3$) is followed until full failure occurs.

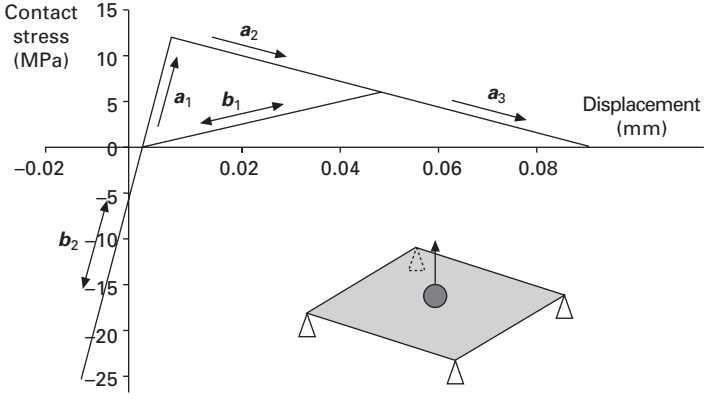

8.15 Example loading–unloading for mode I of a single element test case.

Invariably, in practice, there is a strong coupling between normal and shear loading at the interface. Indeed a specific test procedure has been devised to investigate and quantify this type of mixed mode loading using a mixed mode bending (MMB) test[46]. This work has shown that, for many materials, a linear coupling model can reasonably represent the mixed-mode failure process, thus:

$$\frac{G_I}{G_{In}} + \frac{G_{II}}{G_{IIn}} = 1 \qquad 8.34$$

where $n = A$ for the onset of fracture and $n = C$ for fracture; G_I and G_{II} are the instantaneous values and G_{In} and G_{IIn} corresponding to test values as measured by the DCB and ENF tests. Example solutions using this approach, including validation against DCB, ENF and MMB tests, have been presented by Lourenco[47]. Figure 8.16 shows the experimental set-up for a DCB test

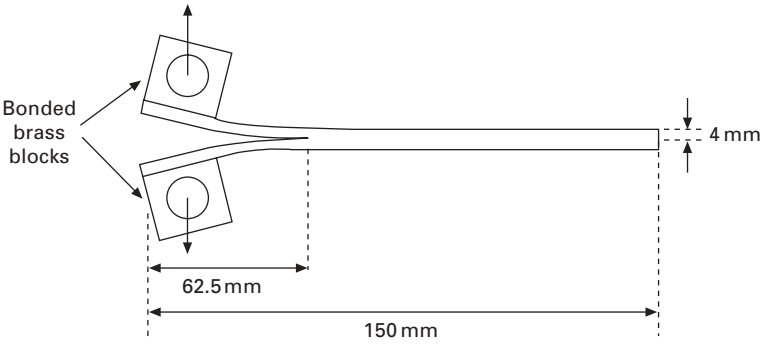

8.16 Experimental test of the double cantilever beam to determine the mode I fracture energy for a non-crimp fabric-based composite.

where the Mode I delamination crack growth in a non-crimp fabric (NCF) reinforced composite is evaluated. Figure 8.17 shows the comparison between test and simulation for this NCF laminate in which the simulation model uses the experimentally determined value for G_{IC}.

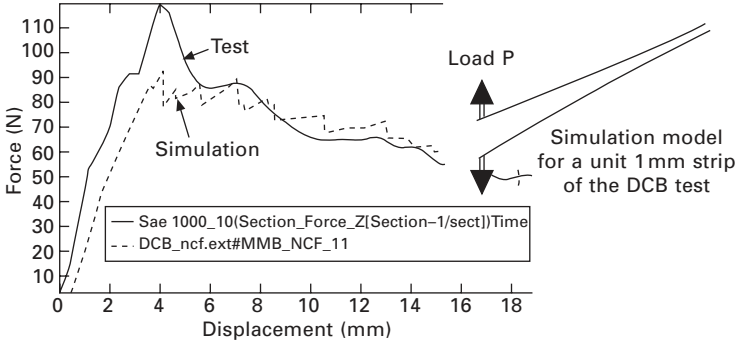

8.17

8.3.3 Examples of impact simulations of textile composites

The following examples illustrate the state-of-the-art simulation of textile composite structures under impact loading. In each case the fabric model[42] and delamination model[48] have been used in the crashworthiness simulation code PAM-CRASH.

Impact simulation of a laminated carbon fabric composite plate

The first example considers a 50 mm diameter rigid ball of mass 21 kg striking a flat, simply supported composite plate at 6.28 m/s; Fig. 8.18. The

material is a woven fabric with T300 carbon fibres and Fibredux 924 epoxy resin. The plate is 300 mm square and has 16 plies of quasi-isotropic lay-up $[(0,90)/(+45, -45)]_{4s}$, giving a thickness of 4.6 mm. A comparison of a conventional multilayered shell (no delamination) and the modelling method with delamination between plies is presented and shows the improved agreement between test and simulation results.

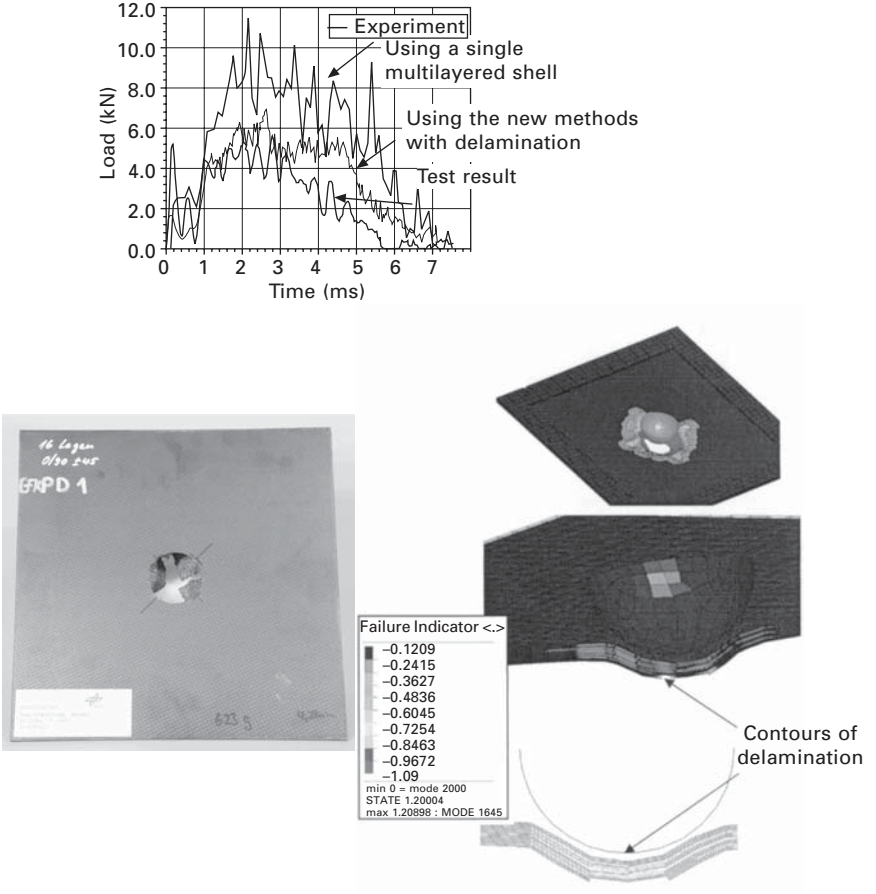

8.18 Test and simulation results for a spherical impactor striking a flat CFRP plate.

Delamination occurs initially under the impact point at the centre of the laminate, where the shear is a maximum, causing it to separate into two sublaminates. These sublaminates then delaminate at their mid-plane as the ball intrudes further into the plate creating further sublaminates and delamination until, possibly, all plies are delaminated. The prediction of extensive delamination is valuable information that agrees well with test C-

scan results. At this velocity the simulation correctly calculates penetration of the plate by the impactor; for a lower velocity of 2.33 m/s (not shown) the simulation and test both find that the punch rebounds, albeit with significant ply and delamination damage.

Impact simulation of a laminated glass fabric aircraft leading edge

A second example concerns the 'bird-strike' impact of a demonstrator aircraft leading edge constructed from woven R-glass fabric and Fibredux 924 epoxy resin. The fluid-like behaviour of the bird at high velocity is usually approximated in tests using a gelatine projectile. Smoothed particle hydrodynamics is a specialised FE technique used here for the projectile, since conventional finite elements cannot handle the excessive deformations that occur in this material. The gelatine, at high velocities, behaves like a fluid and is treated as a nearly incompressible liquid with zero shear response. The laminate is modelled using the same stacked shell with delamination interface techniques as used in the previous flat plate.

The demonstrator leading edge is approximately 200 mm long with a nose radius of 15 mm and consists of eight quasi-isotropic layers $[(0,90)/(+45, -45)]_{2s}$ giving a laminate approximately 2 mm thick. The gelatine has a mass of 30 g and impact velocity of 132 m/s. Test and simulation results are shown in Fig. 8.19. The delamination zone for the test part is marked on the photo and is seen to be non-symmetric in shape and extends over a large area. The numerical model predicts a comparable total area of delamination which is, as may be expected, symmetric about the impact point. The general agreement of the global area of delamination damage is encouraging. Most probably the difference in the areas affected is due to off-centre impact loading in the test. The analysis does correctly compute deflection of the gelatine, without penetration, and shows similar ply damage to that observed in the test part.

Failure simulation of stitched composite 'T' joint

Within a German-funded BMBF project[49, 50] new technologies have been developed for the 'one sided' stitching of textile composite preforms. As a part of that work, the following study demonstrates the potential for simulation of stitched jointing systems. Figure 8.20 shows some details of the manufacturing process for this preform.

The previous fabric models are used to represent the 'T' and outer composite panel and the delamination model is used to represent the resin part of the interface between the 'T' and the outer panel. In addition, beam elements are used to represent the stitches; these elements have a tensile failure criterion (maximum strain) and stiffness to represent the stitching properly. Figure 8.21 shows details of the geometry and the finite element representation. Only

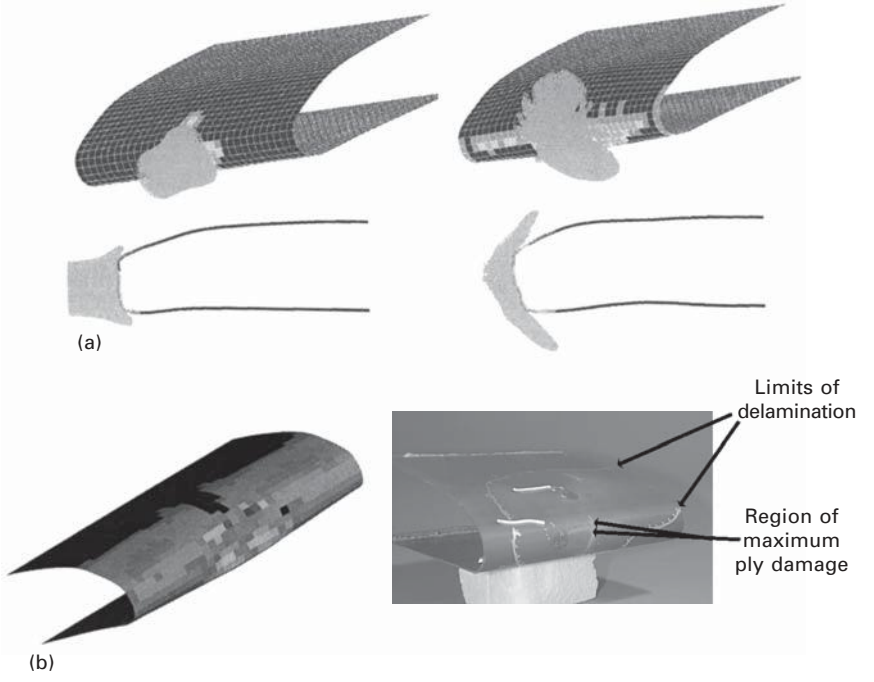

8.19 Test and simulation results for the impact of a demonstrator leading edge. (a) Early and intermediate deformation states showing the spread of the gelatine, deformation of the leading edge and the evolution of delamination damage. (b) Contours of ply damage for the centre ply (simulation and test).

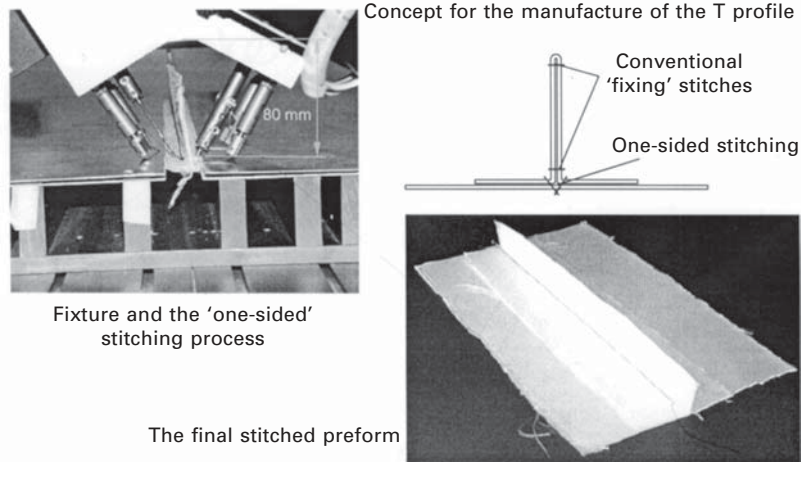

8.20 Details of the 'one-sided' stitching process to manufacture a 'T' joint preform (Courtesy: ITA Aachen).

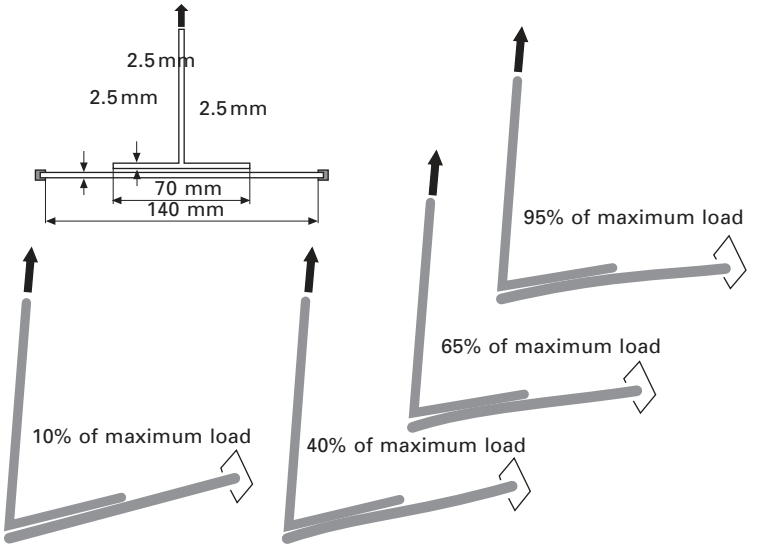

8.21 Geometry and details of the FE model for the composite 'T' joint. The composite is a quasi-isotropic lay-up of non-crimp fabric with RTM6 (Hexcel) epoxy resin.

one symmetric half of a unit strip of the 'T' joint is analysed. In this figure a double chain stitch is used at distances 10 and 30 mm from the symmetry line. Loading is in tension at the free end of the 'T' profile and contours of delamination growth are shown as a function of the maximum failure load.

A simple parametric study, Fig. 8.22, shows the importance of the location

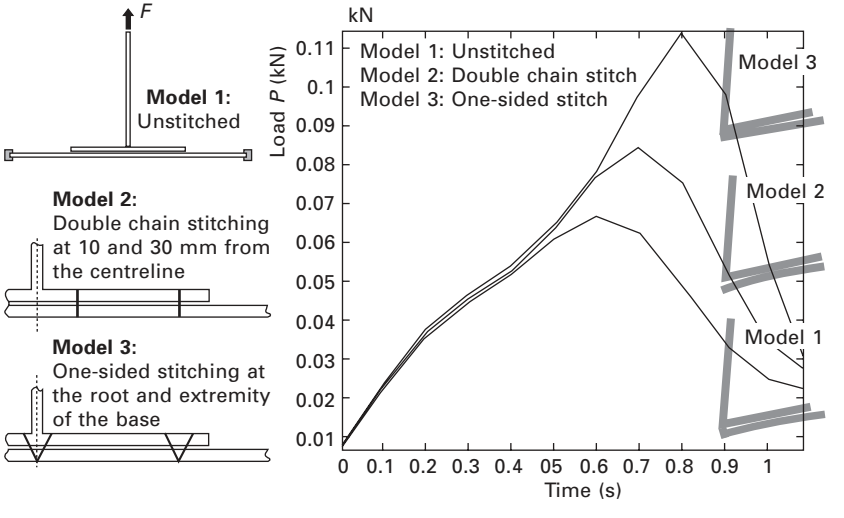

8.22 Example parametric study to optimise stitch location for loading.

of the stitching on the maximum failure load. A 40% increase in failure load can be achieved using optimally located stitching compared with the unstitched case.

8.4 References

1. Bogdanovich A. and Pastore C., *Mechanics of Textile and Laminated Composites*, Chapman and Hall, London, 1996.
2. Hull D. and Clyne T.W., *An Introduction to Composite Materials,* 2nd edn, Cambridge University Press, Cambridge, 1996.
3. Jones R.M., *Mechanics of Composite Materials*, 2nd edn, Taylor and Francis, Washington, DC, 1996.
4. Owen M.J., Middleton V. and Jones I.A. (eds), *Integrated Design and Manufacture using Fibre-reinforced Composites*, Woodhead Publishing Ltd, Cambridge, 2000.
5. *BS2782-10 Method 1003 EN61 Methods of Testing Plastics – Glass reinforced plastics – Determination of tensile properties*. British Standards Institute, UK, 1977.
6. *BS2782 Part 10 Method 1005 EN61 Methods of Testing Plastics – Glass reinforced plastics – Determination of flexural properties. Three point method*. British Standards Institute, UK, 1977.
7. *BS EN ISO 527-5:1997 BS 2782-3: Method 326G:1997 Plastics – Determination of tensile properties – Part 5: Test conditions for unidirectional fibre-reinforced plastic composites*. British Standards Institute, UK, 1997.
8. ASTM D5379/D5379M, Test method for shear properties of composite materials by the V-notched beam method, *Annual Book of ASTM Standards*, ASTM, Philadelphia, USA, 2000, Vol 15.03.
9. Halpin J.C. and Kardos J.L., The Halpin–Tsai equations: a review, *Polymer Engineering and Science*, 1976 **16**(5) 344–352.
10. Halpin J.C., *Primer on Composite Materials Analysis*, 2nd edn., Technomic, Lancaster, PA, 1992.
11. Hashin Z., *Theory of Fibre Reinforced Materials*, CR-1974, NASA, 1972.
12. Hashin Z., Analysis of composite materials – a survey, *J. Appl. Mech.*, 1983 **50** 481–505.
13. Naik N.K. and Shembekar P.S., Elastic behavior of woven fabric composites: I – Lamina analysis, *J. Composite Materials*, 1992 **26**(15) 2196–2225.
14. Reddy J.N., *Mechanics of Laminated Composite Plates: Theory and Analysis*, CRC Press. Boca Raton, FL, 1997.
15. Soldatos K.P., A comparison of some shell theories used for the dynamic analysis of cross-ply laminated circular cylindrical shells, *J. Sound Vib.*, 1984 **97** 305–319.
16. Soldatos K.P. and Timarci T., A unified formulation of laminated composite, shear-deformable, five-degrees-of-freedom cylindrical shell theories, *Composite Structures*, 1993 **25** 165–171.
17. Hofstee J. and van Keulen V., Elastic stiffness analysis of a thermo-formed plain-weave fabric composite. Part II: analytical models, *Composites Sci. Technol.*, 2000 **60** 1249–1261.
18. Tan P., Tong L. and Steven G.P., Predicting the mechanical properties of textile composites – a review, *Composites Part A* 1997 **28A** 903–922.
19. Crookston J.J., Long A.C. and Jones I.A., Modelling effects of reinforcement deformation during manufacturing on elastic properties of textile composites, *Plastics Rubber and Composites* 2002 **32**(2) 58–65.

20 Long A.C., Robitaille F., Rudd C.D. and Jones I.A., 'Modelling strategies for textile composites', *Proc 14th International Conference on Composite Materials (ICCM-14)*, San Diego, CA, 14–18, July 2003.
21. Crookston J.J., Prediction of elastic behaviour and initial failure of textile composites, PhD Thesis, University of Nottingham, 2004.
22. Bigaud D. and Hamelin P., From geometrical description to mechanical prediction – Application to woven fabric composites. *Sci. Eng. Composite Materials*, 1998 **7**(4) 291–298.
23. Chapman C. and Whitcomb J., Effect of assumed tow architecture on predicted moduli and stresses in plain weave composites, *J. Composite Materials*, 1995 **29**(16) 2134–2159.
24. Hofstee J., do Boer H. and van Keulen V., Elastic stiffness analysis of a thermo-formed plain-weave fabric composite. Part I: geometry, *Composites Sci. Technol*., 2000 **60** 1041–1053.
25. Hofstee J., do Boer H. and van Keulen V., Elastic stiffness analysis of a thermo-formed plain-weave fabric composite – part III: experimental verification, *Composites Sci. Technol*., 2000 **62** 401–418.
26. Whitcomb J.D., Three-dimensional stress analysis of plain weave composites. *Composite Materials: Fatigue and Stresses* (3rd volume), ASTM STP 1100, ed. T.K., O'Brien. ASTM, Philadelphia, 417–438.
27. Guedes J.M. and Kikuchi N., Preprocessing and postprocessing for materials based on the homogenization method with adaptive finite element methods, *Comp. Meth. App. Mech. Eng*., 1990 **83**, 143–198.
28. Ng S.-P., Tse P.-C. and Lau K.-J., Numerical and experimental determination of in-plane elastic properties of 2/2 twill weave fabric composites, *Composites Part B*, 1998 **29B** 735–744.
29. Dasgupta A., Agarwal R.K. and Bhandarkar S.M., Three-dimensional modeling of woven-fabric composites for effective thermo-mechanical and thermal properties, *Composites Sci. and Technol.,* 1996 **56** 209–223.
30. Zako M., Uetsuji Y. and Kurashiki T., Finite element analysis of damaged woven composite materials, *Composites Sci. Technol*., 2003 **63**(3–4) 507–516.
31. Aitharaju V.R. and Averill R.C., Three-dimensional properties of woven-fabric composites, *Composites Sci. Technol.*, 1999 **59** 1901–1911.
32. Brown D., Morgan M. and McIlhagger R., A system for the automatic generation of solid models of woven structures. *Composites Part A,* 2003 **34** 511–515.
33. Sun W., Lin F. and Hu X., Computer-aided design and modeling of composite unit cells. *Composites Sci. Technol.*, 2001 **61** 289–299.
34. Robitaille F., Long A.C., Jones, I.A. and Rudd C.D., Automatically generated geometric descriptions of textile and composite unit cells. *Composites Part A*, 2003 **34** 303–312.
35. Zienkiewicz O.C. and Taylor R.L., *The Finite Element Method* 5th edn, Butterworth-Heinemann, Oxford, 2000.
36. Hinton M.J., Soden P.D. and Kaddour A.S., *Failure Criteria in Fibre-Reinforced-Polymer Composites*, Elsevier, Amsterdam, 2004.
37. Cox B.N. and Flanagan G., *Handbook of Analytical Methods for Textile Composites*, NASA Contract Report 4750, March 1997.
38. Cook R.D., Malkus D.S. and Plesha M.E., *Concepts and Applications of Finite Element Analysis*, 3rd edn, Wiley, New York, 1989.
39. The LUSAS FE software code, www.lusas.co.uk.

40. PAM-CRASH™ FE code, www.esi-group.com.
41. Hart-Smith L.J., The role of biaxial stresses in discriminating between meaningful and illusory composite failure theories, *Composite Structures*, 1993 **25**(1–4) 3–20.
42. Johnson A.F., Pickett A.K. and Rozycki P., 'Computational methods for predicting impact damage in composite structures', *Workshop: Recent Advances in Continuum Damage Mechanics for Composites,* LMT-Cachan, 20–22 Sept. 2000.
43. Ladevèze P. and Le Dantec E., Damage modelling of the elementary ply for laminated composites, *Composites Sci. Technol.*, 1992 **43** 257–267.
44. ISO DIS15024 *Fibre-reinforced plastic composites – Determination of Mode I interlaminar fracture toughness, GIC, for unidirectionally reinforced materials*, International Organization for Standardization, Geneva.
45. ASTM draft standard D30.06: Protocol for Interlaminar Fracture Testing, End-Notched Flexure (ENF), revised April 24, ASTM, Philadelphia, USA.
46. Reeder J.R. and Crews J.H., Mixed-mode bending method for delamination testing, *AIAA J.*, 1989 **28**(7) 1270–1276.
47. Lourenco N.S.F., Predictive finite element method for axial crush of composite tubes, PhD Thesis, University of Nottingham, 2002.
48. Warrior N.A., Pickett A.K. and Lourenco N.S.F., Mixed mode delamination – experimental and numerical studies, *Strain*, 2003 **39** 153–159.
49. BMBF project, 'Textile Integrationstechniken zur herstellung vorkonfektionierter verstärkungsstrukturen für FVK', 1999–2002.
50. Gries T., Laourine E. and Pickett A.K., Potentiale nähtechnischer Fügeverfahren für Faserverbundwerkstoffe (Potential application of sewing technologies as a joining process for FRP materials), *Aachener Textil Tagung*, Nov 2001.